# Ground based interferometric synthetic aperture radar for monitoring slowly moving surfaces

Harald Iwe

March 2012

*Series of dissertations submitted to the*
*Faculty of Mathematics and Natural Sciences, University of Oslo*
*No. 1209*

ISSN 1501-7710



Cover: Inger Sandved Anfinsen.
Printed in Norway: AIT Oslo AS.

Produced in co-operation with Unipub.
The thesis is produced by Unipub merely in connection with the
thesis defence. Kindly direct all inquiries regarding the thesis to the copyright
holder or the unit which grants the doctorate.

# Contents

# Abstract

This thesis focuses on the construction and application of a ground based radar for monitoring slowly moving target surfaces such as unstable rock slopes. The radar is given the name GinSAR (Ground INterferometric Synthetic Aperture Radar). We first describe situations where usage of this kind of radar technology is appropriate. Given this situation description, a review of other possible sensors are given. All sensors are compared with respect to what kind of information they provide, update frequency, accuracy and limitations. The main identified disadvantage with the ground radar is found to be rather poor horizontal cross-range resolution.

The design objectives for GinSAR were therefore specified to include usage of much longer synthetic aperture than used by existing ground radars. Since it is difficult to realise a rigid and linear long synthetic aperture where the position of the radar antennas are known at any time, we instead decided to mount the radar on a wagon and let it roll on rails. The uncertainties in the radar position when the wagon is rolling on rails, requires usage of autofocus algorithms. Hence, the investigation and development of a suitable autofocus algorithm was also specified as an important target. We also wanted to investigate the possibility of generating digital elevation models using two receiver antennas vertically aligned.

We describe the working principle of the radar and schematic design of the electronics. The electronics can be divided into a frequency synthesis and up-conversion part, a receiver and demodulation part and a digital processor part. It is shown that repeat-pass interferometric processing requires a very accurate reference oscillator. High gain parabolic reflector antennas are used for making it possible to operate the radar on more than 3 kilo-meters range. To suppress the direct wave from the transmitter- to the receiver-antenna and avoid saturation of the receiver amplifiers, cylinders of radar absorbing material are mounted on the antenna rims. Calculations of the signal to noise ratio shows that the chosen radar design parameters meets the requirement for interferometric processing. The radar transmits a linear frequency modulated signal which is demodulated in the receiver, digitised and stored for later post-processing. The bandwidth of the radar is almost 140 MHz.

The SAR processing is done using an optimal matched filter implemented as a time-domain correlation operation for each point in the SAR image. By forming an interferogram between the complex SAR images from the two vertically aligned

receiver antennas, the vertical position of the image point can be calculated from the interferogram phase. In this way a digital elevation model is constructed. By forming an interferogram between two SAR images measured at different times, the temporal range displacement can be calculated. Both these calculations are deduced.

To test the radar electronics in isolation we have conducted measurements where the antennas were disconnected. Instead the transmitter was connected to the receiver using a 280 meter long coax-cable. Into this cable we added attenuators of varying value. The measured relationship between the signal to noise ratio and the phase noise variance, is shown to be in agreement with theory. The system noise temperature is measured to be 1598 Kelvin, corresponding to a noise factor of 5.5.

At the start of the construction phase the design with the radar moving on rails was considered to be too ambitious. The main concern was the the need for autofocus. As a first configuration we therefore decided to put GinSAR on a rigid linear guide of less than 3 meters length, and accept a large reduction in cross-range resolution. With GinSAR in this first configuration, we conducted measurements on a target area located at 2 kilo-meters range. In the target area 3 reflectors were placed out. One of the reflectors were attached to a solid mast using a threaded iron. By screwing the reflector complete turns on the threaded iron the reflector range could be adjusted with sub milli-meter accuracy.

The measured SAR images shows as expected poor cross-range resolution due to the short synthetic aperture length, but the reflectors can easily be identified. By conducting repeated SAR images the temporal range displacement of the reflectors were calculated. The measured displacements, ideally zero, are small and can be explained with changes in the state of the atmosphere during the measurement period. The enforced displacement of the adjustable reflector were measured with approximately 10 % error which can be explained by the measurement setup. We also calculated a digital elevation model using the interferogram formed between the SAR images from the two vertically aligned receivers. The calculated relative altitude between the reflectors are fairly correct compared to accurate reference data, but other parts of the model has significant errors compared to a reference map.

Based on the results from these measurements using the short linear guide, we concluded that the ground radar would benefit significantly if the cross-range resolution is improved. We also experienced that the radar was difficult to handle and vulnerable to wind induced vibrations beacuse of it's size. We therefore decided to mount the radar on a wagon and let it roll on rails as in the original design, but also to use only one receiver antenna and omitting the possibility to generate digital elevation modells.

In this configuration an autofocus algorithm was required. The development of a suitable algorithm for a ground radar has been an important part of this thesis. Initially, the causes of defocus and their effects are discussed and examples are given. We also discuss necessary assumptions taken by most existing autofocus algorithms. In most SAR applications the processing is done in the frequency do-

main taking advantage of the fast Fourier transform algorithm. A majority of the existing autofocus algorithms assumes SAR processing in the frequency domain. The review of existing algorithms therefore starts with an short introduction to frequency domain SAR processing and the connection with autofocus. The main principle of the phase gradient, weighted least squares and the image contrast algorithms are given. Their applicability to GinSAR is discussed.

The ideas behind the scatter modelling autofocus algorithm is identified as being best suited for GinSAR, it can estimate a phase error function of any order, and it is not inherently connected to frequency domain SAR processing. In its original form the algorithm is formulated by assuming frequency domain SAR processing using a relaxation optimising procedure for estimating scatter magnitude, position and phase. It is shown how the different algorithm steps can be formulated if the SAR processing is conducted in the time-domain. In this formulation it is computationally much more efficient to calculate the SAR image points on a polar grid instead of the more normal rectangular grid. The accuracy of the algorithm is depending on the ability to identify all significant scatterers. This is a difficult task if the image is strongly defocused. We therefore introduce the concept of a threshold-function to improve the robustness of the algorithm. We also extend the identification and impulse response subtraction to two dimensions to reduce the number of false scatter identifications. The final estimation of one common phase error function combines the estimates from the independent range-arcs using concepts from robust statistics. The estimates from the independent range-arcs that are very different from the others are rejected.

The algorithm has been evaluated by many simulated examples. It is capable of etimating the true phase error function with small errors even in difficult cases. We have also analysed the impact of errors in the estimation of the scatterers (position and magnitude).

The configuration of the radar that rolls on rails and the measurement site is described in detail. The position along the rails was measured using a distance wheel connected to an optical encoder. Since the radar was placed on the roof of a building, the length of the synthetic aperture was limited to 12 meters. The target area “Vettakollen” consists of a rather densly vegitated hill where we were able to find only two openings suitable for mounting reflectors. This hill is geological stable. Ideally our measurements should therefore indicate zero movement. In total 175 measurements were conducted during approximately 24 hours.

The SAR magnitude images processed without any autofocus estimation shows that the reflectivity of the natural terrain is rather low, and that the response of the reflectors appears blurred indicating significant phase errors. When using our autofocus algorithm to estimate the phase error functions from all SAR images, the functions resembles each other. This is as expected since we observe that the radar wagon sidewise movement on the rails are mostly repeated between the measurements. When using the estimated phase error functions in a second SAR processing, the response of the reflectors resembles the theoretical point scatter impluse response very well.

Interferometric range processing of the reflectors show that changes in the

propagation speed due to changes in the atmosphere is the main error source for the interferometric ground SAR. It is shown how the propagation speed is a function of temperature, pressure and partial water vapour pressure. The sensitivity of the measured interferometric range as a function of these state variables is calculated. By modelling these state variables the changes in propagation speed can be compensated. Our efforts to make a model by using available meterological data were only partly sucessful. Still, we believe this procedure can be successful if the measurements are taken closer to the radar propagation path and at the same time as when the radar measurements are conducted.

Using a reflector in the target area that is in a static or known posistion is an alternative to modelling the atmosphere. The variations in the measured interferometric range of the reference reflector can be used to calculate the variations in the propagation speed. In this way very accurate measurements can be achieved. All error sources that are common between the reference reflector and other scatterers are canceled. The only remaining are propagation speed differences because of slightly different propagation paths and electronic measurement noise. When using one of our reflectors as a reference, the standard deviation of the measured interferometric range to the other is less than 1 milli-meter. The main draw-back using a reference reflector is the practical problem of finding or establishing a reference reflector in a static or known position. In most situations the whole area illuminated by the radar is subject to movement. Hence, the most practical solution is to measure the movement of the reference by other means, optical surveying or by usage of a geodetic GPS receiver. Of course, such instrumentation adds to the complexity and cost of the measurement setup.

Our main conclusion is that we have build a functional ground SAR with improved horizontal cross-range resolution suitable for monitoring slowly moving surfaces. Since the required long synthetic aperture makes it impractical with a rigid linear guide, we have instead relied on accurate autofocus as a part of the SAR processing. We have therefore developed an accurate autofocus algorithm suitable for a ground SAR with time domain SAR processing. Measurements prove that the radar can measure surface movements with milli-meter accuracy.

# Acknowledgements

During this work I have received valuable help and support from many individuals and institutions who I would like to thank. In particular:

- My supervisors Svein-Erik Hamran and Trygve Sparr at Norwegian Defence Research Establishment (FFI)
- Jan Gundersen and Gudmund Havstad at Norwegian Geotechnical Institute (NGI) for helping me with all mechanical constructions
- Leiv Gelius at NGI for valuable discussions on SAR processing
- Colleges and friends at NGI for proof reading
- NGI which has supported my work financially

Oslo, March 2012
Harald Iwe

# Chapter 1

# Introduction

This thesis deals with ground based radar technology for monitoring slowly moving targets such as unstable rock slopes, mountain blocks and dams. As a part of the work a complete functional radar has been built, it has been given the name "ground interferometric synthetic aperture radar" (GinSAR). The main focus is on this radar itself, principle of operation, radar design, special properties, propagation and scattering, signal processing and achievable performance. But to prepare the reader for the radar technical part, this introduction will start by describing situations where usage of this kind of radar technology is appropriate. Given this situation description, a review of other possible kinds of sensors are given including principle of operation and an evaluation. Also in this context, we will in more detail evaluate the ground radar, ie. specify what kind of information the radar can contribute with, what are the limitations and which properties of the radar one should try to optimize.

Finally an outline of the rest of the thesis is given in section 1.2.

## 1.1 Monitoring slowly moving target areas

In many parts of the world there have been land slides that have caused loss of lives and large damage to human property and infrastructure [2]. There are also a number of ageing dams which stability has been questioned by construction engineers [1]. The task to reduce the impact of land slides and avoid dam failures typically starts with a geotechnical investigation to assess the risk. These investigations normally include drilling and other subsurface remote sensing investigations such as refraction seismic, ground penetrating radar (GPR) and resistivity profiling. Measurements of any surface movements using optical instruments, Global Navigation Satellite Systems (GNSS) receivers and radar (both satellite and ground based), can help in understanding the problem.

After the initial investigation and risk assessment and after any possible mitigating actions, it is often necessary to monitor the unstable area or construction as a part of an early warning strategy. Typically there will be some small accelerating

movement preceding a slide or failure a few days or hours in advance. Accurate and reliable detection and measurement of such small accelerating movements are therefore of high importance in deciding when to start emergency procedures.

As an example we will describe the situation at Åknes, located in Synnylvsfjorden, Norway. Figure 1.1.1 shows a photo of the unstable slope and a map of the area. The unstable part of the slope is marked in red on the photo and in grey on the map. It covers approximately $1\,\mathrm{km}^2$, and the amount of unstable mass is estimated to be more than $40 \times 10^6\,\mathrm{m}^3$. There is no infrastructure in the close vicinity of the unstable area, the danger lays in the tsunami that will be generated when such huge amount of mass falls into the fjord. In the top of the unstable area there is a more than 10 meters deep crack. Extensiometer measurements show a steady increasing opening of this crack of approximately 20 - 50 millimeters annually. The measured movement in the lower area is approximately 5 - 30 milli-meters annually.

Many different approaches have been used in order to understand the geotechnical processes such as core drilling including core sample analysis, refraction seismic, georadar and resistivity profiling. The boreholes have been instrumented with inclinometers and pressure sensors measuring the ground water level. The surface movement has also been measured by satellite navigation receivers, optical instruments and ground based radars as described in sections 1.1.1, 1.1.2 and 1.1.3. For more information on the situation at Åknes including the instrumentation, see [15].

The main conclusion can be summarised in the following points:

- Some time in the future a part of the unstable area will release and initiate a land slides, mainly consisting of rocks.
- The movement velocity is a function of position in the slope and season. The velocity is largest at times with heavy rain and snow melting.
- In the months and weeks before a release it is likely that the slope movement speed will increase.
- In the hours before a release there will almost certainly be micro seismic activity (very small earth quakes).

A reliable early warning system requires constant monitoring of the slope speed. The following sections gives a general introduction to different sensors that can be used for that task.

### 1.1.1 Satellite navigation receivers

In a network of geodetic satellite navigation receivers each receiver that is placed out in the unstable slope will measure the 3 dimensional displacement vector from one measurement to the next. The achievable accuracy is normally 5 milli-meters or better relative to one or more reference receivers. For a general introduction to geodetic measurements using satellite navigation systems, see [89]. Since one

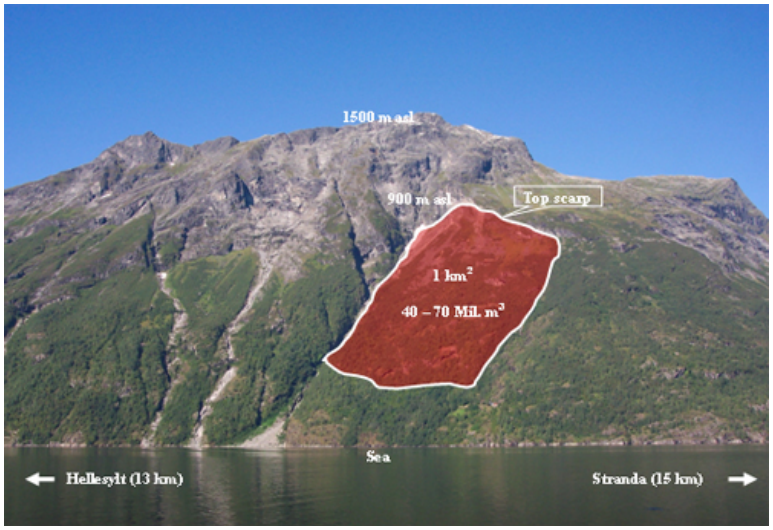


(a)


(b)

Figure 1.1.1: Photo and map of Åknes.

receiver will measure the movement of only one point, many receivers will be needed to monitor all parts of an unstable slope. The measured data from each receiver must somehow be collected before calculation of the displacement vectors are possible, adding to the complexity of the installation. In north-facing slopes at high latitudes, satellite visibility may also be a problem. Snow and ice accumulated on the antennas may disturb the measurements.

In summary, a network of satellite navigation receivers can give accurate measurements of the displacement vector in 3 dimensions but the number of points will be limited by the number of receivers.

### 1.1.2 Optical instruments

A laser distance measurement instrument and a theodolite (in combination normally called a total-station) are able to measure the 3 dimensional position of reflecting prisms. The range and angular accuracy is claimed to be approximately 3 milli-meters and 2 arc-seconds respectively in benign conditions by several producers[1]. One total-station can measure the position of many prisms within sight. The need for prisms comes mainly from the theodolite. On ranges up to some hundred meters laser distance scanners can measure the distance to thousands of points on a bare rock wall due to its very high cross-range resolution [111].

The accuracy of the distance measurements are limited by uncertainties in the propagation speed due to changes in the state of the atmosphere. The usable range will be limited in conditions with reduced optical sight. Since the theodolite has a given angular accuracy the associated (cross-range) position error will increase with range. As most optical equipment these instruments including the reflecting prisms are very sensitive to fog, rain, snow and pollen.

### 1.1.3 Radars

#### 1.1.3.1 Satellite radars

SEASAT was the first civilian SAR satellite to be launched in 1978 [3]. But the launch of European ERS-1 satellite in 1991 marks the beginning of continuous SAR monitoring. At that time sufficient digital processing power had become available for pure digital SAR processing. Since then satellite based radars using interferometric processing have demonstrated a capability to measure displacements in the milli-meter region [36]. After the launch of ERS-1 [8] followed the Japanese JERS-1 [73] in 1992, ERS-2 in 1995, the Canadian RADARSAT-1 [85] in 1995, the European ENVISAT [24] in 2002, RADARSAT-2 in 2007, Italian COSMO-SkyMed [56] in 2007 and the German TerraSAR-X [104] in 2007, just to mention the most important. There has been a remarkable development in data quality provided by these satellite SARs during the last two decades.

Since the launch of the ERS-1 in 1991 the recorded data from most of these satellites are available, and can be processed to find the movement speed during

[1] Topcon Europe B. V. (http://www.topconeurope.com), Leica Geosystems AG. (http://www.leica-geosystems.com/en/index.htm)

this period. This possibility of processing historic data from the last two decades is unique for this sensor.

The main disadvantage is a relative low update frequency. The update period for one satellite is typically one month. Even if data from many satellites are available, the period will be some days. The only displacement component that is measured is the line of sight to the satellite. Typically this is 20 degrees off the vertical but there are variations. The cross-range resolution for the early satellites were approximately 20 meters, in spotlight mode TerraSAR-X shall approach 1.5 square-meters [105]. The correlation between measurements (made at different times) are difficult in vegetated and snow covered areas. Finally, changes in the state of the atmosphere changes the propagation speed and represents a significant error source.

#### 1.1.3.2 Ground radars

Since ground based radars using interferometric processing and a synthetic aperture is the subject for this thesis, an extensive description will follow later. In this summary we will limit to state the main properties.

The sensor has demonstrated a capability to measure displacements as small as 1 milli-meter [6, 78, 4]. The time for one measurement including data processing is typically 5 - 20 minutes. The horizontal cross-range resolution are given by the length of the synthetic aperture, the wavelength and the range to the target area. Longer aperture gives better horizontal cross-range resolution.

The actual true vertical cross-range resolution is given by the vertical size of the antenna and the wavelength which, when calculated, gives essentially no practicable vertical cross-range resolution at all. However, the target area and the radar location is normally such that the radar "looks up into a slope". Seen from the radar, as the range to the scatterers increases, the vertical cross-range position of the scatterers increases, too. In this way the vertical cross-range resolution is given by the range resolution and the slope angle relative to the radar's line of sight line. The range resolution is given by the bandwidth of the radar. For GinSAR the bandwidth is 140 MHz giving a range resolution of approximately 1 meter.

The only velocity movement component that is measured is the line of sight to the radar. In contrast to the satellite radar, this is normally close to the full velocity vector. If a resolution cell is vegetated or covered with snow, the measurements will include changes in the soil water content and snow thickness. Only resolution cells mainly consisting of rocks and bare mountain will give accurate measurements of the movement. In steep slopes and high mountain areas there will usually be a large number of such cells making it possible to produce deformation maps and not only point-wise measurements.

Changes in the state of the atmosphere will change the propagation speed, and is a significant error-source in the measurements. The impact increases with the range to the target area.

As previously said, a long synthetic aperture will give high horizontally cross-range resolution. But finding a suitable place for a long synthetic aperture might

be difficult at some sites.

### 1.1.4 Evaluating ground radars

There are advantages and disadvantages with all sensors described in sections 1.1.1 to 1.1.3. If possible the most reliable and accurate instrumentation would be to use several of the systems as they are to some extent complementary. As a part of an early warning system satellite radars are not suited, the update period is too long. On short ranges laser distance scanners work very well. Both ground radars and optical instruments measure the position of some target point relative to the position of the sensor. This can be a problem if it is difficult to find a sensor placement position which with certainty is know not to be moving, and has a clear view to the unstable area. GPS receivers do not have this problem. However, it is required that they are placed out into the unstable area which, in some cases, can be difficult or dangerous to access. To summarise, the choice of a sensor configuration must be made by a careful consideration of the local conditions. We do not make the claim that the ground radar in general is superior.

A major part of this thesis deals with improving properties of the ground radar. More specifically, decreasing the size of the resolution cells will be an advantage. By itself higher spatial resolution is an advantage, but it will also increase the area containing resolution cells that give accurate information on the movement of the mountain surface. With a given poor resolution, one resolution cell may contain some part of bare mountain and some part of vegetated soil. The measurements for this cell can be completely deteriorated by the vegetated part. With higher resolution, however, one resolution cell may contain only the bare mountain part, and provide accurate measurements of the movement.

Decreasing the size of the resolution cell can be divided into the different dimensions. As stated in section 1.1.3.2 the ground radar has virtually none practical vertical cross-range resolution. In most situations a high range resolution is sufficient. But vertically cross-range resolution can sometimes resolve ambiguities, and provides the possibility to construct digital elevation maps (DEM). In an effort to achieve practical true vertical cross-range resolution we have as a part of this work, tried to use two receiver antennas mounted on each side of the transmitter antenna vertically aligned.

The horizontal cross-range resolution is given by the length of the synthetic aperture and the wavelength. As an example let us assume an aperture length of $L = 2.63$ meters and a centre frequency $f_c = 5790$ MHz. At a range $R = 2000$ meters the horizontal cross-range resolution (half power) becomes $r_{cr} = 35$ meters. Such large resolution cells has clear disadvantages. These numbers are taken from GinSAR in the first configuration. The cross-range resolution for the radar parameters used in [78] ($f_c = 5850$ MHz, $L = 1.80$ meters) becomes $r_{cr} = 51$ meters. For the radar parameters in [81] ($f_c = 9650$ MHz, $L = 2.00$ meters) $r_{cr} = 28$ meters. To decrease the size of the horizontal cross-range resolution, we have (in the second GinSAR configuration) made a railway where the radar is mounted on a wagon. The length of the synthetic aperture can in this case be

almost as long as the rails. Using rails of length $L = 30$ meters, the cross-range resolution will in GinSAR's case be reduce to $r_{cr} = 3$ meters.

Most existing ground radars move on a rigid linear guide where the position of the radar unit is measured accurately along the guide and can be assumed to be known. Mechanically these designs are rigid, preventing any sidewise motion which ensures a straight line movement. But constructing and setting up a rigid linear guide longer than a few meters is impractical. It becomes difficult to maintain the rigidness.

Since we strongly want a long synthetic aperture we investigate using arrangements such as putting GinSAR on a wagon rolling on rails. In this case the position of the radar cannot assumed to be exactly known. The rails can very well have small curves and heaves because of uneven ground support. In addition, wind gusts may move the antennas, both because of mechanical flexibility in the wagon, and because the wheels have some freedom to move sideways on the rails. As a result, the position of the radar antennas is not known with sufficient accuracy. Our approach has been to develop an autofocus algorithm to estimate the position of the antennas. To our knowledge using autofocus in a ground radar such as described is a step in a new direction. Autofocus has successfully been applied in aircraft and satellite SARs. But these algorithms are not optimal for the ground SAR. The development and testing of an algorithm optimised for this application is a major part of this thesis.

## 1.2 Thesis outline

**GinSAR design (chapter 2)** A significant part of this work has been to design and build a radar optimised for monitoring slowly moving targets. In this section the block schematic design is described, the design choices are given and the principle of operation is explained.

**Signal processing (chapter 3)** First the fundamental SAR processing is outlined. It is followed by calculation of digital elevation models (DEM) and interferometric maps.

**Cable measurement tests (chapter 4)** We have conducted tests where the antennas are disconnected and instead the transmitter is connected to the receiver by a long cable. The purpose is not only to check if the radar functions as intended, but also to determine the radar performance.

**Linear guide measurements (chapter 5)** In the first configuration GinSAR consisted of three antennas vertically aligned, where the transmitter was mounted in the middle and the two receiver antennas was mounted above and below. The antenna unit moved on a rather short linear guide. This section describes the measurement tests conducted in this configuration.

**Introduction to Autofocus (chapter 6)** In the second GinSAR configuration one of the receiver antennas was removed, and the radar unit including the two remaining antennas was put on a wagon rolling on rails. Because of mechanical flexibility the sidewise position of the antennas were uncertain and autofocus were needed as a part of the SAR processing. This section gives a general introduction to SAR autofocus and evaluates existing autofocus algorithms applicability to GinSAR.

**SMAA with frequency domain SAR processing (chapter 7)** The ideas behind the scatter modelling autofocus algorithm (SMAA) is considered to be best suited for GinSAR. It can estimate a phase error function of any order, and it is not inherently connected to frequency domain SAR processing. In this section the algorithm is described, and the essential steps of the algorithm is identified and analysed.

**SMAA with time domain SAR processing (chapter 8)** With the analysis from chapter 7 as background the SMAA is formulated to be used with time domain SAR processing. The algorithm is analysed and tested by many simulations, and the impact of scatter estimation errors are evaluated.

**Radar on rails measurements (chapter 10)** First we describe the measurement site and railway setup. Then we continue with autofocus and SAR processing. The last part is devoted interferometric range measurements.

**Conclusion (chapter 11)** This final chapter addresses the conclusions.

# Chapter 2

# GinSAR design

## 2.1 Review of similar radars

Several ground-based SAR (GB-SAR) have been described in the past. [81] There are many similarities between these but also some significant differences. In the following we have tried to summarise the main characteristics and include the reported applications.

The Linear SAR system (LiSA) [88, 6] is a GB-SAR developed at the Joint Research Centre of the European Commission. There are many versions of this system which essentially differs in the frequency band they operate and on the length of the synthetic aperture. The frequency-bands[1] are L, C and Ku, the aperture length is between 1 and 5 meters. It is a step frequency radar using a vector network analyser as a signal generator and detection circuit. The main applications are landslides and man-made structures monitoring [51, 7, 21].

The vector network analyser has been used in ground penetrating radars (GPS) for more than 20 years [49]. It is a very sensitive and accurate laboratory instrument, but it uses relative long time to step through all frequencies and complete one measurement. A GB-SAR that uses a network analyser must therefore move very slowly on the aperture, ideally the antenna unit should be in complete stop when a measurement is taken, and then move to a new position before the next measurement starts.

The Universitat Politècnica de Catalunya (UPC) in Spain has developed a GB-SAR using a frequency modulated continues wave (FMCW) signal [4]. By changing the microwave front-end and antennas the radar may operate in L, C, X and Ku-band. The whole radar is mounted on a linear guide of length 5.5 meters and includes an optional polar-metric capability. The radar has been used for monitoring mining induced subsidence [81, 57, 82]. It has also been used

[1]

| Letter band | Frequency (GHz) |
|---|---|
| L | 1 - 2 |
| S | 2 - 4 |
| C | 4 - 8 |
| X | 8 - 12 |
| Ku | 12 - 18 |

to analyse measurement artefacts introduced by changing atmospheric conditions [83].

The University of Sheffield, United Kingdom, has made an experimental GB-SAR using a network analyser [11]. The main application is to understand better the microwave backscatter characteristics of vegetation and soils. It is mainly operated in the X-band, it uses an aperture length of 4 meters and has polar-metric capabilities.

Zhou, Boerner and Sato has made a GB-SAR designed for ground-truth validation in environmental studies of terrestrial vegetation cover, and especially in biomass estimation [110]. It is based on a vector network analyser using a frequency band from 400 MHz to 6 GHz and includes polar-metric capabilities. The antenna unit can be moved up to 20 meters horizontally and 1.5 vertically. The radar has also been used to find detailed scattering mechanisms and detect deformations [35]. In both reported applications the target range was less than 15 meters.

Gamma Remote Sensing, Swiss, has made an interferometric ground-radar designed for monitoring landslides, glaciers and dams using a real aperture antenna[103]. There are 3 antennas, the transmitter antenna is placed above the 2 receiver antennas. They are all designed as slotted wave-guides approximately 3 meters wide. The azimuth beam-width (3 dB) is 0.43 degrees. The whole antenna unit is turned around the vertical to scan the target area. The centre frequency is 17.2 GHz and the bandwidth is 200 MHz. The usage of FMCW modulation should make it possible to scan the whole scene in less than a minute enabling the radar to monitor rapidly moving targets.

The Usikov Institute for Radio-physics and Electronics, Ukraine, has made a GB-SAR that operates at a centre frequency of 36.5 GHz and has a bandwidth of 450 MHz [59][60]. This radar uses noise modulation and has a synthetic aperture length of 0.7 meters. The antenna is made as a wave-guide where the position of a radiating slot is slide along the guide. The radar has been used for indoor monitoring of ceilings, roofs of big halls and hangars [58].

The FGAN Research Institute for High Frequency Physics and Radar Techniques and Fraunhofer Institute for Applied Solid State Physics have developed an experimental radar operating simultaneously at 10, 35, 94 and 220 GHz [28]. It is used in two measurement configurations. In the first configuration the target object is placed on a turn-table and rotated while the radar is in a fixed position (inverse SAR). In the second configuration the radar is put on a wagon rolling on rails. The radar uses FMCW modulation and has a bandwidth of 4 GHz at 94 GHz. It's main application is to determine the scattering centre distributions of targets.

The Korean Institute of Geoscience and Mineral Resources and Kangwon National University, Korea, have made a GB-SAR using a network analyser [50]. The radar uses a frequency band from 5.0 - 5.6 GHz and moves on a 5 meters long aperture (wagon on rails). A trihedral corner reflector was placed out at 160 meters range, and moved some milli-meters towards the radar for each acquisition. When studying the phase stability of the measurements, it is concluded that applying

atmospheric corrections to the SAR processing reduces the range error to less than 1 milli-meter.

A somewhat similar evaluation of the atmospheric disturbances on GB-SAR measurements has also been investigated in [76]. It is concluded that without any compensation for the changes in the state of the atmosphere, the induced phase errors can completely mask the actual point-scatter displacements.

There have been conducted a number of measurement campaigns demonstrating the capability of the GB-SAR to measure slow slopes movements during periods of months [61][78] and even years [94]. It has also been investigated if the GB-SAR can be used to monitor the snow depth in mountain areas [62].

Some GB-SARs have been designed to have sufficient vertical cross-range resolution for DEM calculation. One possible design where the vertical position of the aperture can be adjusted is proposed in [80]. A sensitivity analysis is carried out in [74]. Theoretical expressions for the calculation of elevation given a number of SAR images acquired from spatially separated apertures, and supporting measurement results, are given in [75, 77, 86].

The development of SAR started with using aircrafts as a carrier platform [32]. This development has continued, there are many aircraft SARs reported in the literature and new sensors keep being designed and constructed [96, 66, 25, 108, 102, 79, 17, 87]. Some of the radars described in these references are physically small and light sensors that may be carried by unmanned air vehicles (UAV). There are also a significant interest in using aircraft-SARs for military reconnaissance and surveillance applications. It is, however, beyond the scope of this text to give a fair review of all these sensors. Instead we have chosen to state some general properties as a comparison with the GB-SAR.

As with GB-SARs there are aircraft-SARs that operate in all parts of the microwave spectrum. They typically transmit short FMCW pulses. Step-frequency modulation as used by the network analyser, will not work because the radar moves with high speed. Compared to GB-SAR, aircraft-SARs typically achieve very high cross-range resolution because the length of the synthetic aperture is much longer. If the beam pointing direction can be steered, the cross-range resolution becomes even higher. Since the radar is carried by an aircraft, it is possible to illuminate large areas in short time. However, continuous monitoring many times each day for long periods is demanding.

Accurate focusing in the SAR processing is a significant challenge because of uncertainty in the position of the aircraft for each transmitted pulse. In contrast to satellite SARs which flies in almost predicable orbits, aircrafts are subject to wind gusts. One possible mitigating action is to use a navigation system. The most accurate aircraft navigation systems typically consists of a differential satellite-navigation receiver tightly integrated with an inertial navigation unit. Such integrated navigation systems are able to estimate the position of the aircraft with an uncertainty of some centimetres [37]. But accurate SAR focusing requires phase errors less than a fraction of a wave-length. For repeat pass interferometry the position-error tolerance is even smaller, [23] specifies 0.25 rad. Hence, usage of autofocus algorithms are often paramount. For GB-SARs moving on a rigid linear

guide autofocus is normally not needed. GinSAR in the second configuration will, however, benefit from autofocus processing.

## 2.2 Design objectives

The overall design objective has been to develop a radar including post-processing software capable of measuring sub milli-meter movement of surfaces such as rock slopes. The radar should be able to operate on relative long ranges such as across fjords, and it should have high cross range resolution, both vertically and horizontally, even if only poor quality digital elevation maps of the target area are available.

The requirement for high horizontal cross-range resolution makes a synthetic aperture in excess of 10 meters necessary. This is practically difficult to achieve using a rigid linear guide where the radar position is always known. Instead we decided that the radar should be mounted on a wagon which were rolling on a pair of rails. Since this construction introduces flexibility in the position of the antennas, we planned to use autofocus algorithms. As an aid to the autofocus procedure and to compensate for errors induced by changing atmospheric conditions, some reflectors could be placed out in the illuminated area at positions known to be fixed. To achieve vertical cross-range resolution making it possible to construct DEMs, we decided to make two complete receiver channels, each with its own receiver antenna. The transmitter and the two receiver antennas should be aligned vertically with the transmitter antenna in centre.

At the start of the construction phase we felt this design was too ambitious, the need for autofocus was the main concern. We felt it would be better to start with a configuration closer to what others had done, and what we evaluated to have higher chances of being successful. Hence, as a first configuration we decided to put GinSAR on a rigid linear guide and accept a reduction in cross-range resolution because of practical limitations in the length of the linear guide. The concept of using the 3 vertically aligned antennas were kept.

## 2.3 Schematic design and working principle

Figure 2.3.1 shows a block schematic diagram of the most important parts of the radar. Note that for simplicity only one receiver channel is shown, both channels are identical. The basic principle of operation is to transmit a linear frequency sweep pulse where the received reflected and delayed signal is mixed with the transmitted signal before analogue-to-digital conversion. Since the frequency sweep pulse duration $t_c$ is much longer than the propagation delay $t_d$, transmission and reception occur simultaneously. Hence, separate transmitter and receiver antennas are required. In all following expressions the amplitude factor has been suppressed for clarity since the vital information is contained in the phase.

The direct-digital-synthesis (DDS) chip generates a $t_c = 15.358$ milli-seconds linear frequency sweep "chirp" signal from 20 MHz to 160 MHz:

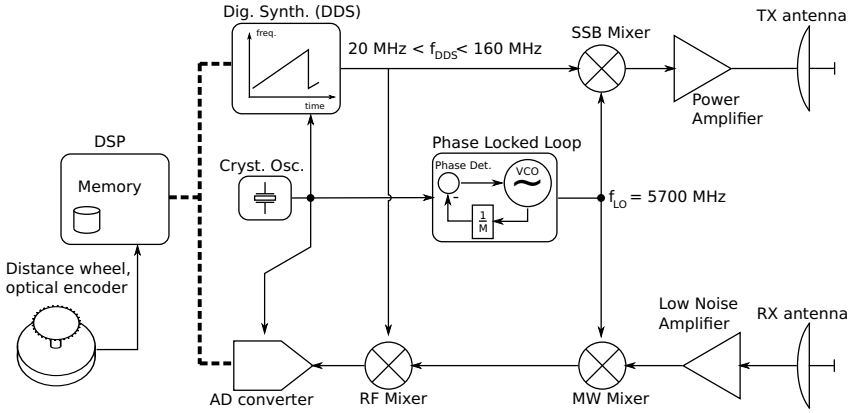


Figure 2.3.1: Block schematic diagram.

$$s_{DDS}(t) = \cos\left(\beta t + \frac{1}{2}\alpha t^2\right) \tag{2.3.1}$$

Here $\beta = 2\pi \times 20 \times 10^6$ rad/s is the DDS chip starting angular frequency, $\alpha = 2\pi \times 9.11 \times 10^9$ rad/s$^2$ is the angular frequency acceleration and $t$ is running time in seconds limited to the interval $0 < t < t_c$. This signal is mixed with the stable local oscillator signal given by $s_{LO}(t) = \cos(\omega t)$, where $\omega = 2\pi \times 5700$ rad/s. The mixing is done in a single-side-band (SSB) mixer where the lower side-band is suppressed. The resulting signal which is amplified and transmitted becomes

$$s_{TX}(t) = \cos\left((\omega + \beta)t + \frac{1}{2}\alpha t^2\right) \tag{2.3.2}$$

For a single point scatter the received signal is a time delayed version of the transmitted signal where the time delay $t_d$ is equal to the two-way propagation time

$$s_{RX}(t) = \cos\left((\omega + \beta)(t - t_d) + \frac{1}{2}\alpha(t - t_d)^2\right) \tag{2.3.3}$$

This received signal is mixed with the the local oscillator signal in the microwave (MW) mixer. The low frequency component output becomes

$$s_{RF}(t) = \cos\left(\beta t - (\omega + \beta)t_d + \frac{1}{2}\alpha(t - t_d)^2\right) \tag{2.3.4}$$

This signal is again mixed with the signal from the DDS chip in the radio-frequency (RF) mixer. The low frequency component output is

$$s_{ADC}(t) = \cos\left(\alpha t_d t - \frac{1}{2}\alpha t_d^2 + (\omega + \beta)t_d\right) \tag{2.3.5}$$

where $t_d < t < t_c$. The final step is to convert $s_{ADC}(t)$ into digital form using an analogue-to-digital converter (ADC). The converted signal is given by

$$s[n] = \cos\left(\alpha t_d\, n\Delta t - \frac{1}{2}\alpha t_d^2 + (\omega + \beta)t_d\right) = \cos\left(\omega_d\, n\Delta t + \phi_d\right) \tag{2.3.6}$$

The sample period is $\Delta t = 2$ micro-seconds and the sample number $n$ is defined in the range $n \in [0,\, N-1]$ where $N = 7679$. After conversion $s[n]$ is stored for post-processing.

The design parameters $t_c$, $\beta$, $\alpha$, $\omega$, $\Delta t$ and $N$ are all software programmable within limits. The choice of pulse length $t_c = 15.358$ milli-seconds makes it possible for the radar to move continuously along the aperture while measuring. If the speed on the aperture is 0.1 m/s, the movement during one measurement will be 1.53 milli-meters. This is mostly a sidewise motion (depending on the squint angle) and generally acceptable. A high speed radar-carrier like an aircraft would require a much shorter pulse length. The advantage of using such relative long pulse length is lower frequency on the ADC input signal (equation 2.3.5), lessening the hardware requirements. In both GinSAR configurations the movement speed is actually much slower than 0.1 m/s.

The start of a new linear frequency sweep, and a new sequence of $N$ ADC samples, is initiated by a pulse-edge from the optical encoder mounted on the same axis as the distance wheel, see figure 2.3.1. In this way measurements are taken at uniform separated positions along the linear guide.

Both the phase $\phi_d$ and the frequency $\omega_d$ of the cosine argument in equation 2.3.6 are functions of the propagation delay $t_d$. The suppressed amplitude factor will be proportional to the magnitude of the point scatter. The optimal way to estimate the amplitude factor is to use the matched filter [97]. It is optimal in the sense it maximises the signal to noise ratio. More on matched filtering as a part of the SAR processing follows in section 3.2.

## 2.4 Hardware design

### 2.4.1 Signal synthesis and the transmitter chain

Figure 2.4.1 shows the function blocks of the frequency synthesis circuits and the transmitter chain.

#### 2.4.1.1 Signal synthesis

There are two DDS chips which are designed to work in synchronization, one generating a cosine- (DDS1) and the other a sine-signal (DDS2). Both chips are clocked by a very stable oven controlled crystal oscillator (OCXO). The output digital-to-analogue converters (DAC) inside the DDS chips are clocked at 400 MHz. Due to the inherent $sin(x)/x$ roll-off in DACs and practical limitations in the design of sharp edge low-pass filters, the highest output frequency at the end

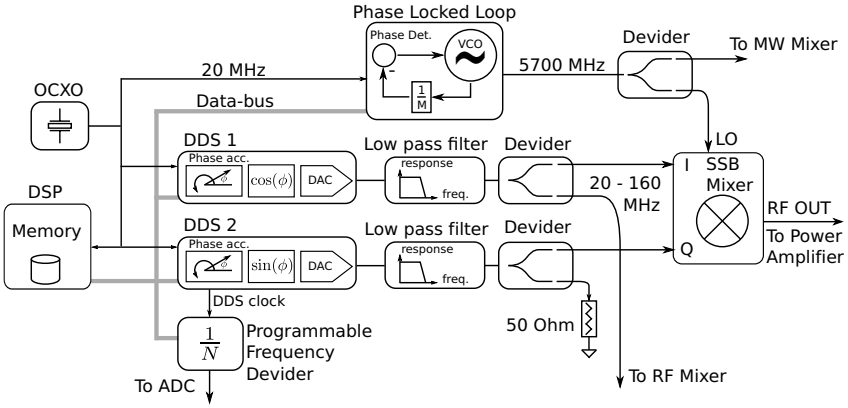


Figure 2.4.1: Frequency-synthesis.

of the frequency sweep has been programmed to 160 MHz. The lowest frequency at the beginning of the sweep has been programmed to 20 MHz. The low-pass filters have their 3 dB attenuation frequency at 195 MHz. The sine- and the cosine signal paths have been made exactly equal to preserve the magnitude- and phase balance.

#### 2.4.1.2 Reference oscillator

The oven controlled crystal oscillator (OCXO) is the origin clock source for all circuits that requires a clock for operation. The phased locked loop (PLL) uses the OCXO output signal directly to synthesise a stable local oscillator signal at 5700 MHz. The digital signal processor (DSP) and the DDS circuits also uses the OCXO clock signal directly. The DDS circuit has an integrated PLL that generate the 400 MHz DDS clock used by the internal DAC. This DDS clock, which is synchronous to the start of the frequency sweep, is divided down to 500 kHz and used to trigger the ADCs. In this way all digital signal sequencing, including ADC sampling, which takes place during one measurement-sweep is completely deterministic. This is a necessary property of an accurate coherent radar like GinSAR.

#### 2.4.1.3 Frequency up-conversion

The SSB mixer converts the I and Q (cosine and sinus) quadrant signals from the two DACs (20 - 160 MHz) into the output frequency band (5720 - 5860 MHz). The suppression of the local oscillator (LO) carrier (5700 MHz) and the first lower side-band (5540 - 5680 MHz) is more than 22 dB and 20 dB, respectively, relative to the first upper side-band. The power amplifier's output power is very close to 2 Watt (+33 dBmW) for the whole output frequency band.

### 2.4.2 Receiver and demodulator

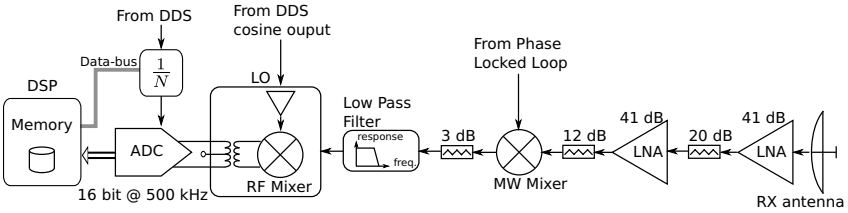


Figure 2.4.2: Receiver and demodulator.

Figure 2.4.2 shows the function blocks of one of the two receiver and demodulator chains. The first low noise amplifier (LNA) is connected directly to the antenna terminal without any intermediate cable. By changing the value of the coaxial attenuator between the LNAs the signal level entering the second LNA can be adjusted to avoid saturation. Increasing the attenuation can become necessary if the antenna side-lobe happens to illuminate a strong closely located scatterer.

The MW mixer is an ordinary double-balanced diode-ring mixer. It does *not* reject the image frequency band (5540 - 5680 MHz). Noise and disturbances in this frequency band will therefore mix directly into the signal band which is a clear disadvantage. We decided to accept the resulting increase in the noise and disturbance levels since implementing proper image rejection would significantly add to the complexity of the design. The MW mixer output is low-pass filtered to 180 MHz bandwidth.

The RF mixer demodulates the received and down-converted signal. It is an active mixer with a buffer amplifier integrated on the local oscillator (LO) port which is connected to the output signal from the DDS chip. The advantage is that the mixer output amplitude is almost insensitive to variations in the DDS signal amplitude.

As a part of the ADC input circuitry there is a transformer for changing the DC level to comply with the ADC specified input range. This transformer has the effect of a high pass filter and reduces the amplitude of low frequency components generated by closely located scatterers. Hence, closely located scatterers will not saturate the ADC. Even for long range scatterers generating high frequency components at the ADC's input, the ADC will only saturate if the antenna input is seriously over-driven. The second LNA will start to compress at a slightly smaller signal level than the ADC saturation limit. The LNA compression/saturation is however fairly soft compared to the ADC's hard clipping.

At the input of the ADC there is a low pass filter (not shown in figure 2.4.2) which eliminates folding of high frequency components. The ADC sample clocking is in phase-lock synchronization with the DDS chips signal generation. The ADC has a resolution of 16 bits and samples the input signal at 500 kHz. The digital samples are stored in the DSP memory.

### 2.4.3 Microprocessor, motor and power supply

The main controlling unit in GinSAR is a general purpose micro-processor system. It initialises the DSP and receive the data which may be stored in non-volatile memory. It is also in control of the motor that moves the antenna unit on the guide or on the rails. As it runs the Linux operating system, the radar can be controlled remotely if it is connected to a network. The radar also includes a power supply unit that generates all the needed voltage levels from on external 12 Volt supply. Figure 2.4.3 shows a schematic diagram of these units.

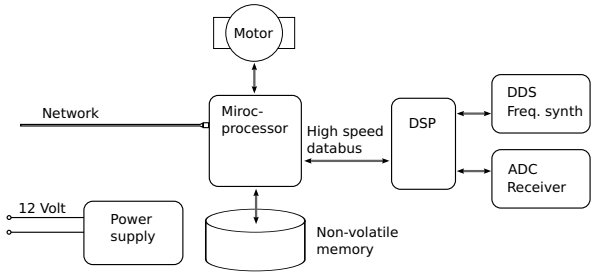


Figure 2.4.3: Microprocessor and power supply.

### 2.4.4 Antennas

Since the radar is simultaneously transmitting and receiving separate transmit and receive antennas were used. The antennas were mounted on a light and rigid aluminium structure. In the first GinSAR configuration the transmitter antenna was placed in the middle with the two receiver antennas below and above in line. In the second configuration the two antennas were placed next to each other horizontally. The separation in all cases was 0.85 meters. All antennas were standard back-haul telecommunication parabolic dish antennas designed for operation in the 5800 MHz band with a diameter of 0.60 meters. The specified gain was 27 dBi. In the first GinSAR configuration the polarisation was vertical, in the second horizontal. The polarisation could be changed by twisting the antenna feed horn 90 degrees. It was also possible to adjust the pointing direction both vertically and horizontally.

To reduce the direct cross-talk from the transmitter antenna to the receiver antenna, cylinders of radar absorbing material (RAM) were mounted around the dishes. The cylinders extended approximately 0.5 meters outwards from the dish rim. The RAM had 28 dB of specified return-loss for normal incident waves at 5800 MHz. The RAM sheets included metal backing. The direct cross-talk suppression from the transmitter to the receiver antenna has been measured to be better than

Figure 2.4.4: GinSAR antennas in the first configuration.

90 dB. This was more than sufficient to avoid the direct wave to saturate the receiver. Indirect measurements indicated that the RAM cylinders reduced the antenna gain to 25 dBi. Figures 2.4.4 and 2.4.5 show pictures of the antennas in the two configurations.

## 2.5 Choice of frequency

The centre frequency of GinSAR is $f_c = (\omega + \beta + \alpha t_c/2)/2\pi = 5790$ MHz, corresponding to a wave-length $\lambda = c/f_c = 51.8$ milli-meters where $c$ is the propagation speed of electro-magnetic waves. It has been chosen as a compromise between attainable accuracy, atmospheric attenuation, ease of construction and radio energy emission regulations.

**Accuracy** In a coherent radar system the range accuracy of a point scatterer is proportional to the phase accuracy of the measurement

$$\sigma_R = \frac{c}{2\pi f_c}\sigma_\theta \tag{2.5.1}$$

where $\sigma_R$ and $\sigma_\theta$ are the standard deviation of the range and the phase, respectively. The phase standard deviation $\sigma_\theta$ is related to the signal to noise ratio SNR

Figure 2.4.5: GinSAR antennas in the second configuration.

$$\sigma_\theta = \frac{1}{\sqrt{N \cdot \mathrm{SNR}}} \tag{2.5.2}$$

where $N$ is number of samples in one measurement. See appendix A for a derivation of equation 2.5.2. The attainable SNR will normally only decrease slowly with increasing frequency. Consequently, increasing the frequency will improve the range accuracy.

The cross-range accuracy will also improve with increasing frequency. The broadside cross-range angular diffraction limited resolution (angel between first zeros) is

$$\Delta\phi_{cr} = 2 \arcsin \frac{c}{M d f_c} \approx \frac{2c}{M d f_c} \tag{2.5.3}$$

where $M$ is the number of measurements on the aperture and $d$ is the distance between each measurement.

**Atmospheric attenuation** In a clear atmosphere the attenuation of electromagnetic (EM) waves for frequencies lower than 18 GHz is less than 0.1 dB/km, two-way [10, pp. 278-279]. It is smallest for the lowest frequencies. In heavy rain the attenuation can increase many times, and the increase factor is largest for high frequencies. For frequencies above the Ku-band, heavy rain will also noticeably

reduce the coherence of the wave due to Rayleigh scattering. At those target distances the ground-radar typically operates, we may conclude that there is a small advantage of using a low frequency. But for frequencies lower than 12 GHz the advantage is almost insignificant.

**Ease of construction** As the frequency increases the construction becomes more difficult. The tolerances become smaller, and the amount of available components decreases. But for frequencies less than 18 GHz component availability is not a big issue.

**Radio emission regulations** The chosen frequency band of GinSAR is within the one of the ISM bands. These ISM-bands are used for license-free error-tolerant communications like cord-less phones, local-area computer networks and radio controlled model aircrafts. The disturbance level is generally higher in the ISM-bands than in other licensed frequency bands. Choosing a frequency band outside the ISM-bands will in most nations require an EM-emission license.

## 2.6 Oscillator stability

In a repeat pass radar interferometry the phase difference between the two measurements is calculated. Normally it is assumed that any change in the measured phase for a given point scatterer is because of scatterer movement. But any change in the radar frequency between the two measurements will also generate an interferometric phase difference, and therefore represents a source of error. This phase difference can be expressed

$$\Delta\phi = 2\pi\left(\frac{2R}{\lambda_1} - \frac{2R}{\lambda_2}\right) = \frac{4\pi R}{c}(f_1 - f_2) = \frac{4\pi R}{c}\Delta f \tag{2.6.1}$$

where $\lambda_{1,2}$ and $f_{1,2}$ are the wave lengths and frequencies at the time for the two measurements. The phase and frequency differences can be replaced with the standard deviation of the same quantities

$$\sigma_\phi = \frac{4\pi R}{c}\sigma_f \tag{2.6.2}$$

Oscillator long term stability $\zeta$ is normally defined as the relative change in frequency. It is a dimension-less number usually expressed in parts-per-million (ppm)

$$\zeta = \frac{\sigma_f}{f}\cdot 10^6 \tag{2.6.3}$$

Here $f$ is the oscillator's nominal frequency and $\sigma_f$ is the standard deviation of the frequency measured over some specified time period. By solving equation 2.6.3 for $\sigma_f$ and inserting into equation 2.6.2 we get

$$\sigma_\phi = \frac{4\pi R}{c} f\zeta \cdot 10^{-6} \tag{2.6.4}$$

Using the relationship between interferometric phase $\Delta\phi$ and the change in range $\Delta$R

$$\Delta R = \frac{c}{4\pi f}\Delta\phi \tag{2.6.5}$$

the standard deviation of the range $\sigma_R$ becomes

$$\sigma_R = \frac{c}{4\pi f}\sigma_\phi = R\,\zeta \cdot 10^{-6} \tag{2.6.6}$$

The oscillator used in GinSAR has a specified long term stability of $\zeta = 0.3\,$ppm. per year. If we assume $R = 3000\,$m the range standard deviation becomes $\sigma_{\Delta R} = 0.9\,$milli-meters per year. In most applications this is acceptable but it shows the importance of an accurate oscillator.

In GinSAR the oscillator frequency can also be slightly adjusted by an external input voltage. Hence, if an order of magnitude more accurate reference oscillator is available, the frequency drift may be removed by synchronising to the reference.

## 2.7 Signal to noise ratio

The ability of the radar to accurately measure the magnitude and phase of a scatterer depends on the signal to noise ratio SNR. The signal power received by the receiver antenna $P_r$ is given by the radar equation [10, pp. 9-11]

$$P_r = P_t G_t G_r \frac{\lambda^2}{(4\pi)^3}\frac{\sigma}{R^4} \tag{2.7.1}$$

where $P_t$ is the transmitted power, $G_t$ and $G_r$ are the transmit and receiver antenna gains, $\sigma$ is the radar cross-section of a scatterer and $R$ is the range. In GinSAR $G_t$ and $G_r$ are equal.

The noise power referred to the receiver antenna terminal is given by [10, pp. 13-16]

$$P_n = kT_sB_W \tag{2.7.2}$$

where $k$ is Boltzmann's constant, $T_s$ is the system's noise temperature and $B_W$ is the effective noise bandwidth. Since the receiver signal processing is an implementation of a matched filter, it is not necessary to estimate $B_W$. The theory of the matched filter [97] states that the maximum attainable output SNR $= P_r/P_n$ is equal to the ratio of total received energy $P_r t_c$ to the noise spectral density $kT_s$. In practice the SNR will be reduced by a filter mismatch factor $L_m$

$$\text{SNR} = \frac{P_r t_c}{kT_s}L_m = P_t G_t G_r \frac{\lambda^2}{(4\pi)^3}\frac{\sigma}{R^4}\frac{t_c}{kT_s}L_m \tag{2.7.3}$$

In order to calculate the SNR for GinSAR we need numerical values for all factors in equation 2.7.3, $P_t = 2\,$W (section 2.4.1.3), $G_t = G_r = 316$ (section

2.4.4), $\lambda = 51.8$ milli-meters (section 2.5), $t_c = 15.358$ milli-seconds (section 2.3). The filter mismatch factor is estimated to $L_m = 0.63$ (2 dB).

The $\sigma$ and $R$-values are target dependent. The radar back-scatterer coefficient per unit area for natural terrain depends on incidence angle, surface roughness, vegetation, polarisation and frequency [98]. Here we will use $\sigma = 0.025\,\mathrm{m}^2$ and $R = 4$ km as a challenging example.

The system noise temperature $T_s$ is calculated by

$$T_s = T_A + T_0(N_F - 1) \tag{2.7.4}$$

where $T_A$ is the antenna noise temperature, $T_0 = 290$ K is the reference noise temperature and $N_F$ is the receiver's noise factor. Since the radar is illuminating the terrain it is reasonable to assume $T_A = T_0$. If $N_F = 5$ is used as an estimate, the system noise temperature becomes $T_s = 1450$ K.

Inserting into equation 2.7.3 gives SNR = 12.8. By using equations 2.5.2, setting $N = 1$ since the SNR calculated from equation 2.7.3 is for the whole measurement time $t_c$, we find $\sigma_\theta = 0.28$ rad. Using equation 2.5.1 the range standard deviations becomes $\sigma_R = 2.3$ milli-meter. Even in this rather difficult example the range standard deviation $\sigma_R$ is in most cases still acceptable.

This is the effect of the noise on one single measurement on the aperture given a single point scatterer. Since we have $M$ measurements on the aperture available, theory says the standard deviation will be reduced by a factor $1/\sqrt{M}$ if all measurements are added in phase. In practice there will be phase-errors among the terms and the improvement will be smaller but still important. We therefore conclude that the GinSAR design has sufficient SNR.

# Chapter 3

# Signal processing

## 3.1 System model

Figure 3.1.1 shows the coordinate system where the radar's position is used as reference. The origin is taken to be the position of the sledge/wagon on the linear guide/rails for the first measurement. The $x$-axis is parallel to the guide and ideally horizontal. The $y$- and the $z$-axis are both perpendicular to the $x$-axis and ideally horizontal and vertical, respectively. The $w$-axis is found by tilting the $y$- and $z$-axes an angle $\phi$ around the $x$-axis. The $\phi$-angle is the pitch angle of the antenna's pointing direction.

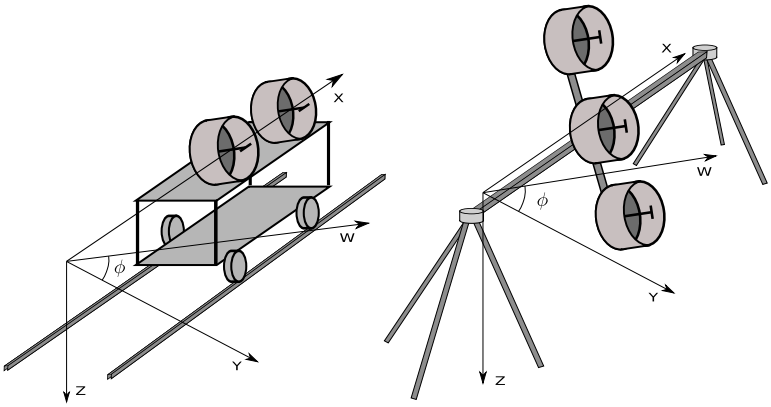


Figure 3.1.1: Coordinate system.

We will use ($x_{at}$, $y_{at}$, $z_{at}$) and ($x_{ar}$, $y_{ar}$, $z_{ar}$) for the position of the transmitter- and one of the receiver antennas, respectively and we will use ($x_t$, $y_t$, $z_t$) for the target position.

A linear single scatterer system model of the received signal is then given by

$$s_{RX}(t) = \int_{x_t}\int_{y_t}\int_{z_t} \sigma(x_t,\, y_t,\, z_t)\, s_{TX}(t - t_d)\, dx_t\, dy_t\, dz_t \tag{3.1.1}$$

where $\sigma\,(x_t,\, y_t,\, z_t)$ is the target area reflectivity function. $s_{TX}(t)$ is the transmitted signal and $t_d$ is the two way propagation delay.

The integration limits are given by the illuminated area. In a medium with constant propagation speed $c$, the propagation delay $t_d$ becomes

$$\begin{aligned} t_d &= \frac{1}{c}\Big(\sqrt{(x_t - x_{at})^2 + (y_t - y_{at})^2 + (z_t - z_{at})^2} \\ &\quad + \sqrt{(x_t - x_{ar})^2 + (y_t - y_{ar})^2 + (z_t - z_{ar})^2}\Big) \end{aligned} \tag{3.1.2}$$

Consequently $s_{RX}(t)$ is also a function of $(x_{at},\, y_{at},\, z_{at})$ and $(x_{ar},\, y_{ar},\, z_{ar})$. Since the antennas move on the linear guide/rails the positions of the antennas $(x_{at},\, y_{at},\, z_{at})$ and $(x_{ar},\, y_{ar},\, z_{ar})$ are functions of time. We will however approximate that the guide do not move during the measurement-sweep time $t_c$, see section 2.4.4. Hence, $(x_{at},\, y_{at},\, z_{at})$ and $(x_{ar},\, y_{ar},\, z_{ar})$ become functions of the integer sweep-number $m$. The stored measurement-sweep samples are denoted $s[n,\, m]$ where $n \in [0,\, N-1]$ is the ADC sample number and $m \in [0,\, M-1]$ is the position number along the linear guide, the sweep-number. Using equation 2.3.5 the model for the stored samples becomes

$$\begin{aligned} s[n,\, m] &= \int_{x_t}\int_{y_t}\int_{z_t} \sigma(x_t,\, y_t,\, z_t) \\ &\quad \times \cos\left(\alpha\, t_d\, n\Delta t - \frac{1}{2}\alpha\, t_d^2 + (\omega + \beta)\, t_d\right) dx_t\, dy_t\, dz_t \end{aligned} \tag{3.1.3}$$

where $t_d = t_d(m,\, x_t,\, y_t,\, z_t)$.

The same model applies to the samples stored by the second receiver channel in the first GinSAR configuration except for a different receiver position $(x_{ar},\, y_{ar},\, z_{ar})$.

## 3.2 SAR processing

The matched filter [97] is optimal in the sense that it maximizes the signal to noise ratio. Our approach is to implement the matched filter by correlating the measured signal $\hat{s}[n,\, m]$ with the analytical signal function [31] found from the system model in equation 3.1.3. We assume only one point scatter located in the position $(x_{ts},\, y_{ts},\, z_{ts})$

$$\sigma(x_t,\, y_t,\, z_t) = \delta(x_t - x_{ts},\, y_t - y_{ts},\, z_t - z_{ts}) \tag{3.2.1}$$

where $\delta(\cdot)$ is the spatial Dirac-impulse function.

The analytical signal is defined $\tilde{s} = s_I + \jmath s_Q$ where $s_I$ and $s_Q$ are defined by

$$s_I[n,\, m] = \cos\left(\alpha\, t_d\, n\Delta t - \frac{1}{2}\alpha\, t_d^2 + (\omega + \beta)\, t_d\right) \tag{3.2.2}$$

$$s_Q[n,\, m] = \sin\left(\alpha\, t_d\, n\Delta t - \frac{1}{2}\alpha\, t_d^2 + (\omega + \beta)\, t_d\right) \tag{3.2.3}$$

The complex correlation product $c_p(x_{ts},\, y_{ts},\, z_{ts})$ can now be calculated

$$c_p(x_{ts},\, y_{ts},\, z_{ts}) = \sum_{n=0}^{N-1} \sum_{m=0}^{M-1} \kappa[n,\, m](s_I[n,\, m] + j\, s_Q[n,\, m])\, \hat{s}[n,\, m] \tag{3.2.4}$$

where $\kappa[n,\, m]$ is a two-dimensional Kaiser window function [47]. In the numerical SAR processing the Kaiser window function argument is set to $\alpha_K = 5$ which reduces the side-lobe level to 36 dB relative to the main lobe at the cost of less spatial resolution. By repeating the calculation of $c_p(x_{ts},\, y_{ts},\, z_{ts})$ for a grid of uniform distributed target points in a plane defined by the $x$- and a $w$-axis (see figure 3.1.1) a complex SAR image is produced. We will use the following notation to denote the correlation product for the grid-points in the $x$-$w$ plane

$$c_p[k,\, l] = c_p(X_t + k\Delta x_t,\, Y_t + l\Delta w_t \cos\phi,\, Z_t - l\Delta w_t \sin\phi) \tag{3.2.5}$$

Here $k \in [0,\, K-1]$ and $l \in [0,\, L-1]$ are the target point sample numbers in the $x$- and $w$-dimensions respectively, $\Delta x_t$ and $\Delta w_t$ are the associated inter-point distances and $X_t$, $Y_t$, $Z_t$ are the target area origin coordinates. Normally calculation of target points outside the $x$-$w$ plane is not done because the poor vertical cross-range resolution.

The SAR magnitude image is found by the absolute value of the correlation product, $|c_p[k,\, l]|$. The SAR phase image is found by

$$\theta(k,\, l) = -\arctan\left[\frac{\Im m\{c_p(k,\, l)\}}{\Re e\{c_p(k,\, l)\}}\right] \tag{3.2.6}$$

The time domain SAR processing procedure outlined here is computationally intensive. For each target position the double sum in equation 3.2.4 must be evaluated. But using modern computers we have found that the processing time needed to do the SAR processing this way is in the order of minutes and therefore acceptable.

Frequency domain processing represents an alternative. A matched filter approach ($\Omega - k$ migration) is described in [65] (see appendix D), a tomographic approach is described in [43] (see appendix C). These procedures utilises the fast-fourier-transform (FFT) which may give orders of magnitude reduction in computation time. The main disadvantages are a required interpolation step in the procedure which will to some degree reduce the accuracy, and constrains in the radar positioning and target-point grid. In chapter 6 - Autofocus, the impact of these procedures with respect to autofocus will be discussed.

## 3.3 Interferometric processing

Interferometric processing of SAR images is an established technique for both air- and space-born and ground-based radars [64], [18], [51]. The application is twofold, to estimate the three-dimensional position of scatterers (generate DEM) and to estimate temporal range displacement of scatterers (terrain deformation, slope monitoring). In what follows only the fundamental processing steps are explained.

By definition an interferogram is calculated from two complex SAR images $c_A$ and $c_B$ [36]

$$\begin{aligned} g_{AB}[k,\, l] &= c_{pA}[k,\, l] \cdot c_{pB}[k,\, l]^* \\ &= |c_{pA}[k,\, l]| \cdot |c_{pB}[k,\, l]| \cdot \exp j(\angle c_{pA}[k,\, l] - \angle c_{pB}[k,\, l]) \end{aligned} \quad (3.3.1)$$

The phase of the interferogram $\theta_{2\pi}$ is proportional to the difference in propagation time $\Delta t_d$ between the two SAR images:

$$\theta_{2\pi}[k,\, l] = \angle c_{pA}[k,\, l] - \angle c_{pB}[k,\, l] = \Delta t_d[k,\, l]\, 2\pi f \bmod 2\pi \quad (3.3.2)$$

The $\bmod 2\pi$ operation gives a wrapping of the phase into $[-\pi,\, \pi]$ which has to be unwrapped before further processing. There are many reported unwrapping algorithms [33]. In this work we have first unwrapped the interferograms relative to coarse gradients and then manually unwrapped all finer details. The unwrapped phase is related to the wrapped phase by

$$\theta[k,\, l] = \theta_{2\pi}[k,\, l] + m[k,\, l]\, 2\pi \quad (3.3.3)$$

Here $m[k,\, l]$ is the integer found by the unwrapping procedure.

### 3.3.1 Three dimensional scatter positioning

In the horizontal cross-range and radial-range dimensions the synthetic aperture length and the signal bandwidth determine the resolution. If only one transmitter-receiver pair is available, however, there is essentially no resolution in the vertical cross-range dimension. To achieve some vertical cross-range resolution two receiver antennas placed above and below the transmitter antenna are used. This is the first GinSAR configuration, see figure 2.4.4 and the right part of figure 3.1.1.

The interferometric phase of a scatter calculated from the two receiver's SAR images is as described in equation 3.3.2 wrapped into a $2\pi$ interval

$$\theta_{2\pi} = 2\pi(\frac{\Delta r}{\lambda} - m) \quad (3.3.4)$$

where $m$ is the unknown integer sought by the unwrapping algorithm that bounds $-\pi < \theta_{2\pi} < \pi$, and $\Delta r$ is the range difference defined by

$$\Delta r = r_{Tx} + r_{Rx1} - (r_{Tx} + r_{Rx2}) = r_{Rx1} - r_{Rx2} \quad (3.3.5)$$

Here $r_{Tx}$, $r_{Rx1}$and $r_{Rx2}$ are the distances from the scatter to the transmitter and receiver antennas, respectively. Se figure 3.3.1.

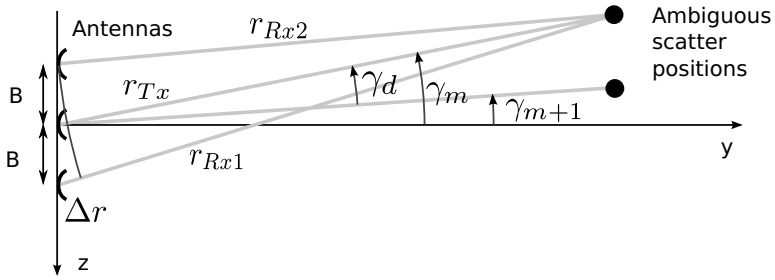


Figure 3.3.1: Ambiguous scatterers and distances to the antennas.

Since $\Delta r$ is defined to be a range difference, holding $\Delta r$ constant limits the scatter position to be on a hyperbola. The 3-dimensional scatter position can then be determined in combination with the range and horizontal cross-range scatter position.

Solving equation 3.3.4 for $\Delta r$ gives

$$\Delta r = \lambda \left( \frac{\theta_{2\pi}}{2\pi} + m \right) \tag{3.3.6}$$

Hence, a given measurement of $\theta_{2\pi}$ limits the scatter to be located on one of a family of hyperbolas given by the $m$-value. The associated scatter position ambiguity cannot be resolved by the radar itself. At practical target ranges the angle between two neighbouring ambiguous scatter positions can be approximated by $\gamma_d$ defined to be the angle between their hyperbola asymptotes. See figure 3.3.1. The angle between one ambiguous scatter position and the y-axis $\gamma_m$ is related to $\Delta r$ by

$$\Delta r_m = \lambda \left( \frac{\theta_{2\pi}}{2\pi} + m \right) = 2B \sin \gamma_m \tag{3.3.7}$$

Similarly, the angle to the neighbouring ambiguous scatter is related to $\Delta r$ by

$$\Delta r_{m+1} = \lambda \left( \frac{\theta_{2\pi}}{2\pi} + m + 1 \right) = 2B \sin \gamma_{m+1} \tag{3.3.8}$$

Since the $\gamma_d$-angles are small we approximate $\sin \gamma_d \approx \gamma_d$. By subtracting equation 3.3.8 from 3.3.7 and arranging we find

$$\gamma_d = \gamma_m - \gamma_{m+1} \approx \frac{\lambda}{2B} \tag{3.3.9}$$

Inserting $B = 0.85$ meter and $\lambda = 51.8$ milli-meter into equation 3.3.9 we find $\gamma_d = 30.5$ milli-rad.

If the radar looks up into a slope without any large overhangs, then within the

same azimuth resolution cell, the scatter elevation angle $\gamma_m$ must always increase with increasing scatter range. The scatter separation in range and terrain slope must be used to determine if the interferometric phase $\theta$ difference between two neighbour scatterers exceeds $2\pi$. In most practical situations $\gamma_d = 30.5$ millirad makes it possible to correctly determine the unknown integer $m$ (unwrap the phase) relative to other scatterers.

The vertical scatter positioning accuracy can be found expressing $\gamma_m$ as a function of $\theta_{2\pi}$ using equation 3.3.7 and setting $m = 0$

$$\gamma_m \approx \frac{\lambda}{2B} \frac{\theta_{2\pi}}{2\pi} \tag{3.3.10}$$

The vertical scatter positioning variance can therefore be found from the variance of $\theta_{2\pi}$ inserted into equation 3.3.10 and multiplied with the range.

There are many pixels in the interferogram which have large uncertainties in their phase values. A possible approach is to mask out these pixels in the construction of the DEM and instead calculate the elevation value at their positions by linear interpolation. We have chosen to identify the pixels with sufficiently certain phase values by a three part acceptance criteria. Those pixels that do not meet all three parts are masked out.

**First criteria** Only pixels with a coherency value larger than 0.8 are accepted. The coherency value is defined [30]

$$\rho_c[i,\, j] = \frac{E\left\{c_{pA}[i,\, j] c^*_{pB}[i,\, j]\right\}}{\sqrt{E\left\{c_{pA}[i,\, j] c^*_{pA}[i,\, j]\right\} E\left\{c_{pB}[i,\, j] c^*_{pB}[i,\, j]\right\}}} \tag{3.3.11}$$

The expectation operator $E\{\cdot\}$ is implemented as the spatial average of all pixels inside a small circle with the pixel $i$, $j$ in centre. In [36], section 4.3 there is given some support for using spatial averaging instead of ensemble averaging.

**Second criteria** The phase standard deviation of a 7 times 7 pixels (3.5 meters times 3.5 meters) patch of the interferogram, with the pixel in question in centre, has to be smaller than $\pi/5$ radians. The pixels removed by this second criteria are typically found on both sides next to strong scatterers in the cross range dimension. We believe the phase of the pixels in these positions are wrong because of some remaining uncompensated antenna trajectory movement. The zeros in the magnitude response of the two SAR images are not exactly at the same positions in the cross-range dimension, giving abrupt phase jumps in the interferogram.

**Third criteria** The average interferogram is found as the average of 7 subsequent measurements (the nominator in equation 3.3.11). Within this average only pixels with a magnitude larger than -40 dB relative to the overall maximum are accepted.

### 3.3.2 Temporal range displacement

If we assume constant propagation speed $c$ the range difference between two SAR images is proportional to the phase of the interferogram

$$\Delta r[k,\, l] = \frac{c}{4\pi f}\theta[k,\, l] = \frac{\lambda}{4\pi}\theta[k,\, l] \tag{3.3.12}$$

For equation 3.3.12 to be valid the two SAR images must be calculated from measurements where the radar antennas follow exactly the same path. In practice many measurements are taken during a campaign. For all subsequent SAR image pairs an unique interferogram is calculated. Throughout these interferograms some scatterers have sufficient high coherence for reliable range displacement estimation. The estimated range displacement of these scatterers is typically reported as colour-coded dots overloaded a digital elevation map or a photo of the target area, see [51] as an example.

The variance of the $\Delta r$-estimate due to additive noise (equation A.0.1) is found from the variance of the $\theta$-estimate (equation A.0.9)

$$\sigma^2_{\Delta r} = \left(\frac{\lambda}{4\pi}\right)^2 \frac{\kappa_w}{NM\,\mathrm{SNR}} \tag{3.3.13}$$

Here $\kappa_w$ is a Kaiser windowing weight factor. Using the values for $N$, $M$ and $\alpha_K$ given above $\kappa_w = 1.85$. In practice the variance of the $\Delta r$-estimate will be larger. The additional error sources are anomalies in the propagation speed due to changing atmospheric conditions, temporal changes of the scatterers and aperture focusing errors. These additional error sources are often dominating the measurement noise.

# Chapter 4

# Cable measurements

When doing tests with the complete radar to determine the accuracy, the results will depend on a number of factors such as internal electronic noise both in the transmitter and in the receiver, external noise and disturbances picked up by the receiver antenna, changes in the state of the atmosphere and instabilities in the positions of the antennas. In an effort to isolate the accuracy of the radar electronics we have conducted measurements where the antennas have been removed, and the transmitter amplifier has been connected directly to the receiver amplifiers by a long coaxial cable. The idea was to make a controlled environment without any free radiation suitable to determine the accuracy of the radar electronics itself.

The length of the coaxial cable was approximately 280 meters, the attenuation was specified to be 0.443 dB/meter for GinSAR's centre frequency and the propagation speed factor was 0.81 relative to free space. The total cable attenuation was therefore close to $L_{cab} = 124$ dB. At the receiver side the signal was split equally into both receivers, adding an additional $L_{split} = 4$ dB attenuation (1 dB excess splitter loss). Since the transmitted power was $P_t = +33$ dBmW (2 Watt), the signal power entering the receiver amplifier should therefore be $P_r = -95$ dBmW ($0.316 \times 10^{-12}$ Watt). This estimate was confirmed by direct measurements using a spectrum analyser. To avoid cross-talk between different cable sections the cable was rolled out on the ground outdoors with more than 2 meter separation at all points. In total 721 measurement-sweeps were recorded during a period of 155 seconds giving 4.7 measurements per second. The down-converted and digitised data were processed by the matched filter as described in section 3.2.

**Magnitude** Figure 4.0.1 shows the normalised magnitude of the response.

The range is scaled as if the propagation was in free air. Three curves are actually shown though almost identical. The middle red curve shows the measurement-sweep which is closest (in the mean square sense) to the average of all sweeps. The upper and lower blue curves shows the maximum and minimum response values for each range point. As can be seen the variation through all 721 measurement-sweeps were small. The recorded raw signals were not multiplied with any window-

function prior to the matched-filter processing.

Figure 4.0.2 shows the same measured normalised magnitude response as in figure 4.0.1 (red curve) and the theoretical response (blue curve) we would have had if there were no disturbances and noise.

The range between the first two minima for the real measurement response is approximately 2.27 meters, corresponding to an effective bandwidth of 132 MHz. The corresponding numbers for the theoretical response are 2.14 meters and 140 MHz. The deviation from the theoretical response is mainly due to declining transmitter power with increasing frequencies because of the inherent DDS output response (zero order hold) and subsequent low-pass filter roll-off.

**Phase** The accuracy of an interferometric SAR is determined by the system phase noise. In order to estimate the phase noise generated by the radar hardware itself we have used the phase value for all 721 measurement-sweeps at the maximum of the magnitude response, $R = 173.2$ meters. The ideal response would be a constant phase for all measurements. The red curve in Figure 4.0.3 shows an example of the measured phase value as a function of measurement-sweep number. The blue curve shows the filtered low frequency drift.

As can be seen, there has been a rather large unexpected low frequency drift in these phase measurements in addition to the expected high frequency noise. We believe this drift can be explained by thermal expansion of the cable. A phase change of 0.09 rad as shown corresponds to only 0.16 C degrees temperature change of the 280 meter cable-centre copper conductor[1]. Such small temperature changes can very well occur within 155 seconds considering that the cable was laying on the ground outdoor exposed to wind, sunshine and shadow. Additionally the electromagnetic power injected into the cable by the transmitter amplifier will mainly be converted to heat. And there will also be some direct heat conduction from the amplifier to the connected cable end.

In an effort to remove the contribution from thermal expansion and to be able to estimate the high frequency electronic noise magnitude, the calculated phase values were high-pass filtered. We used a finite impulse response (FIR) filter with 64 coefficients and a corner frequency of 0.28 Hz. In effect the blue curve in figure 4.0.3 has been subtracted from the red. The filter parameters were chosen as far as possible to keep the high frequency noise but at the same time remove low frequency drift. The resulting high frequency filtered phase is shown in figure 4.0.4. Because of FIR filtering end-effects, 32 samples have been removed in both ends .

The phase noise standard deviation in this figure is $\sigma_\theta = 2.8 \times 10^{-3}$ rad, corresponding to 0.012 milli-meters in range. By adding coaxial attenuators to the cable we were effectively reducing the signal-to-noise-ratio (SNR). The phase noise standard deviation $\sigma_\theta$ is related to the SNR by

$$\sigma_\theta = \frac{1}{\sqrt{N \cdot SNR}} \tag{4.0.1}$$

[1]Copper has a linear thermal expansion coefficient of $16.8 \cdot 10^{-6}\ \frac{1}{\mathrm{K}}$

| Added attenuation $L_{att}$ | Raw data SNR | SNR Raw data relative reduction | $\sigma_\theta$ [rad] | SNR Calculated from $\sigma_\theta$ | SNR relative reduction |
|---|---|---|---|---|---|
| 0 dB | 13.7002 | 0.0 dB | 0.0028 | 16.9353 | 0.0 dB |
| 10 dB | 1.3319 | 10.1 dB | 0.0087 | 1.7165 | 9.9 dB |
| 20 dB | 0.1408 | 19.9 dB | 0.0267 | 0.1862 | 19.6 dB |
| 28 dB | 0.0231 | 27.7 dB | 0.0708 | 0.0269 | 28.0 dB |
| 35 dB | 0.0071 | 32.9 dB | 0.1410 | 0.0067 | 34.0 dB |
| 40 dB | 0.0030 | 36.7 dB | 0.2669 | 0.0018 | 39.6 dB |

Table 4.0.1: Cable measurement results.

where $N = 7679$ is the number of samples in one trace. Equation 4.0.1 is derived in appendix A. By calculating $\sigma_\theta$ from the measurements such as shown in figure 4.0.4 the corresponding SNR is found from equation 4.0.1.

The SNR can also be calculated from the raw data directly. If there are $M$ measurements available, each with $N$ samples ($s_m[n]$, $n \in [1, N]$, $m \in [1, M]$), the noise power can be estimated by

$$P_\nu = \frac{1}{N} \sum_{n=1}^{N} \mathrm{var}(s_m[n]) \tag{4.0.2}$$

The variance is calculated between the $M$ measurements for each sample $n$. The signal power can be estimated by

$$P_s = \frac{1}{N} \sum_{n=1}^{N} \left( \frac{1}{M} \sum_{m=1}^{M} s_m[n] \right)^2 - \frac{P_\nu}{N} \tag{4.0.3}$$

Table 4.0.1 summarizes the measurement results. The first column shows the extra attenuation added to the cable. Column 2 and 3 show the SNR calculated from raw measurement data and the corresponding SNR reduction (in dB) relative to the first measurement where no attenuation was added. Column 4 shows the phase noise standard deviation $\sigma_\theta$. Column 5 shows the SNR calculated from $\sigma_\theta$ using equation 4.0.1. Column 6 shows the relative reduction in SNR (in dB) of column 5.

For 10, 20 and 28 dB added attenuations the calculated relative reductions in SNR of the raw data are almost equal to the added attenuations. For 35 and 40 dB added attenuations, it is lower than expected. This can be explained by the calculated signal power being too high because the noise due to the thermal expansion is correlated between the measurements.

The SNR calculated from $\sigma_\theta$ corresponds rather well with all the added attenuation values. Since $\sigma_\theta$ and the corresponding SNR is calculated from high-pass

| Added attenuation $L_{att}$ | Received power $P_r$ | SNR Calculated from $\sigma_\theta$ | System noise temperature $T_s$ |
|---|---|---|---|
| 0 dB | -95 dBmW | 16.9353 | 1708 K |
| 10 dB | -105 dBmW | 1.7165 | 1685 K |
| 20 dB | -115 dBmW | 0.1862 | 1553 K |
| 28 dB | -123 dBmW | 0.0269 | 1705 K |
| 35 dB | -130 dBmW | 0.0067 | 1368 K |
| 40 dB | -135 dBmW | 0.0018 | 1571 K |

Table 4.0.2: Calculated system noise temperature.

filtered phase measurements, the effect of the correlated thermal noise is removed. When comparing the SNR calculated from the raw data and from $\sigma_\theta$, the later is larger for added attenuation values except 35 and 40 dB. Ideally these two SNR calculations should be equal. In practice this is difficult to achieve because the SNR calculated from $\sigma_\theta$ depends on the corner-frequency used in the high-pass filtering. Since the frequency spectrum for the phase noise and thermal expansion noise partly overlap, there is no perfect corner frequency. In general a higher corner frequency removes more of the total noise and gives higher SNR.

The received signal level $P_r$ can be calculated as a function of added attenuation $L_{att}$:

$$P_r = P_t - L_{cab} - L_{split} - L_{att} \text{ [dB]} \tag{4.0.4}$$

The calculated $P_r$ values and the associated SNR values calculated from $\sigma_\theta$ in table 4.0.1 can be inserted into equation 2.7.3 and solved for the system noise temperature $T_s$

The mean system noise temperature $\bar{T_s} = 1598$ K indicating a noise figure $N_F = 5.5$. This is close to the estimate used in section 2.7. These cable measurements therefore confirm the calculations in that section.

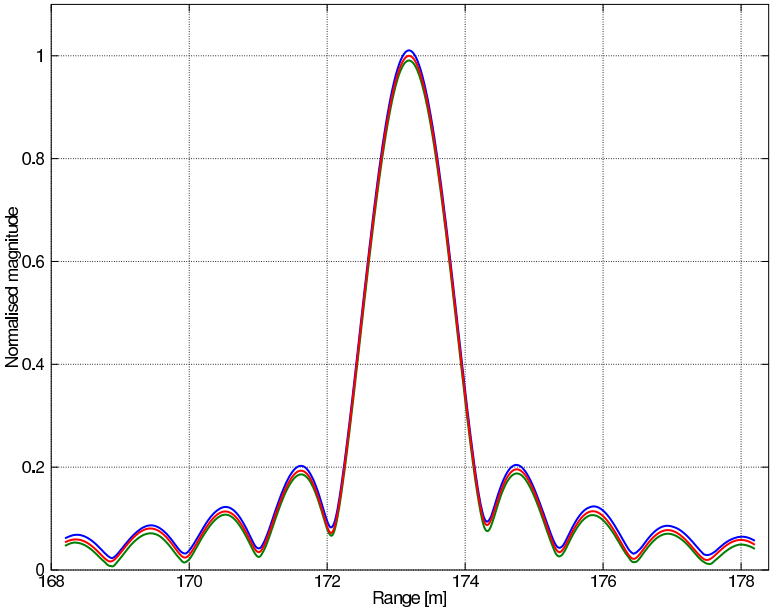


Figure 4.0.1: Magnitude response of cable measurement.

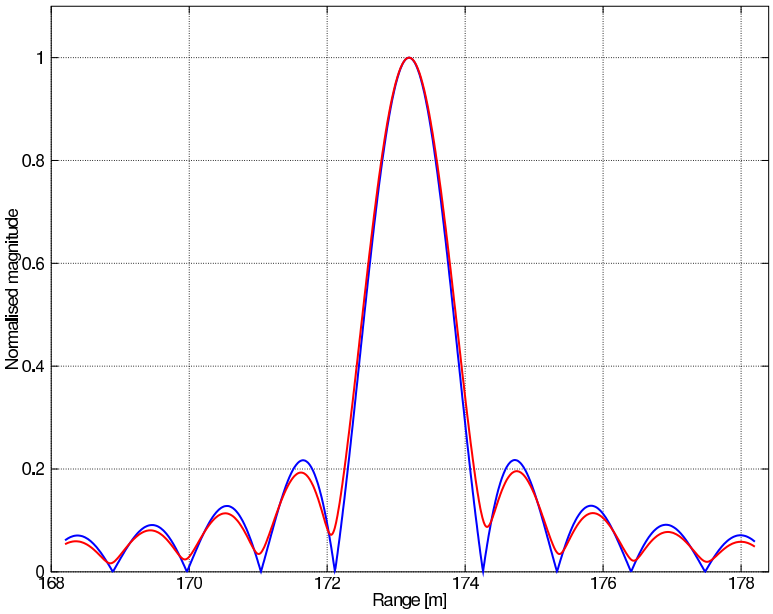


Figure 4.0.2: Actual and theoretical magnitude response.

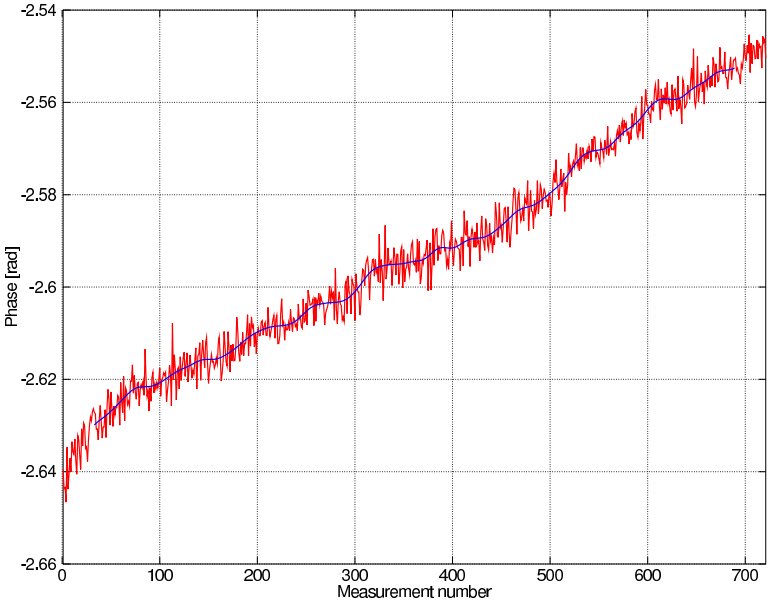


Figure 4.0.3: Phase at 173.2 meters as a function of measurement number.

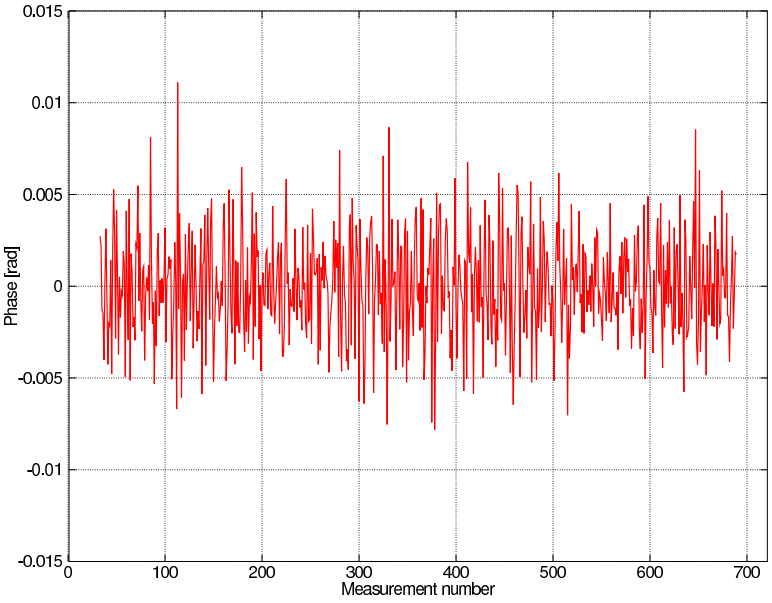


Figure 4.0.4: High-pass filtered phase noise as a function of measurement number.

# Chapter 5

# Linear guide measurements

## 5.1 Measurement description

Using GinSAR in the first configuration we have conducted measurements where the range from the radar to the target area was close to 2 km. The radar was placed on an open field in the bottom of a valley illuminating the top part of an alpine skiing slope. Three reflectors were set out in the target area , see table 5.1.1.

Reflector 1 was attached to a snow-cannon pipe using a threaded iron that pointed towards the radar. By screwing the reflector complete turns on the threaded iron the range could be adjusted with sub milli-meter accuracy. One complete turn corresponded to 1.75 milli-meters. Reflector 2 and 3 were of identical construction and they were not intentionally moved during the measurements. The stated radar cross sections (RCS) in table 5.1.1 are the theoretical maxima for the constructions and dimensions. The relative accuracy of the reflector positions is approximately 1 meters.

Totally 18 measurements were conducted. The first 4 measurements were con-

| Refl. No. | RCS [m²] | Altitude [m] | Range position [m] | Cross-range position [m] | Construction |
|---|---|---|---|---|---|
| 1 | 826 | 287 | 1922 | -9 | Flat plate reflector, adjustable |
| 2 | 104 | 296 | 1973 | -24 | Dihedral corner reflector, fixed |
| 3 | 104 | 298 | 1983 | -18 | Dihedral corner reflector, fixed |

Table 5.1.1: Reflector position and construction used in target area.

ducted before the reflectors were set out. The next 7 measurements were conducted with all reflectors in their initial constant positions. Before the last 7 measurements reflector 1 was adjusted 14 milli-meter towards the radar (8 complete turns). All measurements were conducted during a 12 hour period.

The linear guide design was intentionally meant to be rigid and linear. However, due to the weight of the antenna unit, the beam showed some bending and torsion. By using some simple measurement arrangements the bending and torsion were investigated as the antenna unit travelled along the guide. We concluded that the deviation of the antennas away from a straight line was very repeatable from one measurement to the next, and that the bending and torsion could be modelled by low order polynomials. Given the estimated bending and torsion the 3 dimensional deviation for each antenna were calculated. Finally, the deviations were compensated for in the SAR processing.

## 5.2 SAR magnitude image

Figure 5.2.1 shows an example of a processed SAR image (magnitude) measured after the reflectors had been set out. The colour scaling is in Decibel relative to the receiver saturation limit. If the resolution is measured as the distance between the first zeros, the cross-range resolution is approximately 70 meters and the range resolution is 4 meters. The SAR processing included a two-dimensional Kaiser-window with parameter 5, both these resolutions are therefore as expected given the bandwidth and synthetic aperture length.

Figure 5.2.2 shows a zoomed version around the reflectors. In addition to the reflectors a strong scatter at the coordinates (1967, -10) meters can be seen. This is most certainly a ski-lift mast in that position. Except for the reflectors and one or two other obvious scatterers the rather poor cross-range resolution makes it difficult to identify other scatterers with confidence. Figure 5.2.1 indicates that the open fields of the down-hill track have higher reflectivity than the surrounding forests.

## 5.3 Interferometric range

Figure 5.3.1 shows the interferometric calculated range $R$ at the 3 reflector positions as a function of measurement number.

The enforced movement of reflector 1 between measurement 7 and 8 is very clear. The close to parallel movement shown by all reflectors are due to changing atmospheric conditions. Appendix B derives the propagation time as a function of the state of the atmosphere (pressure, temperature and partial water vapour pressure).

As can be seen in figure 5.3.1 the total measured range span for reflector 2 and 3 is 5.9 milli-meters. Using the results from appendix B this positive span can be explained by only 2.5 K temperature drop, 0.65 hPa partial water vapour pressure increase or a 21.9 hPa total pressure increase. Official weather data measured

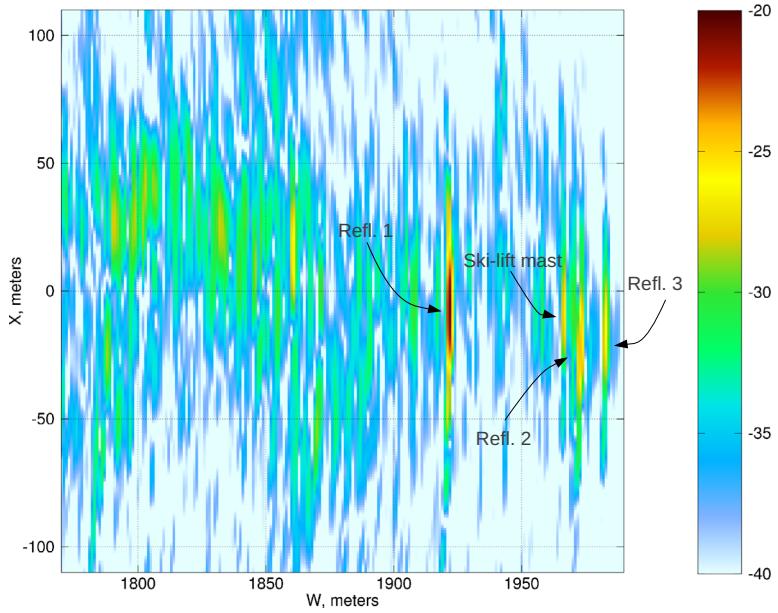


Figure 5.2.1: SAR magnitude image.

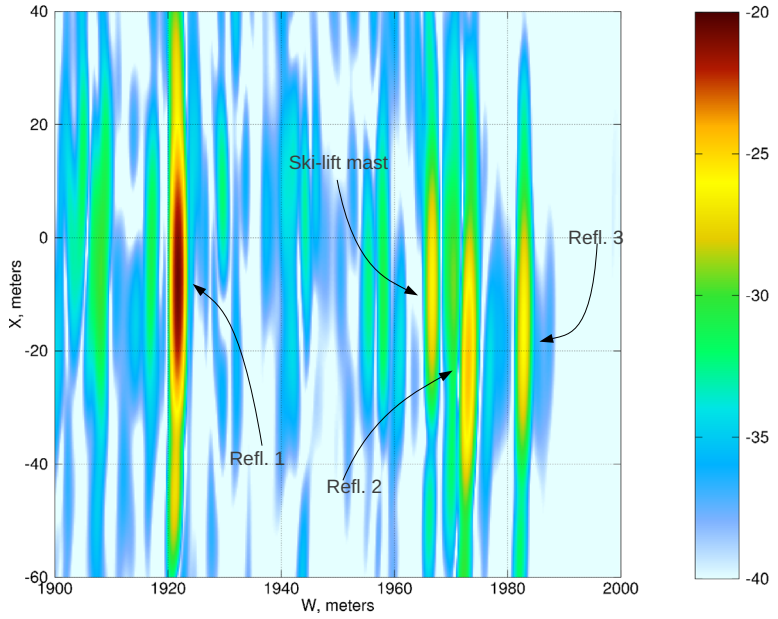


Figure 5.2.2: Zoomed SAR image around the reflectors.

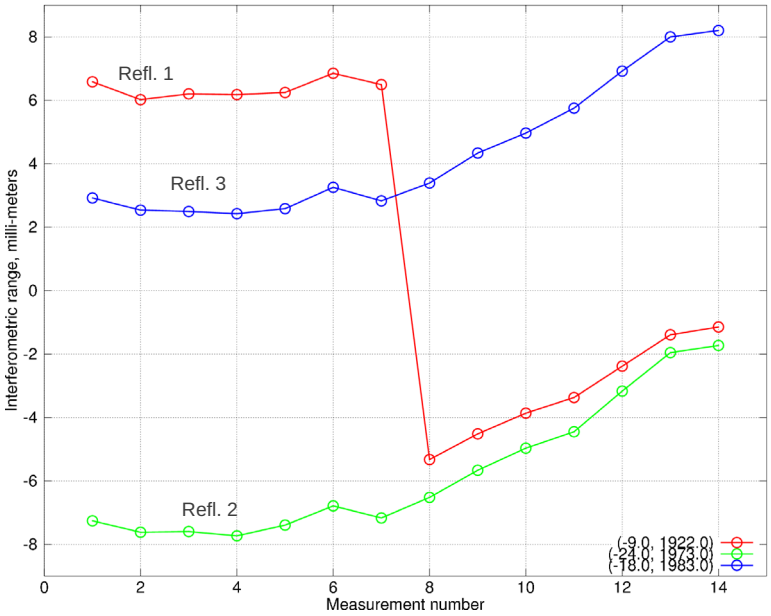


Figure 5.3.1: Interferometric range to the reflectors for all 14 measurements.

1 km. from the target area shows that the temperature did decrease with 2-3 K during the measurement period. The same data shows insignificant changes in vapour pressure and total pressure.

The calculated sensitivities in appendix B and these measurements show that changes in the state of the atmosphere is a major source of measurement error if not compensated. One possible remedial action is to define one reflector close to the target area as reference and measure the relative movement of the other scatterers. If reflector 3 is used as a reference the movement of the other reflectors are shown in figure 5.3.2.

The standard deviation of the relative range to reflector 2 is 0.10 milli-meter. The standard deviation of the relative range to reflector 1 before and after the adjustment is 0.08 and 0.28 milli-meter, respectively.

The measured adjustment of reflector 1 (difference between measurement number 7 and 8) is -12.4 milli-meter. This is considerably shorter than the actual adjustment of -14 milli-meter. The difference can be explained by the reflector being mounted on a snow-cannon which represents a significant fixed scatter by its own. We should therefore expect the measured adjustment to be a weighted average between the moved reflector and not-moved snow-cannon. The weights should be proportional to the magnitude of the scatterers. By comparing the scatter magnitude in this position before and after the reflector was set out the magnitude

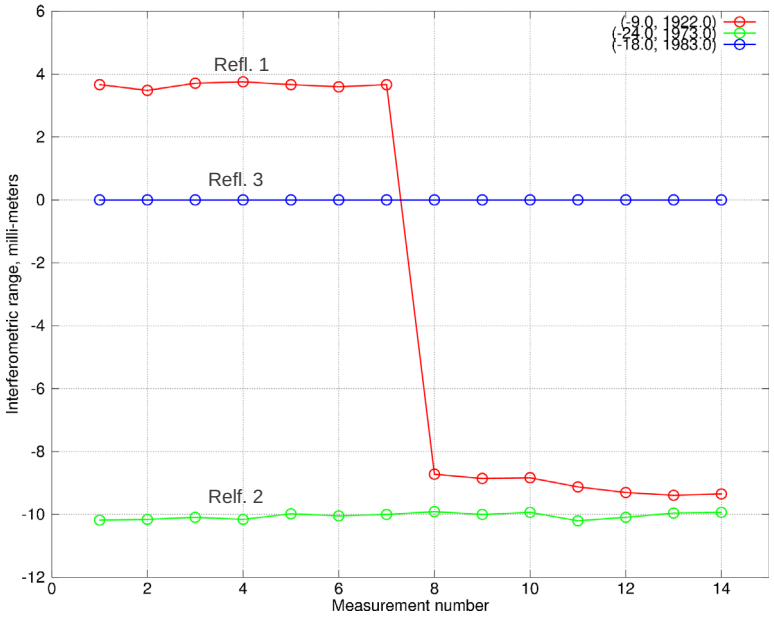


Figure 5.3.2: Interferometric range relative reflector 3 for all 14 measurements.

ratio is 7.5. Using this ratio the expected adjustment measurement becomes -12.1 milli-meter which is in good agreement with the measurement.

There are however, significant uncertainties with this estimate. When mounted the reflector hides part of the snow-cannon structure adding to the uncertainty of the 7.5 magnitude ratio. Any coupling between the reflector and cannon structure is also ignored. The contributions from the reflector and the cannon structure are added as vectors. The phase difference between these contributions before and after the adjustment will influence the total phase change. Although the experiment setup limits very accurate verification, the measured reflector movement agrees fairly well with the actual adjustment.

## 5.4 Digital elevation model

Figure 5.4.1 shows the unwrapped interferogram phase. By comparing with the SAR magnitude image in figure 5.2.1 the phase values at some patches on both sides of the strong scatterers in the cross range dimension have abrupt jumps. We believe, as explained in section 3.3.1, that the phase values in these positions are wrong and therefore must be removed before calculation of a digital elevation model. This is the purpose of the second criteria in section 3.3.1. Figure 5.4.2 shows the pixel mask calculated by all three criteria combined. The pixels in the

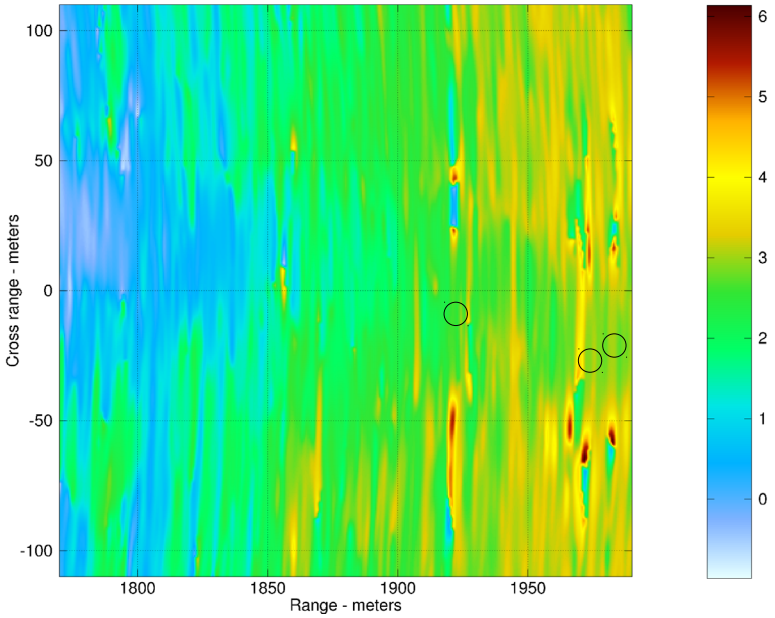


Figure 5.4.1: Interferogram phase in radians after unwrapping.

light areas are removed, as can be seen the majority of the pixels are removed.

Figure 5.4.3 shows a DEM map of all the pixels within the mask. The colour-bar scale is in meters above the radar.

In the construction of figure 5.4.3 the $\phi$-angle in figure 3.1.1 (the pitch of the antenna structure) has been included. To calculate the $\phi$-angle reflector 3 has been used as reference. The angle from reflector 3 seen from the radar to the $w$-axis can be found from the measured phase difference $\Delta\theta$

$$\gamma_{r3} = \arcsin \frac{\lambda \frac{\Delta\theta}{2\pi}}{2B} \tag{5.4.1}$$

Since the angle sum $\phi + \gamma_{r3}$ can be found directly from the position of the reflector (see table 5.1.1) the antenna pitch angle $\phi$ can be found by

$$\phi = \arcsin \frac{h_{r3}}{w_{r3}} - \gamma_{r3} \tag{5.4.2}$$

where $h_{r3}$ and $w_{r3}$ is the altitude and range to reflector 3.

The measured elevation of the reflector positions are given in table 5.4.1 together with their actual positions.

In the calculation of the pitch angle $\phi$, the altitude of reflector 3 was used as reference. Hence, the measured altitude for this reflector will be absolutely correct.

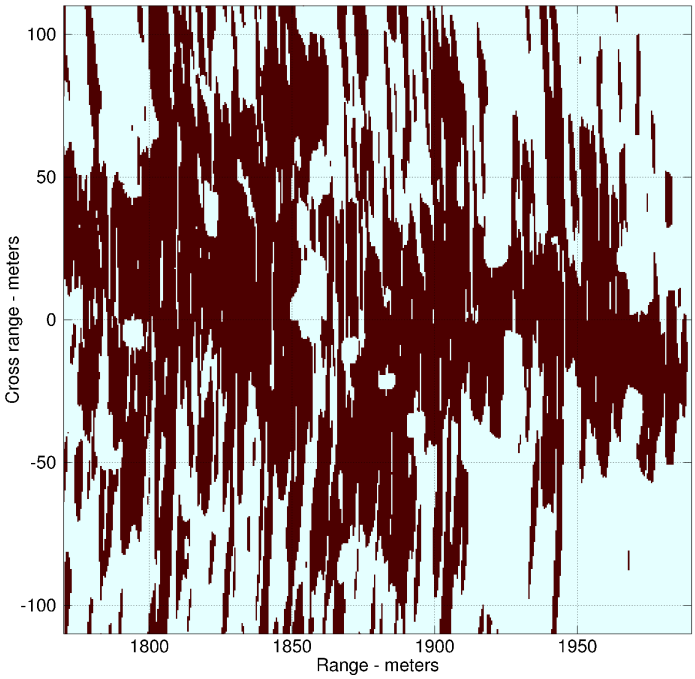


Figure 5.4.2: Pixel-mask for removing low quality pixels.

When comparing the measured altitude for reflector 1 and 2, they correspond fairly well to the correct altitude. It seems to be possible to determine the altitude of strong scatterers rather well.

Figure 5.4.4 shows the DEM where the masked out areas have been bi-linearly interpolated (2 dimensional quasi linear interpolation).

For some general position away from the reflectors we do not have accurate altitude references available, and are therefore forced to compare with available topographic maps and photos. The measured overall hill slope corresponds to the topographic maps. But there are smaller areas that are clearly wrong. At range 1460 and cross-range -10 meters, there appears to be a depression which is not there is reality. The peaks at 1922, -40 and 1922, +17 are also not correct. These peaks are on both sides of reflector 1 close to the first zeros in the cross-range response. Most of the pixels in these areas are removed by criteria 2 but apparently not all. In general there are significant differences between the measured DEM and the general map.

There are at least two explanations for the discouraging results. In section 5.1 we described how the linear guide beam showed some bending and torsion due to the weight of the antenna unit and the compensation procedure applied. Since the

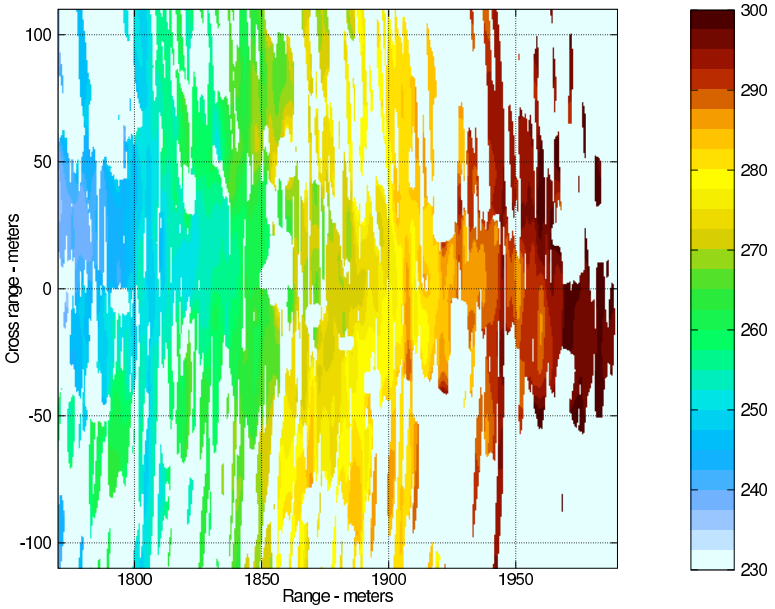


Figure 5.4.3: Digital elevation model.

| Refl. no | Range position [m] | Cross-range position [m] | Altitude [m] | Measured altitude [m] |
|---|---|---|---|---|
| 1 | 1922 | -9 | 287 | 285 |
| 2 | 1973 | -24 | 296 | 295 |
| 3 | 1983 | -18 | 298 | 298 |

Table 5.4.1: Reflector elevations

measurements used in the estimation have limited accuracy, there will be some uncompensated antenna deviations from straight and parallel lines. In particular, any uncompensated torsion will affect DEM calculations directly. The magnitude of these uncompensated deviations are difficult to assess directly from the estimation procedure but even small deviations are significant. At 2 km. range an uncompensated torsion deviation of 1 milli-meter at the antennas give an altitude error of almost 1.2 meters.

The cross-range resolution of GinSAR in this first configuration is approximately 70 meters (distance between the first zeros in the response when a window function is included in the processing). The calculated elevation will be a weighted average of the resolution cell removing finer details. To improve the DEM usefulness higher cross-range resolution is clearly needed. In addition accurate SAR image focusing prior to interferogram calculation, and the selection of low quality

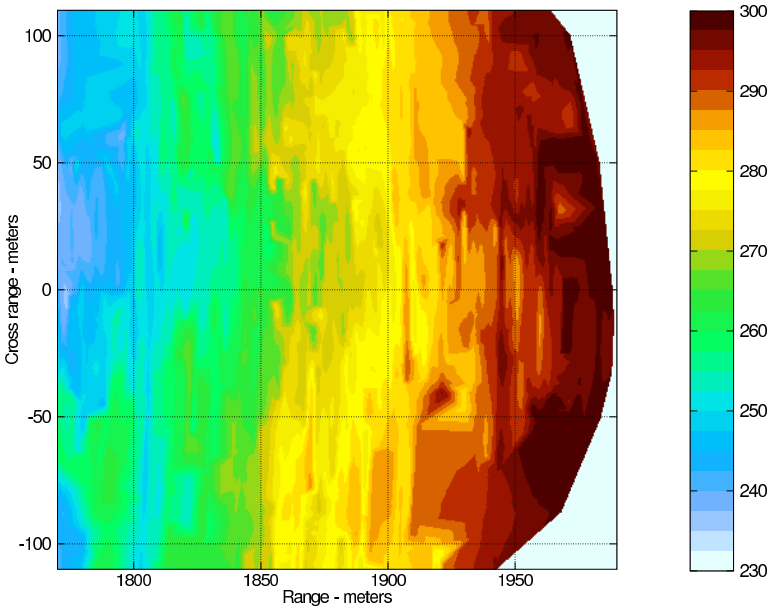


Figure 5.4.4: Interpolated digital elevation model.

pixels to be masked out, needs careful attention.

# Chapter 6

# Introduction to Autofocus

If it is assumed that there is only one point scatterer in the scene, the signal received by a SAR on each position on the synthetic aperture is a time-delayed version of the transmitted signal. The delay is proportional to the distance from the position on the synthetic aperture to the scatterer and inversely proportional to the propagation speed. The basic idea of the SAR processing is to add a calculated time-delay to the received signal at each position on the synthetic aperture, such that they all get a common uniform delay. The signals are then added together. This procedure requires that the time-delay at each position on the synthetic aperture can be accurately calculated. Thus, the assumed positions along the aperture and the assumed propagation speed must be correct. If there are varying errors in these assumptions, the signals added will not be in phase resulting in a defocused image. Autofocus procedures take a SAR image, which to some extent is defocused, and estimates the errors in the time-delay along the aperture. The estimated errors can then be applied in a new SAR processing to generate a better focused image.

## 6.1 Causes of defocus

The most important cause of phase errors are uncompensated movement of the radar antenna along the synthetic aperture. A second cause is errors in the assumed EM-wave propagation speed.

**Satellite SAR** Satellites orbiting the earth follow tracks that can be calculated rather well by Kepler's equations. Deviations are mainly due to the flattening of the earth, uneven mass distribution within the earth, gravity attraction by the moon, air resistance and solar radiation pressure. The resulting orbit anomalies have very low frequency. Normally the orbit anomalies are so accurately measured by other sensors that autofocus is not needed. Since the time a point on the surface is illuminated by a satellite SAR is typically less than 1 second, there are practically no contemporary changes in the propagation speed through the

atmosphere. The spatial changes in propagation speed from all positions along the aperture are also almost always negligible since the lines from a scatterer to the end-positions on the synthetic aperture are almost parallel.

**Aircraft SAR** Even if the pilot tries to fly in a straight line the deviations will typically be in the range of meters due to wind and turbulence. Some of the deviation can be measured. The most accurate instruments for this purpose are satellite navigation receivers tightly integrated with inertial navigation systems. Even after the measured deviation is compensated, significant residual position error remains. Hence, the aircraft SAR normally depends on autofocus algorithms to produce high quality SAR images. The target point exposure time varies from 10 to 200 seconds depending on range and aircraft speed. The synthetic aperture length can be many kilo-meters. Changes in the propagation speed as a function of position on the synthetic aperture must therefore be expected, adding to the need for autofocus procedures.

**Ground SAR** The position of a ground SAR moving on a rigid linear guide is normally known very accurately. The time needed to complete all measurements along the synthetic aperture may be as long as 10 minutes. Some changes in the propagation speed may occur during this time interval, and the ground radar may benefit from autofocus algorithms in this case. But normally the changes are insignificant and autofocus is therefore not needed.

As described in section 1.1.4 the position of the ground radar moving on rails is not very accurately known and therefore depends on autofocus to produce high quality SAR images. In this respect it resembles the aircraft SAR although the residual error is usually much smaller. The measurement time can be up to 10 minutes which adds to the need for autofocus.

## 6.2 Defocus effects

In the most general case the position error at one position on the synthetic aperture is a 3-dimensional vector from the nominal position to the actual position. By including the error in the assumed propagation speed a resulting 3-dimensional time-delay error vector can be defined. For a fixed target point the time delay error will be the time-delay error vector projected into the line-of-sight (LOS) vector. Ideally all 3 components of the time-delay error vector should be estimated since the LOS direction varies over the target area and with position on the synthetic aperture. But normally the antenna lobe width is so small that the defocus sensitivity for more than one dimension is small. Hence, almost all autofocus algorithms limits the estimation of the error vector to a scalar time-delay error common to all target points. Estimating more than one dimension may be justified if the LOS direction varies much over the target area. This may be the case in some low altitude strip-map mode SARs [95].

Since most SARs have a small relative bandwidth the scalar time-delay error $\Delta t_\epsilon$ may be replaced by a phase error

$$\Delta\phi_\epsilon = 2\pi f_c \Delta t_\epsilon \tag{6.2.1}$$

But adding the phase error $\Delta\phi_\epsilon$ to the phase of the analytical signal defined in equation 3.2.2 and 3.2.3 instead of adding the time-delay error $\Delta t_\epsilon$ to the time variable is only justified within limits. The range error corresponding to the time-delay error $\Delta R_\epsilon = c\Delta t_\epsilon/2$ must be much smaller than the range resolution. If $\Delta R_\epsilon$is equal or larger than the range resolution the analytical signal $\tilde{s}$ will not correlate with the measured signal $\hat{s}$ in equation 3.2.4. The range resolution is given by

$$R_r = \frac{c}{2 * B_w} = \frac{c\pi}{\alpha t_c} \tag{6.2.2}$$

In the second part of equation 6.2.2 the bandwidth expressed by the chirp parameters $\alpha$ and $t_c$ has been substituted, $B_w = \alpha t_c/(2\pi)$. By expressing the range resolution as the corresponding interferometric phase $4\pi R_r/\lambda_c$ we must demand that

$$\Delta\phi_\epsilon \ll \frac{4\pi R_r}{\lambda_c} = \frac{4\pi^2 f_c}{\alpha t_c} \tag{6.2.3}$$

for equation 6.2.1 to be valid. For GinSAR the range resolution is $R_r = 1.07$ meters while the uncertainty of the radar position is at most only some tens of mili-meters. Using the phase error $\Delta\phi_\epsilon$ instead of the time-delay error $\Delta t_\epsilon$ is therefore justified.

**Constant equal phase errors** As previously described the single point scatterer signal from all positions on the synthetic aperture must have a common uniform delay before summation to produce a correctly focused image. If the phase errors are equal along the synthetic aperture, we still have a common uniform delay and we will get a correctly focused image. Only the image phase will be different. The constant phase error cannot be estimated by any autofocus procedure which uses the image alone. Any constant phase error will therefore propagate unnoticed to the interferometric processing.

**Linear phase errors** Phase errors that are described by a linear function along the synthetic aperture, have the same effect as if the synthetic aperture was twisted a small angle. The whole target scene will appear sidewise shifted but otherwise well focused. An autofocus procedure which uses the image alone will not be able to estimate such linear phase errors. The linear phase error difference between two images can, however, be estimated by interferometric processing [84].

**Second degree and higher order phase errors** Phase errors functions of this type will defocus the SAR image. The degree of defocus varies with the

magnitude of the phase errors and the phase error function along the synthetic aperture. Figure 6.2.1 shows a simulation of the cross-range response of a point target where the phase error function is quadratic.

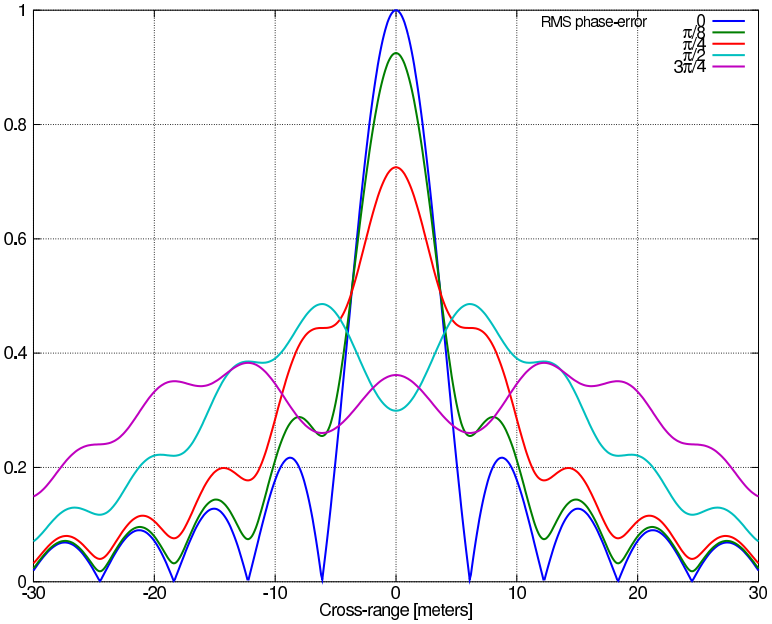


Figure 6.2.1: Cross-range response for different quadratic RMS phase error levels.

This simulation uses parameters taken from GinSAR in the second configuration, i.e. the length of the synthetic aperture is 12.133 meters, there are 721 measurement positions along the synthetic aperture and the point target is located at a range of 2859 meters centred in front of the radar. As can be seen increasing root-mean-square (RMS) phase errors lowers the peak response and increases the width of the cross-range response. If there were many scatterers, the SAR magnitude image would have appeared to be blurred in the cross-range dimension.

Figure 6.2.2 shows an equal simulation, but where the phase error function along the synthetic aperture is white noise Gaussian distributed.

For small phase errors the reduction in peak response is similar to the quadratic case. For RMS phase-error equal to $\pi/2$ the peak response is smaller, but the cross-range width increase is less pronounced. The "blur" appears to be further spread out and have a smaller magnitude close to the target position.

The effect in the range dimension is merely a reduction in the peak response as long as the equivalent range error is a small fraction of the range resolution. Figure 6.2.3 shows the simulated SAR magnitude image without any phase errors

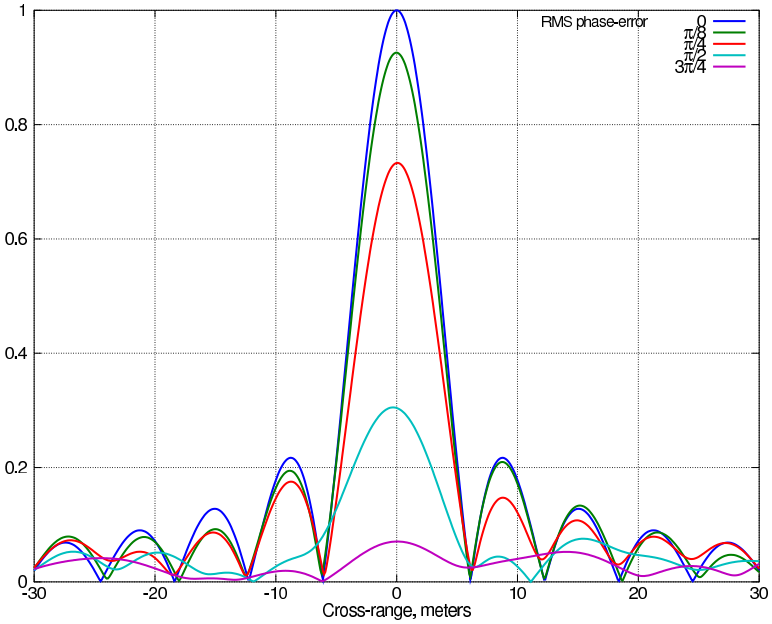


Figure 6.2.2: Cross-range response for different Gaussian white noise RMS phase error levels.

and with a $\pi/2$ radians quadratic RMS phase error function. As can be seen, resolution loss is almost exclusively limited to the cross-range dimension.

## 6.3 Basis for autofocus algorithms

**Scalar LOS phase approximation** As described in section 6.2, if the antenna lobe width is relative small, it is a justified approximation to limit the estimation procedure to a scalar for each position on the synthetic aperture. The lobe width of the GinSAR antennas is less than 10 degrees and therefore meets this requirement. We will also approximate the time-delay error with a phase error. Inserting numerical values for GinSAR on the right side of equation 6.2.3 gives $\Delta\phi_\epsilon \ll 260.0$ rad which corresponds to an equivalent position error $\Delta r_\epsilon \ll 1.07$ meters. Since the expected position error when the radar moves on the rails is at most some tens of milli-meters, the approximation is justified.

The estimated phase error can be converted to an equivalent scalar position error. If the centre of the target area is located at a squint angle $\vartheta$ relative to the broadside of the synthetic aperture, the equivalent estimated position error will be along the LOS and not perpendicular to the synthetic aperture. Notice that the

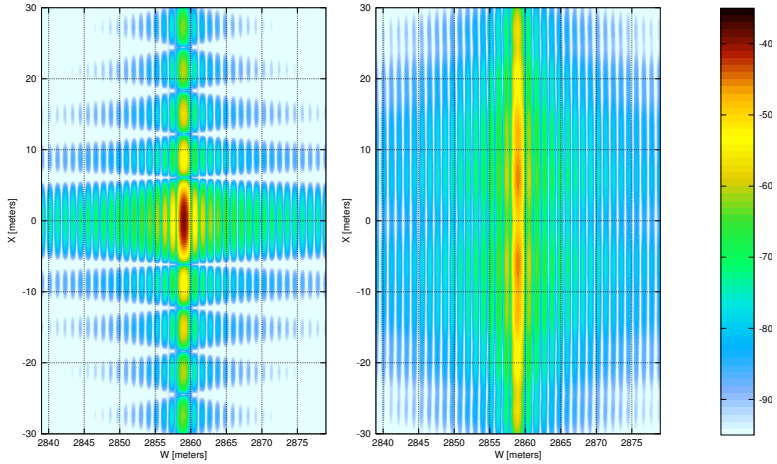


Figure 6.2.3: SAR magnitude image without any phase error (left) and with $\pi/2$ radians quadratic RMS phase error (right).

effective synthetic aperture length is a factor $\cos\vartheta$ shorter than the real aperture length. The cross-range resolution therefore will decrease by $1/\cos\vartheta$.

**Autofocus dimension** Equations 3.2.4 and 3.2.5 states the complex correlation product that defines the matched filter for the indexes $k$ and $l$ into the target area. It is rewritten here with some modifications.

$$c_p[k,\, l] = \sum_{m=0}^{M-1} \left( \sum_{n=0}^{N-1} \left(\tilde{s}[n,\, m][k,\, l]\right) \hat{s}_0[n,\, m] \right) \exp \jmath \Delta\phi_e[m] \tag{6.3.1}$$

The received signal $\hat{s}$ in equation 3.2.4 has been factorised into the signal we would have received if there were no phase errors $\hat{s}_0$ and the phase error exponential $\exp \jmath\Delta\phi_e[m]$. The kaiser window function $\kappa$ has been removed for simplicity. To underline that the matched filter signal $\tilde{s}$ is a function of target area position, the $[k,\, l]$ function indexes has been added.

As shown in section 6.2 phase errors will mainly defocus the SAR image in the cross-range dimension. To emphasis this fact equation 6.3.1 can be rewritten in vector-form for one range line

$$\boldsymbol{c}_p[l] = \exp(\jmath \boldsymbol{\Delta\phi}_e)\, \boldsymbol{F}[l] \tag{6.3.2}$$

where $\boldsymbol{c}_p[l] = [c_p[0,\, l],\, c_p[1,\, l],\, \ldots,\, c_p[K-1,\, l]]$ is the SAR range line vector $l$, and $\boldsymbol{\Delta\phi}_e = [\Delta\phi_e[0],\, \Delta\phi_e[1],\, \ldots,\, \Delta\phi_e[M-1]]$ is the phase error vector along the aperture. $\boldsymbol{F}[l]$ is a $M \times K$ matrix where element $[m,\, k]$ is given by

$$F_{m,\,k}[l] = \sum_{n=0}^{N-1} \left(\tilde{s}[n,\,m][k,\,l]\right) \hat{s}_0[n,\,m] \tag{6.3.3}$$

Equation 6.3.2 shows that each range line of the defocused SAR image (each $l$) is the phase error vector exponential multiplied with a matrix $\boldsymbol{F}[l]$ which is a function of the range line $l$. This matrix is defined from $\hat{s}_0$, the signal we would have received if there were no phase errors and therefore unknown. If the distance between the range lines exceed the range resolution, each range line can be regarded as independent. Since each defocused range line is defocused by the same phase error vector, each range line therefore provides independent information that can be used to estimate $\boldsymbol{\Delta\phi}_e$.

The $K \times L$ dimensioned defocused image is defocused by an $M$-dimensional phase error vector where each element is defined in the interval $[0,\, 2\pi]$. The perfect focused image is therefore some point in this $M$-dimensional space, and the autofocus task may be regarded as a $M$-dimensional optimisation problem.

This $M$-dimensional space may be expressed in an basis spanned by orthogonal Lagrange polynomials such that each Lagrange function constitutes an unit vector in an independent dimension. Then the first two Lagrange functions correspond to the constant and linear phase error functions. As discussed in section 6.2, these two dimensions cannot be estimated by an autofocus procedure that uses the SAR image alone. By using Lagrange functions as basis, the search space dimension may therefore be reduced to $M - 2$.

**Accuracy** As shown in figures 6.2.1 and 6.2.2 small phase error causes only small changes in the magnitude SAR image. Most scatterers will still be easy to identify. An autofocus algorithm which reduces the phase error to less than $\pi/4$ will give a SAR magnitude image which in most cases reveals a necessary detail level.

If the SAR image shall be used in interferometric processing, the main concern is the residual phase error. Surprisingly, only the constant and the linear phase error functions actually changes the phase at the position of a single point scatterer. For all higher (Lagrange) order phase error functions the phase error sum is zero. But even if the constant and linear phase error functions cannot be estimated by autofocus procedures working only on the SAR image alone, autofocus is still needed for two reasons.

First, defocus reduces the signal power and consequently the SNR at the position of a single point scatterer. The variance of the phase estimate will therefore increase according to equation 2.5.2. Second, the measured phase at the position of one point scatterer also includes contributions from other close scatterers. Second degree and higher order phase error functions increase the width of all scatterers. At the position of the point scatterer we are studying, the phase contribution from close scatterers will therefore increase and introduce a phase error. It is only at the position of a single point scatterer that a second or higher order phase error function does not change the phase. In all other cross-range positions the phase generally changes.

Interferometric processing benefits from accurate autofocus. In most applications phase errors translates directly into errors in the end product such as a DEM or slope movement maps.

**Necessary assumptions** For autofocus procedures to work, some assumptions must be made on the properties of the correctly focused SAR image. If we cannot make any assumptions, then all images have an equal probability making it impossible to decide if a correction improves the focus. The autofocus procedures tries to estimate the phase error function such that the resulting SAR image is in better accordance with the assumed properties. The assumed properties varies to some degree between different algorithms.

A number of algorithms (see sections 6.4) assumes there are some dominating point scatterers in the scene and treats other scatterers as noise. The rational behind this assumption is that if there is only one point scatterer in the scene, the phase error function would be the phase difference between all positions on the synthetic aperture before the last summation step in the SAR processing. A second approach is to regard autofocus as an optimisation problem where some image contrast objective function is optimised. A third alternative is to assume that in some areas of the target area, the reflectivity is zero.

## 6.4 Existing autofocus algorithms

### 6.4.1 Frequency domain SAR processing and autofocus

Many of the following algorithms assume that the SAR processing is done in the frequency domain instead of directly in time domain as is done for GinSAR, described in section 3.2. By itself frequency domain processing using the fast Fourier-transform (FFT) is generally much faster than time domain processing. For large datasets the computational time needed to do time domain processing is practically too long. For GinSAR which is imaging a relative small area, the computational time is acceptable. The disadvantages with frequency domain processing are some small reduction in accuracy because of a necessary interpolation step, and that the distance between points in the image and on the synthetic aperture must be regular and uniform. In appendix C and D a brief introduction to tomographic formulated SAR processing and frequency domain matched filter (FDMF) SAR processing are given. They include descriptions on the limitations and necessary approximations taken. This section discusses the implications of frequency domain processing on autofocus algorithms.

#### 6.4.1.1 Tomographic formulated SAR processing without interpolation

If the target area size is very small relative to the range to the target area, the tomographic formulated SAR processing, even without the interpolation steps, will be fairly accurate. In this case the processing consists of the following steps

1. De-ramping upon reception (Multiply the received signal with a copy of the transmitted chirp-pulse, often done in hardware)

2. Inverse Fourier-transform (IFFT) in range

3. IFFT in cross-range (azimuth)

The first two steps only involve data recorded from single radar positions on the aperture, there are no mixing of data between different radar positions. At one single radar position a phase error has the effect of multiplying the ideally correct data with a complex constant of unit length. If the data is stored in a matrix where each column holds data from one single radar position, then each column is multiplied with a phase error constant. The multiplication with a constant is invariant through the first two steps. After these two steps we say the data are in the range-compressed Doppler domain. This domain and the image domain are Fourier-transform pairs in cross-range (step 3). If we have an estimate of the phase error vector which we would like to include in the SAR processing, it is sufficient to multiply the estimated phase error vector with the associated columns of the data matrix before computing IFFT in cross-range, it is not necessary to redo all SAR processing steps.

In the range-compressed Doppler domain, each element of the phase error vector can be determined if the phase of the ideally correct data vectors are known. In the case where we know there is only one single point scatterer in the azimuth centre of a range line in the image, the cross-range FFT of that line shall ideally give a constant function in the range-compressed Doppler domain. Hence, any deviation from a constant function can be used to estimate the phase error vector. Or more precisely, the phase of the resulting function is the phase error function to within a constant. Autofocus algorithms based on frequency domain SAR processing assumes there is a one-to-one relationship between one radar position on the synthetic aperture and one column in the data matrix before the IFFT in cross-range. It is important to notice that this is only at best an approximation.

The tomographic formulated SAR processing described in appendix C includes two interpolation steps, first in range and second in cross-range. These steps are needed to increase the SAR image accuracy which is particularly important if the image shall be used in interferometric processing. The last interpolation step in cross-range breaks the one-to-one relationship between one radar position on the synthetic aperture and one column in the data matrix. We are then forced to inter- and extrapolate the estimated phase errors if the radar position error at the actual measurement positions are needed. Even with the interpolation steps included, the tomographic formulated SAR processing has limited accuracy due to the approximations taken in the derivation. It may therefore be rejected all together when the size of the target area is substantial compared with the range to the radar as is normally the case for GinSAR.

#### 6.4.1.2 Frequency domain matched filter SAR processing

Frequency domain matched filtering (FDMF) as described in appendix D makes it possible to do SAR processing in the frequency domain without loss of accuracy. The processing steps are

1. The measured signal matrix is Fourier-transformed in both range and cross-range dimensions
2. The transformed signal is multiplied with the Fourier-transform of a centred point scatterer
3. The product matrix is interpolated in range such that the spatial frequency samples have uniform separation
4. The interpolated matrix is inverse Fourier-transformed in both range and cross-range (azimuth)

Since the order of the IFFTs in step 4 is arbitrary, we may choose to do IFFT in cross-range last. In this respect FDMF fits into the framework of frequency domain autofocus. But as stated in section 6.4.1.1 autofocus algorithms based on frequency domain SAR processing assumes there is a one-to-one relationship between one radar position on the synthetic aperture and one column in the data matrix before the IFFT in cross-range. In this section we will identify the ways the cross-range Fourier-transform of the FDMF SAR image differs from the ideal assumed by frequency domain autofocus. A more detailed treatment of this subject with special focus on phase-gradient autofocus (PGA) can be found in [99].

**Limited support in Doppler domain** If there is only one point target located in the azimuth centre of a scene, the associated magnitude of the image domain range line will be very close to a sinc-function. When this line is Fourier-transformed into the Doppler domain, the magnitude of the result is a rectangular function. The width of this rectangular function depends on the spacing on the synthetic aperture.

Figure D.0.1 shows the radar as a red dot moving on the synthetic aperture where the position of the radar is limited $|x_r| < L$. The spatial Doppler frequency measured by the radar as it moves is

$$f_d = \frac{2}{\lambda}\frac{d}{dx_r}\left(\sqrt{(x_r - x_{tc})^2 + w_{tc}^2}\right) \tag{6.4.1}$$

To avoid aliasing the sample spacing on the aperture $\Delta x_r$ must meet the Nyquist criteria

$$\Delta x_r \leq \frac{1}{2f_d} = \frac{\lambda}{4(x_r - x_{tc})}\sqrt{(x_r - x_{tc})^2 + w_{tc}^2} \tag{6.4.2}$$

The shortest sample spacing requirement is when the radar is at one of the end positions ($x_r = \pm L$) and the target is located at the closest part of the target

area on the opposite side of the radar. To meet this shortest requirement, the resulting sample spacing must be smaller than needed for all other targets. And if possible, it is generally an advantage to use very short sampling distance and many measurements on the aperture. Hence, the normalised spatial Doppler frequency of a single target located in the azimuth centre will be limited, it will cover an interval less than $[-\pi, \pi]$ radians. The part of the Doppler domain function which fall outside the rectangular function (the part which has very small magnitude) must be excluded before extracting the phase error function (PEF). Since the number of samples within the rectangular function is less than the number of sample positions on the synthetic aperture, there is not a one-to-one relationship. The phase error function must be found by interpolation.

**Phase modulation of the SAR image range lines** The magnitude of the matched filter response for a point target located in the cross-range centre is shown in figure 6.2.3. It is a plot of the correlation function restated here in a simplified form

$$c_p(x, w) = \sum_{m=0}^{M-1} \sum_{n=0}^{N-1} s_{TX}(n\Delta t - \frac{2}{c} r_{RT})\, s_{TX}(n\Delta t - \frac{2}{c} r_{RP})^* \tag{6.4.3}$$

The sums are over positions on the synthetic aperture ($m$) and time ($n$). $r_{RT}$ is the distance from the radar to the point target, $r_{RP}$ is the distance from the radar to some position $(x, w)$ in the target area. As can be seen from equation 6.4.3 when $r_{RT} \approx r_{RP}$, the magnitude of the correlation product will be high. Hence, the correlation maximum in the azimuth direction is not a straight line but an arc with centre at the middle point of the synthetic aperture. Note that it is difficult to see the arc in figure 6.2.3 because the distance to the point target is much larger than the cross-range span. The constant phase lines of $c_p(x, w)$ follows the magnitude, and will also be arcs. The magnitude and phase of the range line containing the point target in the left part of figure 6.2.3 is plotted in figure 6.4.1. As can be seen the phase decreases with increasing (positive and negative) cross-range position because the distance to the radar increases.

If there are no phase errors, the range line in the Doppler domain will be a constant function for a azimuth centred point-target. When a such constant function is inverse Fourier-transformed the resulting image domain function shall ideally be a sinc-function where the phase alternates between 0 and $\pi$ at each zero in the sinc-function. As shown in figure 6.4.1 the actual FDMF SAR range line has a phase which decreases with distance from the centre. Hence, when the actual FDMF SAR range line is Fourier-transformed into Doppler domain the result is not a constant function with constant phase leading to errors in the estimation of the phase error function.

The deviation from constant phase varies with the SAR parameters. The phase of the image domain range line as a function of cross-range position can be approximated by

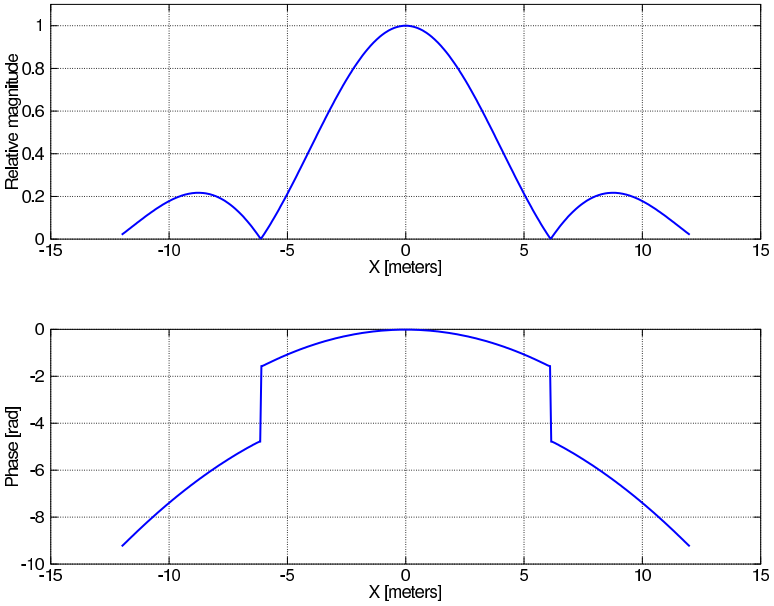


Figure 6.4.1: The phase and magnitude of a range line.

$$\phi_{rl} = 4\pi \frac{\sqrt{x^2 + w^2} - w}{\lambda} \tag{6.4.4}$$

The cross-range position of the first zero of the sinc image domain magnitude function is approximately

$$x_{1z} = w \frac{\lambda}{4L} \tag{6.4.5}$$

Inserting $x_{1z}$ for $x$ in equation 6.4.4 gives the phase change from the centre of the sinc-function to the first zero. Using values for GinSAR in the second configuration ($w = 2859$ meters, $L = 6.04$ meters and $\lambda = 51.8$ milli-meters) gives $\phi_{rl\ \mathrm{GinSAR}} = 1.59$ rad. Using values for the ERS-1 satellite ($w = 850$ kilo-meters, $L = 2400$ and $\lambda = 56.6$ milli-meters) satellite gives $\phi_{rl\ \mathrm{ERS\text{-}1}} = 3.28 \cdot 10^{-3}$ rad. We conclude that for GinSAR the phase modulation is significant and should be compensated, for a satellite SAR it may be ignored.

If the scene consists of a point target located off-centre in the azimuth direction, the image domain range line must be shifted to the centre before the Fourier-transform into Doppler domain. Otherwise the Doppler domain signal will have a phase modulation. But even after shifting, the range line in image domain will be phase modulated due to the increasing distance from the radar as a function of cross-range position. If not compensated the result will be a shift in the Doppler

domain leading to errors in the estimation of the phase error function.

**Range dependent cross-range resolution** The cross-range resolution of a spotlight SAR decreases with range. When a range line at the far end of the target area is Fourier-transformed into the Doppler domain, the resulting bandwidth will be smaller than for a range line at the close end. For autofocus algorithms that average estimated phase error functions such as phase gradient algorithm (PGA), the different bandwidth must be compensated for before summation.

**Conclusion** Frequency domain autofocus algorithms assume that the cross-range Fourier-transform of a centre located point target has constant phase and unit magnitude. This corresponds to a Dirac-function in the SAR image range line. An actual FDMF SAR image range line differs from an Dirac-function in several ways as described in the above paragraphs. As described in [99] it is possible to mostly compensate for these differences, but the extra computational load is significant. The radar parameters of GinSAR makes compensation necessary.

### 6.4.2 Single Scatterer Autofocus

When processing a SAR image using the time domain matched filtering as described in equation 6.4.3, it is possible to arrange the order of the summations such that the sum over positions on the synthetic aperture are done last. If there are only one point target in the scene and we calculate the correlation product for the position of the point target, then all terms in the last summation shall have equal phase. In this way the signal energy is maximised according to the definition of the matched filter. Any phase errors in the measured signal will introduce phase differences between the terms in the last summation. The phase error function can therefore be found directly from the phase differences between the terms.

It is possible to implement the single scatterer autofocus (SSA) algorithm in frequency domain, too. The last IFFT in cross-range is just a sum of the terms for the target point in the cross-range centre. If the cross-range position of the actual point target in image domain is shifted to the centre by multiplying with a phase modulation function in the Doppler domain, then the terms after multiplication shall have equal phase. The phase error function can then be found from the difference between these terms.

Since targets separated in range with more than the range resolution are assumed to be independent, it is sufficient with one range line that contains a single scatterer. Despite this fact, it is difficult in most SAR scenes to find range lines which contains only one single scatterer. For the received signal at one position on the synthetic aperture, each point scatterer on a range line contribute with a complex term that when added together generally changes the phase of the sum. Hence, all additional point scatterers introduces errors in the estimate of the phase error vector. For this reason the single scatterer autofocus algorithm is often considered unreliable. More information on the SSA algorithm implemented in the

frequency domain can be found in [43], section 4.4.1. There are, however, successful reports of SSA in the literature utilizing prominent scatterers occurring by opportunity in the scene [17].

### 6.4.3 Phase Gradient Autofocus

The phase gradient autofocus (PGA) algorithm [26, 101, 44, 27] has been successfully applied in a number of applications and is often used as a reference relative to other new algorithms [70]. The algorithm assumes frequency domain SAR processing such that there is a one-to-one relationship between one radar position on the synthetic aperture, and one column in the data matrix in the Doppler domain. This corresponds to tomographic formulated SAR processing without cross-range interpolation, see section 6.4.1.1. Within the associated approximations the Doppler and image domains then become Fourier-transform pairs in cross-range.

Since all range-lines are independent we may study one range-line in isolation. If there is only one point scatterer at the cross-range position $x_t$, the Doppler domain signal becomes

$$P(k_x) = a_t \exp \jmath(k_x x_t + \phi_t) \tag{6.4.6}$$

Here $a_t$ and $\phi_t$ are the magnitude and phase of the point scatterer and $k_x$ is the Doppler domain variable which is limited by $K_x$

$$|k_x| \leq K_x \approx \frac{2\omega_c}{c} \frac{L}{\sqrt{R_c^2 + L^2}} \tag{6.4.7}$$

where $\omega_c$ is the centre transmitted angular frequency, $2L$ is the length of the synthetic aperture and $R_c$ is the range to the centre of the target area, see figure C.0.1. After IFFT the image domain signal becomes

$$\rho(x) = 2K_x a_t e^{\jmath\phi_t} \operatorname{sinc} 2K_x(x - x_t) \tag{6.4.8}$$

If the measurements along the synthetic aperture includes phase errors, the Doppler domain signal becomes

$$P(k_x) = a_t \exp \jmath(k_x x_t + \phi_t + \Delta\phi_e(k_x)) \tag{6.4.9}$$

where $\Delta\phi_e(k_x)$ is the phase error function. The image domain signal then becomes

$$\rho(x) = 2K_x a_t e^{\jmath\phi_t} \operatorname{sinc} 2K_x(x - x_t) \otimes E(x - x_t) \tag{6.4.10}$$

where $\otimes$ denotes (circular) convolution and $E(x)$ is the inverse Fourier-transform of $\exp \jmath\Delta\phi_e(k_x)$. The cross-range blurring seen in SAR images with phase errors (see left part of figure 6.2.3) is caused by the convolution with $E(x)$. To estimate the phase error function the first step is to (circular) shift the image domain signal such that the peak of the sinc function is in the centre. We use $\tilde{\rho}(x)$ to denote the shifted function

$$\tilde{\rho}(x) = \rho(x + x_t) \tag{6.4.11}$$

The second step is to Fourier-transform $\tilde{\rho}(x)$ giving

$$\tilde{P}(k_x) = a_t \exp \jmath(\phi_t + \Delta\phi_e(k_x)) \tag{6.4.12}$$

Except for the constant $\phi_t$, the phase error function now can be estimated from the phase of $\tilde{P}(k_x)$.

This procedure is exactly the SSA algorithm implemented in the frequency domain. As described in section 6.4.2 all additional point scatterers introduces errors in the estimate of the phase error vector. The PGA algorithm therefore include multiplying $\tilde{\rho}(x)$ with a window function $\kappa(x)$ before the Fourier-transform into Doppler domain. The purpose is to remove all other scatterers from the image domain signal and thereby remove the errors they introduce in the phase error function estimate.

Since all point scatterers are imaged as sinc-functions that partly overlaps, the effect of the windowing operation is not perfect. Some parts of the sinc-functions from other scatterers will be inside the window, and some part of the sinc-function from the chosen scatterer will be removed. Choosing the width of the window function is a compromise. On the other hand the windowing operation makes it possible to estimate the phase error function from any range line in the image. By combining all the estimates, one optimal estimate can be found if all additional scatterers are modelled as the sum of random complex sinusoids with Rayleigh distributed magnitude and uniformly distributed phase. The linear unbiased minimum variance (LUMV) estimator [26] of the derivative of $\Delta\phi_e(k_x)$ is

$$\frac{d}{dk_x}\Delta\phi_e(k_x) = \frac{\sum_{n=0}^{N-1} \Im\left(\frac{d}{dk_x}(\tilde{P}_n(k_x))\tilde{P}_n(k_x)^*\right)}{\sum_{n=0}^{N-1} |\tilde{P}_n(k_x)|^2} \tag{6.4.13}$$

The sums are over all range lines, the actual phase error function is found by integrating equation 6.4.13. In practice the algorithm is implemented as an iteration because of the difficulty in choosing the width of the window function. The steps can be summarised with the following points

1. The strongest scatterer on each range line is circularly shifted to the cross-range centre.
2. All range lines are multiplied with a window function. The width of the window function is normally reduced for each iteration.
3. All range lines are Fourier-transformed into the Doppler domain.
4. The estimate of the phase error function is found from (integration of) equation 6.4.13.
5. The SAR data in the Doppler domain is corrected with the estimated phase error function.

6. The corrected SAR data is inverse Fourier-transformed into the image domain giving a better focused SAR image.

7. The procedure is repeated until some stop criteria.

As stated above PGA in its initial description assumes tomographic formulated SAR processing without cross-range interpolation. The associated approximations makes the resulting SAR image sub-optimal. The degrade is worst for radars with large target areas relative to the average range from the radar as is the case for GinSAR. FDMF SAR processing has the potential of being optimal, but as described in section 6.4.1.2 the assumptions made by PGA does not directly apply. It is possible to include additional processing steps into the PGA algorithm to make it applicable to FDMF [99] but the computational load is significant.

In addition the windowing operation of the PGA limits the bandwidth of the phase error function that can be estimated. The image domain function multiplied with the window function is found by inserting equation 6.4.8 into equation 6.4.11

$$\kappa(x)\tilde{\rho}(x) = \kappa(x)\left(2K_x a_t e^{\jmath\phi_t}\,\mathrm{sinc}\,2K_x x \otimes E(x)\right) \tag{6.4.14}$$

Fourier-transformation into Doppler domain gives

$$K(k_x) \otimes \tilde{P}(k_x) = K(k_x) \otimes 2K_x a_t e^{\jmath\phi_t} \exp \jmath(\phi_t + \Delta\phi_e(k_x)) \tag{6.4.15}$$

where $K(k_x)$ is the Fourier-transform of the window function $\kappa(x)$. With respect to the Doppler domain signal $\tilde{P}(k_x)$ the multiplication with $\kappa(x)$ in the image domain has the effect of filtering where the filter impulse function is $K(k_x)$. Normally the window function $\kappa(x)$ is a centred rectangular function. $K(k_x)$ is therefore a low-pass filter and the phase error function $\Delta\phi_e(k_x)$ is estimated from a low-pass filtered version of $\tilde{P}(k_x)$. The width of $\kappa(x)$ determines the low-pass cut-off frequency. Even if $\tilde{P}(k_x)$ is an angular modulated function of the phase error function, $\Delta\phi_e(k_x)$ will be band limited, too. The number of non-zero elements in $\kappa(x)$ determines the degrees-of-freedom (DOF) of the estimated $\Delta\phi_e(k_x)$ for one iteration. Repeated iterations may increase the number of DOF of the accumulated phase error function estimate. Still, based on this discussion PGA has limited ability to estimate the high frequency part of $\Delta\phi_e(k_x)$. This is mostly a concern for interferometric applications where the highest autofocus accuracy is sought.

### 6.4.4 Weighted Least Square Autofocus

Weighted Least Square Autofocus (WLSA) is an autofocus algorithm that utilizes the weighted least squares algorithm to estimate the phase error function. The description of the WLSA algorithm in this section follows the original paper closely[107]. The algorithm assumes tomographic formulated SAR processing without cross-range interpolation such that there is a one-to-one relationship between one radar position on the synthetic aperture, and one column in the data matrix in

the Doppler domain. The Doppler and image domains are then Fourier-transform pairs in cross-range, see section 6.4.1.1.

Since all range-lines are independent we may study one range-line (index $n$) in isolation. If we assume that the reflectivity function consists of a number of point scatterers, then the Doppler domain signal for range-line $n$ is the sum of all scatterer contributions (index $l$) where the phase is corrupted by the phase error function

$$P_n(k_x) = \left( \sum_l a_{tln} \exp \jmath (k_x x_{tln} + \phi_{tln}) \right) \exp \jmath \Delta\phi_e(k_x) \tag{6.4.16}$$

Here $a_{tln}$, $\phi_{tln}$ and $x_{tln}$ are the magnitude, phase and cross-range position of scatterer $l$, respectively. Equation 6.4.16 can be rewritten in the following way

$$P_n(k_x) = a_n(k_x) \exp \jmath \left( k_x x_{tn} + \phi_{tn} + \phi_{cn}(k_x) + \Delta\phi_e(k_x) \right) \tag{6.4.17}$$

where $x_{tn}$ and $\phi_{tn}$ are the cross-range position and the phase of the strongest scatterer on range-line $n$. The phase contribution from all the other minor scatterers are contained in $\phi_{cn}(k_x)$. In this formulation the magnitude $a_n(k_x)$ is a function of $k_x$.

To remove the $\exp \jmath k_x x_{tn}$ factor $P_n(k_x)$ is first Fourier-transformed into the image domain. The image function is then (circularly) shifted such that the peak of the strongest scatterer is placed in the azimuth centre. Fourier-transforming the shifted function back into the Doppler domain gives

$$\tilde{P}_n(k_x) = a_n(k_x) \exp \jmath \left( \phi_{tn} + \phi_{cn}(k_x) + \Delta\phi_e(k_x) \right) \tag{6.4.18}$$

In the following we are only interested in the phase of equation 6.4.18

$$\arg \tilde{P}_n(k_x) = \Phi_n(k_x) = \phi_{tn} + \phi_{cn}(k_x) + \Delta\phi_e(k_x) \tag{6.4.19}$$

The estimation of $\Delta\phi_e(k_x)$ proceeds by evaluating equation 6.4.16 for each $k_x$ in isolation. In this view $\Delta\phi_e(k_x)$ is a constant that can be estimated from the measured phases along the range-lines $\Phi_n(k_x)$. In order to do so the phase of the strongest scatterer must first be estimated and subtracted from equation 6.4.19

$$\tilde{\Phi}_n(k_x) = \Phi_n(k_x) - \phi_{tn} = \phi_{cn}(k_x) + \Delta\phi_e(k_x) \tag{6.4.20}$$

The procedure for estimating $\phi_{tn}$ is for a moment postponed. We will assume it has been estimated such that it can be subtracted from equation 6.4.19. The phase contributions from all minor scatterers $\phi_{cn}(k_x)$ are independent between the range-lines and can be modelled as identically independent distributed variables, in this context unwanted clutter. Then the phase error can be estimated by minimizing a least weighted squares criteria with respect to $\Delta\hat{\phi}_e(k_x)$

$$J_1(k_x) = \frac{1}{2} \sum_n \left( \frac{\tilde{\Phi}_n(k_x) - \Delta\hat{\phi}_e(k_x)}{\sigma_n} \right)^2 \tag{6.4.21}$$

where $\sigma_n^2$ are the variance of range-line $n$. The estimate becomes

$$\Delta\hat{\phi}_e(k_x) = \frac{\sum_n \frac{\tilde{\Phi}_n(k_x)}{\sigma_n^2}}{\sum_n \frac{1}{\sigma_n^2}} \tag{6.4.22}$$

Equation 6.4.22 is solved for each position on the synthetic aperture independently.

As stated above the phase of the strongest scatterer on the range-line $\phi_{tn}$ must be estimated before subtraction in equation 6.4.20. Since $\phi_{tn}$ is constant with respect to $k_x$, it is estimated by minimizing the following criteria with respect to $\hat{\phi}_{tn}$

$$J_2 = \frac{1}{2}\sum_{k_x}\left(\Phi_n(k_x) - \Delta\hat{\phi}_e(k_x) - \hat{\phi}_{tn}\right) \tag{6.4.23}$$

which finds the $\hat{\phi}_{tn}$ that is closest to the measured phase $\Phi_n(k_x)$ compensated for the phase error estimate $\Delta\hat{\phi}_e(k_x)$ in a least square sense. The catch is that $\Delta\hat{\phi}_e(k_x)$ is unknown at this stage. The problem is circumvented by an iterative procedure

1. $\Phi_n(k_x)$ is calculated from the phase of $\tilde{P}_n(k_x)$, see equation 6.4.19.
2. The range-lines are sorted in order of decreasing signal to clutter ratio (SCR) in the image domain (power of the major scatterer relative to the minor scatterers). The variances $\sigma_n^2$ are calculated from the SCRs.
3. Initially we set $\Delta\hat{\phi}_e(k_x) = 0$, $N_l = 1$.
4. $\hat{\phi}_{tn}$ is estimated from the criteria in equation 6.4.23,$n\epsilon[1,\, N_l]$.
5. $\tilde{\Phi}_n(k_x)$ is calculated from equation 6.4.20 for all $k_x$, $n\epsilon[1,\, N_l]$.
6. $\Delta\hat{\phi}_e(k_x)$ is estimated from equation 6.4.22 for all $k_x$, $n\epsilon[1,\, N_l]$.
7. $N_l = N_l + 1$, repeat from step 4 for all range-lines (until $N_l = N$).

The measured phase $\Phi_n(k_x)$ is sorted to find the most initial accurate estimate of $\phi_{tn}$.

The WLSA algorithm can easily be adapted to time-domain matched filter SAR processing. The correlation product for one target point (index $[k,\, l]$) is given by equation 6.3.1. It is rewritten here where the inner (time-samples) sum has been substituted by $U[m,\, k,\, l]$

$$c_p[k,\, l] = \sum_{m=0}^{M-1} U[m,\, k,\, l] \exp \jmath\Delta\phi_e[m] \tag{6.4.24}$$

If the target point is chosen to be the position of the major scatterer on a range-line $[k_t,\, l_t]$, the phase of the sum-terms in equation 6.4.24 can be written

$$\arg\left(U[m,\, k_t,\, l_t]\exp \jmath\Delta\phi_e[m]\right) = \phi_t[k_t,\, l_t] + \phi_c[k_t,\, l_t,\, m] + \Delta\phi_e[m] \qquad (6.4.25)$$

This is equal to equation 6.4.19 where $k_x \to m$, $n \to l_t\Delta w_t$, $x_t \to k_t\Delta x_t$.

The WLSA algorithm is robust in the sense it makes no assumption on the clutter model and can be used on most SAR images. It is capable of estimating any order of the phase error function, and it can be applied to both frequency and time-domain SAR processing. The main drawback is that all minor scatterers make some contribution to the estimation error as they are not filtered out. For SAR scenes with low SCR the accuracy will degrade.

### 6.4.5 Image Contrast Autofocus

A processed SAR image may be viewed as a 2-dimensional function of the phase error function (PEF). As shown in section 6.2 phase errors blurs and defocuses the SAR magnitude image. If the PEF is zero, the image appears to have much better contrast. Based on this observation the autofocus task can be formulated as a mathematical optimisation problem. Using an image contrast metric function to focus an image was first suggested in optics [71]. To our knowledge the first reported use of ICA for SAR appeared in [13], later followed [106].

A scalar objective function that takes the image as an argument must be defined. The objective function should ideally be constructed such that it has an extremal value when the PEF is zero. In practice some contrast or sharpness metric function is formulated. The optimisation task is then to search for the PEF which compensates the measured SAR data such that the objective function is optimised. This can be expressed by

$$\Delta\hat{\phi}_e[m] = \underset{\Delta\hat{\phi}_e[m]}{\arg\min}\, J_3\left(c_p(\Delta\hat{\phi}_e[m])\right) \qquad (6.4.26)$$

where $J_3$ is the objective function and $c_p$ is the calculated 2-dimensional SAR image function. This is a challenging task due to the high dimensionality of the PEF $\Delta\hat{\phi}_e[m]$.

The quality of an algorithm is normally judged on the amount of calculations needed, the ability to find the global extremal value (not only a local peak) and the complexity of the implementation. The choice of objective function is very important in this respect. Since the objective function acts on the SAR image, a new image must be processed for each new estimate of the PEF. Frequency domain SAR processing (tomographic formulation) has an advantage relative to time domain processing in this respect, since PEF estimate can be applied in the Doppler domain. It is only necessary to redo the cross-range IFFT to process a new SAR image with a new PEF estimate. For time domain SAR processing it is possible to optimise the processing of a new SAR image given a new PEF relative to a complete new processing. But still, the computational load and memory requirements are substantial.

There has been a number of different objective functions suggested. The most popular all operate on the image power defined

$$I[k,\, l][m] = |c_p[k,\, l](\Delta\hat{\phi}_e[m])|^2 \tag{6.4.27}$$

The functions themselves are convex for non-negative arguments. Image entropy is defined similar to entropy in information theory

$$J_{3\ \mathrm{entropy}}(c_p(\Delta\hat{\phi}_e[m])) = -\sum_k \sum_l \bar{I}[k,\, l][m] \ln \bar{I}[k,\, l][m] \tag{6.4.28}$$

The maximum power value in the image is defined

$$J_{3\ \mathrm{max\_pow}}(c_p(\Delta\hat{\phi}_e[m])) = -\max_{k,\,l} \bar{I}[k,\, l][m] \tag{6.4.29}$$

The sum of the power squared is defined

$$J_{3\ \mathrm{pow\_square}}(c_p(\Delta\hat{\phi}_e[m])) = -\sum_k \sum_l \left(\bar{I}[k,\, l][m]\right)^2 \tag{6.4.30}$$

Successful application of ICA requires that the estimated PEF which minimises the objective function, is close to the actual PEF. Investigations in this matter [29] shows that best sharpness metric function depends on the characteristics of the scene. The errors in the estimated PEF that minimises the chosen objective function, are generally smaller for scenes with many strong point scatterers. In addition a well behaved objective function has none or few local minima.

With respect to optimisation algorithms there are many suggestions, too. The most standard optimisation algorithms described in the general mathematical literature normally requires many function evaluations before convergence because of the high search space dimensionality. Specialised computer hardware may be necessary [48]. By assuming bandwidth limitations on the PEF, the computational burden can be reduced [45]. The approaches taken in the initial ICA papers [13, 106] typically adjust $\Delta\hat{\phi}_e[m]$ for one $m$ at the time where the adjustment step is reduced for each iteration [53]. In [67] it is shown that within some radius of the optimal solution, the most important contrast metric functions are well approximated by a sum of 1-dimensional functions for each element of $\Delta\hat{\phi}_e[m]$. Each element of the PEF can then be optimised in isolation which reduces the computational load substantially.

With respect to GinSAR the main drawback with ICA is the computational burden. Since the SAR processing is done in time-domain, the relative large number of SAR image reprocessing needed makes it less attractive.

### 6.4.6 Other autofocus algorithms

In addition to the autofocus algorithms described in sections 6.4.2 to 6.4.5 there are other autofocus algorithms suggested, too. Only a limited description of these are given.

#### 6.4.6.1 Map Drift Autofocus

Map Drift Autofocus Algorithm (MDAA) [63, 20] divides the synthetic aperture into two sections and estimates the second degree of the phase error function from the difference between the two images. By dividing the aperture into an increasing number of sections, higher polynomial degrees of the phase error function are estimated. The main drawback of MDAA is that estimating high orders of the phase error function becomes error prone since each section on the synthetic aperture becomes very short.

#### 6.4.6.2 Multichannel Approach to Autofocus

In the Multichannel Approach to SAR Autofocus (MAA) [68, 69, 54] the perfectly focused SAR image is formulated as a matrix - vector equation involving expressions made from the measured SAR image and the phase error function (blurring kernel). By imposing the additional constraint that the perfect focused image has regions with zero-reflectivity, the matrix - vector equation can be solved for the phase error function. The imposed constraint makes MAA different from other autofocus algorithms that typically in some way depends on point scatterers in the image. Areas with zero reflectivity are typically found close to the zeros in the radiation pattern of the antennas.

### 6.4.7 Discussion

The main GinSAR applications involve interferometric processing where the demands for accurate autofocus is the highest. The widely and successfully used PGA algorithm works inherently in the frequency domain where the tomographic approximations are taken. As detailed in section 6.4.1 it is possible to adapt PGA to time domain matched filtering, but the computational and complexity costs are significant. In addition the PGA algorithm has limited ability to estimate the high frequency part of the phase error function. These concerns have made us look for alternatives.

The papers describing the ICA algorithms shows encouraging results. Our main concerns are the accuracy of the phase error function estimate since the objective function is defined on the magnitude of the SAR image alone. The computational load may also be substantial. Still, ICA seems to be a robust algorithm capable to estimate a phase error function of any order.

By setting the weights to zero for all but one range-line, the WLSA algorithm degenerates to the SSA algorithm. Hence, the SSA algorithm may be viewed as a special case of the WLSA algorithm. We will therefore only evaluate the WLSA algorithm. It has the ability to estimate the phase error function of any order, and can easily be adapted to the time domain. The main drawback is that all minor scatterers make some contribution to the estimation error. It is possible to remedy this situation by modelling all identifiable scatterers on a range-line. In this way very accurate phase error function estimates should be possible.

Because high accuracy is important for GinSAR we have chosen to pursue the idea of modelling many scatterers of each range line. We will call this scatterer modelling autofocus.

# Chapter 7

# Scatter Modelling Autofocus with frequency domain SAR processing

The idea of estimating the phase error function by modelling many scatterers is not new. Like the original description of the WLS algorithm itself, the papers describing Scatter Modelling Autofocus Algorithms (SMAA) assume frequency domain tomographic formulated SAR processing [55, 109]. As an introduction to SMAA implemented in the time domain, we will give an introduction to the existing frequency domain algorithms.

## 7.1 Algorithm description

It is assumed that the reflectivity function consists of a number of point scatterers. The Doppler domain signal for range-line $n$ then becomes the sum of all scatterer contributions (index $l$) where the phase is corrupted by the phase error function $\Delta\phi_e(k_x)$

$$P_n(k_x) = \left( \sum_l a_{tln} \exp \jmath(k_x x_{tln} + \phi_{tln}) \right) \exp \jmath \Delta\phi_e(k_x) + \nu_n(k_x) \qquad (7.1.1)$$

Here $a_{tln}$, $\phi_{tln}$ and $x_{tln}$ are the magnitude, phase and cross-range position of scatterer $l$, respectively, and $\nu_n(k_x)$ is additive uncorrelated noise. Given the actual measurements and the model in equation 7.1.1, the task is to estimate $\Delta\phi_e(k_x)$. Since the scatterer parameters $a_{tln}$, $\phi_{tln}$ and $x_{tln}$ are unknown these must be estimated, too. In total, this is a complicated estimation task. The path taken by both [55] and [109] is to estimate $\Delta\phi_e(k_x)$ and the scatterer parameters $a_{tln}$, $\phi_{tln}$ and $x_{tln}$ alternately in an iterative procedure.

First it is assumed that we have estimates of all scatterer parameters ($\hat{a}_{tln}$,

$\hat{\phi}_{tln}$ and $\hat{x}_{tln}$) that are assumed to be correct. Then $\Delta\phi_e(k_x)$ can be estimated by minimising the following objective function (weighted least squares)

$$J_4(k_x) = \frac{1}{2}\sum_n \left| \frac{P_n(k_x) - K_n(k_x)\exp \jmath \Delta\hat{\phi}_e(k_x)}{\sigma_n} \right|^2 \tag{7.1.2}$$

where $P_n(k_x)$ is the actual measurements, $K_n(k_x) = \sum_l \hat{a}_{tln} \exp \jmath(k_x\hat{x}_{tln} + \hat{\phi}_{tln})$ and $\sigma_n^2$ is a weight factor (ideally the variance of $\nu_n$) for each range-line $n$. The estimate becomes

$$\Delta\hat{\phi}_e(k_x) = \angle \exp \jmath \Delta\hat{\phi}_e(k_x) = \angle \frac{\sum_n \frac{P_n(k_x)K_n(k_x)^*}{\sigma_n^2}}{\sum_n \frac{K_n(k_x)K_n(k_x)^*}{\sigma_n^2}} \tag{7.1.3}$$

In the second step it is assumed that we have a correct estimate of the phase error vector $\Delta\hat{\phi}_e(k_x)$. The task is to estimate all scatterer parameters ($\hat{a}_{tln}$, $\hat{\phi}_{tln}$ and $\hat{x}_{tln}$). This is a complicated multidimensional optimisation problem and therefore more difficult than the estimation of $\Delta\hat{\phi}_e(k_x)$. We may formulate the estimation task as to find the scatterer parameters that minimises this objective function

$$J_{5n} = \frac{1}{2}\sum_{k_x} \left| P_n(k_x) - \left( \sum_l \hat{a}_{tln} \exp \jmath(k_x\hat{x}_{tln} + \hat{\phi}_{tln}) \right) \exp \jmath \Delta\hat{\phi}_e(k_x) \right|^2 \tag{7.1.4}$$

The approach taken is to use the *relax* algorithm [52]. By inspection of equation 7.1.1 we see that the estimation of the scatterer parameters resembles estimation of sinusoids in additive noise. This is exactly the estimation problem targeted by the *relax* algorithm. The *relax* algorithm may be viewed as an improvement to the *clean* algorithm [41] which has its origin in radio astronomy. In [34] an improved *clean* algorithm is formulated for general spectral estimation. The estimation accuracy is improved by correcting previously estimated spectral parameters for each new spectral component added into the estimation. The *relax* algorithm takes the iteration even further. The iteration procedure is repeated for each new component until the estimation objective function 7.1.4 converges. By using convergence as an iteration stop criteria, the *relax* algorithm can itself determine the number of sinusoids in the signal.

Here follows a summary of a scatterer modelling autofocus algorithm in the frequency domain

1. Select the range-lines to be include in the estimation.
   Some range-lines are better removed all together from the estimation. These are characterised by (i) no clear point scatterers, the reflectivity function appears to be diffuse, and (ii) a high number of scatterers where no one really dominate. With respect to (i) these range-lines do not meet the assumption of discrete point scatterers. Practically they can be identified by having low energy. With respect to (ii) it is demanding to include these range-lines because a high number of scatterers must be included in the estimation.

Finding the range-lines to exclude is challenging. If the focus of the initial SAR image is poor then all range-lines look diffuse. The thresholds applied to accept range-lines must be set based on image characteristics. If there are a few range-lines containing only one strong scatterer and otherwise little clutter, then all other range-lines may be excluded. And if all range-lines are very equal then maybe no one should be excluded.

2. Sort the chosen range-lines such that the line assumed to be best suited for autofocus comes first.

3. Initially the phase error estimate is set to zero, $\Delta\hat{\phi}_e(k_x) = 0$.

4. The range-line index is set to the first range-line, $n = 1$.

5. The scatterer parameters of range-line $n$ are estimated using the *relax* algorithm.

   (a) Initially we will start by estimating one scatterer, $L = 1$.

   (b) Initialise the index to the scatterer we will estimate, $i = 1$.

   (c) Subtract (*clean*) the effect of all previously estimated scatterer parameters except the one we shall estimate from the measured range-line

   $$P_{ni}(k_x) = P_n(k_x) - \left( \sum_{l=1,\, l\neq i}^{L} \hat{a}_{tln} \exp \jmath(k_x \hat{x}_{tln} + \hat{\phi}_{tln}) \right) \exp \jmath \Delta\hat{\phi}_e(k_x)$$

   (d) Estimate the cross-range position of the scatterer

   $$\hat{x}_{tin} = \arg\max_{\hat{x}_{tin}} \left| \sum_{k_x} P_{ni}(k_x) \exp -\jmath k_x \hat{x}_{tin} \exp -\jmath \Delta\hat{\phi}_e(k_x) \right|^2$$

   It is found at the maximum value of the Fourier-transform of $P_{ni}(k_x) \exp -\jmath\Delta\hat{\phi}_e(k_x)$ squared. Since the Fourier-transform of this Doppler domain signal is the *clean*ed image-domain signal, $\hat{x}_{tin}$ may be found at the *clean*ed image-domain signal maximum magnitude point.

   (e) Estimate the magnitude of the scatterer

   $$\hat{a}_{tin} = \left| \frac{1}{N_{k_x}} \sum_{k_x} P_{ni}(k_x) \exp -\jmath k_x \hat{x}_{tin} \exp -\jmath \Delta\hat{\phi}_e(k_x) \right|$$

   It is found as the magnitude of the Fourier-transform of $P_{ni}(k_x) \exp -\jmath\Delta\hat{\phi}_e(k_x)$ evaluated at $\hat{x}_{tin}$. Similar to $\hat{x}_{tin}$, this is equal to the magnitude of the *clean*ed image-domain signal maximum point.

(f) Estimate the phase of the scatterer

$$\hat{\phi}_{tin} = \arg\left(\sum_{k_x} P_{ni}(k_x) \exp -\jmath k_x \hat{x}_{tin} \exp -\jmath \Delta\hat{\phi}_e(k_x)\right)$$

It is found as the phase of the Fourier-transform of $P_{ni}(k_x) \exp -\jmath\Delta\hat{\phi}_e(k_x)$ evaluated at $\hat{x}_{tin}$. Similar to $\hat{x}_{tin}$, this is equal to the phase of the *clean*ed image-domain signal maximum point.

(g) If $i < L$ then increment $i$ and continue from step 1f.

(h) If $L > 1$ and if the scatterer estimates have not converged, set $i = 1$ and continue from 1f

(i) If the reduction in the objective function 7.1.4 is larger than some threshold, increment $L$ and $i$, and continue from step 1f.

6. Estimate the phase error function $\Delta\hat{\phi}_e(k_x)$ by equation 7.1.3.

7. Increment the range-line index $n$ and continue from step 5. If computational time is of little concern we may re-estimate the scatterer parameters in all range-lines up to $n$, that is continue from step 4. Re-estimation is appropriate when $n = 2$, it may be considered when $n$ is small, but will contribute little as $n$ increases.

## 7.2 Discussion

The algorithm described in section 7.1 uses the Fourier-transform relationship between image domain and the Doppler-domain. The essential point for the algorithm is that the data is made available in a domain where each data point has a one-to-one relationship with one position on the synthetic aperture. We will call this the aperture-domain as the name Doppler-domain is not appropriate for SAR processing in time-domain. The algorithm described in section 7.1 can be divided into the *relax* estimation of scatterers and the phase error function estimation. In the following we will analyse these parts to identify the essential steps taken.

**The *relax* estimation** The *relax* part of SMAA works on range-lines in isolation. To simplify we assume a range-line with only two scatterers. The algorithm consists of the following points.

1. The initial SAR processed image-line vector is available both in image- and in aperture-domain. In frequency-domain SAR processing the last step is a Fourier-transform from aperture-domain (Doppler-domain) to image-domain. Time-domain SAR processing can also be arranged such that the processing that combines data measured at different positions on the synthetic aperture is done last.

2. Estimate the cross-range position of the dominating scatterer by finding the maximum value in the image-domain. The magnitude and phase of the maximum image-point is taken as estimates of the scatterer magnitude and phase.

3. Clean the found major scatterer from the signal. In the algorithm given in section 7.1 the *clean* subtraction is done in aperture-domain (Doppler-domain), see algorithm step 5c.

4. Transform the *clean*ed signal into image-domain and find the second major scatterer by finding the maximum value. The magnitude and phase is found from the maximum pixel.

5. Back in aperture-domain now only the second (minor scatterer) is subtracted from the initial signal.

6. Transform this *clean*ed signal into image-domain and re-estimate the major scatterer.

7. Continue from point 3 until the two sets of scatterer parameters have converged.

In essence, the estimation of the scatterer-parameters (position, magnitude and phase) is done in the image-domain, and the *clean*ing subtraction is done in the aperture-domain. The procedure described in section 7.1 only includes transformation from aperture-domain into image-domain (inverse Fourier-transform). Transformation in the other direction is not needed because the Fourier-transform of one found scatterer is calculated analytically as a single harmonic function, see the expression within the brackets of point 5c in the algorithm. Since we have assumed that the image scene consists of a number of discrete point scatterers, the Fourier-transform of a single shifted point (impulse) is a harmonic function.

It is important to notice that the *clean*ing subtraction does not need to be done in the aperture-domain. After the *clean* subtraction the difference is transformed into image-domain. Since this transformation is a linear operation (inverse Fourier-transform for SAR processing in frequency-domain, matrix multiplication for SAR processing in time-domain), the order of subtraction and transformation may be switched. Subtracting the image-domain impulse response from the image-domain signal will give the same result. Hence, the *relax* estimation may be computed in the image-domain alone if we can calculate the impulse response in the image-domain. We will take advantage of this fact in formulating a practical SMAA in time-domain.

We will add one comment on the impulse response when the SAR processing is done in frequency-domain. In practice the sample spacing in image-domain is often increased by zero-padding in the Doppler-domain before the last inverse Fourier-transform. In this case the Fourier-transform of a single point scatterer, the harmonic function, is also zero for those Doppler frequencies that were zero-padded. When inverse Fourier-transformed back into the image-domain the result will not be a single impulse but a sampled sinc-function.

**The phase error function estimation** The phase error function estimate is found by equation 7.1.3 which minimises the least square weighted sum given in equation 7.1.2. These two equations are naturally formulated in the aperture-domain since the phase error function is an aperture-domain function. Hence, the aperture-domain representations of the found point scatterers are needed.

To enlighten the principle for scatterer modelling autofocus, we will assume that there is only one range-line and on this range-line there is only one scatterer. The sums in equations 7.1.3 and 7.1.2 will then consist of a single term and the $K(k_x)$ sum will consist of only a single harmonic function $K(k_x) = \hat{a}_t \exp \jmath(k_x \hat{x}_t + \hat{\phi}_t)$. The phase error function estimate then simply becomes the phase difference between $P(k_x)$ and $K(k_x)$. In general, the scatterer modelling autofocus phase error estimate for one position of the aperture is the phase difference between the measured signal and the signal we should have received given the estimated scatterer.

# Chapter 8

# Scatter Modelling Autofocus with time domain SAR processing

We have decided to use time-domain SAR processing in GinSAR. It the most accurate and flexible SAR processing method, and the computational load is considered to be acceptable. With respect to autofocus, the arguments given in section 6.4.1 indicates that higher accuracy in the estimation of the phase error function should be possible operating in the time-domain. In this section we will therefore present a scatterer modelling autofocus algorithm (SMAA) based on SAR processing in time domain. The development of SMAA is one of the main achievements in this thesis.

## 8.1 Aperture-domain

SAR processing in time-domain is described in section 3.2. It is implemented as a matched filter two-dimensional correlation product for each target point as shown in equation 3.2.4 and 3.2.5. In a simplified form the correlation product is given by

$$c_p[k,\, l] = \sum_{m=0}^{M-1} \sum_{n=0}^{N-1} \tilde{s}[n,\, m]\, \hat{s}[n,\, m] \tag{8.1.1}$$

Here $k$ and $l$ are indexes into the target point grid, that is, they define the image point position $(x_t,\ w_t)$, and $m$ and $n$ are indexing the position on the synthetic aperture and time sample, respectively. $\hat{s}$ is the measured signal, and $\tilde{s}$ is the complex conjugate of the signal we would expect if there is a scatterer in the image point position. Hence, $\tilde{s}$ is a function of the image point position. By studying one range-line in isolation (ignoring the $l$-index) and introducing

$$A_p[m][k] = \sum_{n=0}^{N-1} \tilde{s}[n,\, m]\, \hat{s}[n,\, m] \tag{8.1.2}$$

as the sum over the $N$ time samples, the correlation product can be written

$$c_p[k] = \sum_{m=0}^{M-1} A_p[m][k] \tag{8.1.3}$$

The $A_p$ function in equation 8.1.2 contains the signal in aperture-domain, data recorded at different positions on the synthetic aperture are not combined. We have deliberately included the $k$-argument in the $A_p$-function to underline it is a function of the image point position. This fact shows a difference relative to the Doppler-domain for SAR processing conducted in the frequency domain. There is not one single aperture-domain function that can be transformed into image-domain, there are separate functions for each image-domain position. To find the image-point the associated aperture-domain function must simply be summed. Consequently, it is not possible to transform an image-domain range-line into a set of aperture-domain functions.

With respect to the *relax* estimation of scatterers on a given range-line, the *clean* subtraction must therefore be done in the image-domain. Hence, it must be practically possible to calculate the impulse-response in the image-domain. With respect to the phase error function estimation, it is necessary to calculate an aperture function from the signal we would have received given the estimated scatterers, and another aperture function from the real measured signal. These two aperture functions must be calculated using the same image-domain position argument. It is not necessary to calculate aperture-domain functions for all image-domain positions. Conceptually, which image-domain position argument that is used is arbitrary.

## 8.2 Polar grid of image positions

A rectangular grid of image points is normally used in SAR processing. Besides providing uniform point density, the choice is dictated by the FFT algorithm when the SAR processing is done in the frequency domain. When the SAR processing is done in the time domain, the positions for the image points can be arbitrarily chosen since each point is calculated in isolation. For scatterer modelling autofocus using time-domain SAR processing, there are two reasons for using a polar grid of image positions instead of a rectangular grid.

**Independent range-lines** In the algorithm described in section 8.3 it is assumed that each range-line is independent. Along the centre-line normal to the synthetic aperture the distance between the first zeros in the point response can be approximated by $\Delta R_c = c/B_w$ where $B_w$ is the bandwidth of the signal (two times the range resolution). The left side of figure 8.2.1 shows a simplified view of

the SAR response for two scatterers.

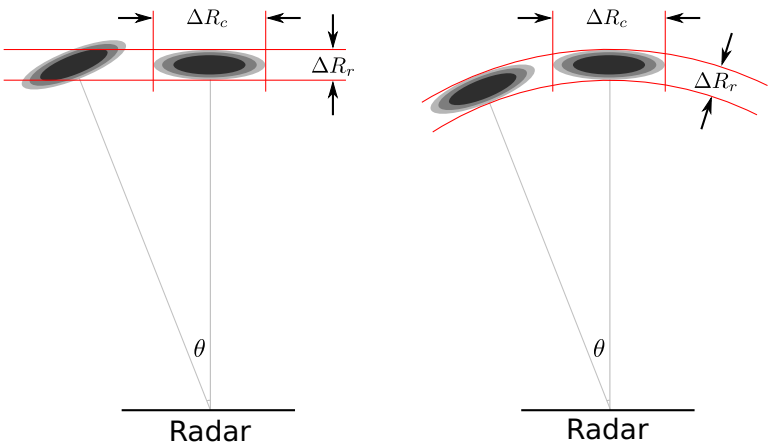


Figure 8.2.1: Independent range-line distance for rectangular and polar grid.

The first scatterer is located on the centre line normal to the synthetic aperture, the other at a squint angle $\theta$. In this image the cross-range resolution given by $\Delta R_c = \lambda/2L$, is larger than the range resolution $\Delta R_r$.

Because $\Delta R_c > \Delta R_r$ the distance between the first zeros in range is larger than $\Delta R_r$ for the squinted target. If a polar grid of image point is used instead as shown in the figure on the right, the distance between the first zeros are kept at $\Delta R_r$.

**Impulse response calculation** As explained in section 8.1 it is necessary to do the *clean* subtraction in the image-domain. It must therefore be practically possible to calculate the impulse-response in the image-domain. If a rectangular grid of image points is used, the impulse-response along the range-line is a complicated function difficult to approximate with analytical functions. If, however, a polar grid of image points is used, it is possible to approximate the impulse-response along the range-arc with fair accuracy. The angular impulse response assuming a plane wave-front is given by [100]

$$h(\theta,\, \theta_t) = \frac{\sin(k\Delta x_r N_a(\sin\theta_t - \sin\theta))}{\sin(k\Delta x_r(\sin\theta_t - \sin\theta))} \tag{8.2.1}$$

where $\theta_t$ is the squint angle of the target, $N_a$ is the number of measurement positions on the synthetic aperture and $\Delta x_r$ is the distance between the measurement positions. To reduce the computational time we have first defined a prototype function

$$h_p(\upsilon) = \frac{\sin(k\Delta x_r N_a \upsilon)}{\sin(k\Delta x_r \upsilon)} \tag{8.2.2}$$

which is calculated and stored for a wide range and densely separated values of the argument $v$. To calculate $h(\theta, \theta_t)$ for a particular scatterer located at the angel $\theta_t$, $h_p(v)$ is interpolated at $v = \sin\theta_t - \sin\theta$. The computational load for the (linear) interpolation is low.

There are two approximations introducing small errors in this approach, interpolation and the plane wave front. The error contribution from the interpolation can be reduced to an insignificant level by increasing the density of the prototype function argument $v$. The error contribution from assuming a plane wave-front is a function of the distance from the radar to the scatterer and the length of the synthetic aperture. Using typical numbers for GinSAR gives a peak relative error less than 0.01.

**Conclusion** Based on this discussion we have used a polar distributed grid of image points. It is required for being able to calculate the arc-range impulse response necessary for the SMAA. We have also chosen to use an equal angular distribution of image points on each range-arc. The image point density along the arc will then be higher at the near end of the target area compared to the far end. Normally the target area range span is small relative to the range from the radar to the centre of the target area. Hence, the difference in point density is acceptable.

## 8.3 One dimensional scatterer estimation algorithm

This section describes the first algorithm we have implemented and used to process simulated data. As all other algorithms described so far, it assumes that the distance between the range arcs exceeds the range resolution, and each range arc may therefore be regarded as independent. Thus, the estimation of scatterer positions becomes a one dimensional estimation task along the arc. Compared to the algorithm described in section 7.1 the algorithm described here is not only a conversion imposed by the SAR processing being done in the time-domain. There are also other modifications we have found practical and needed for better performance.

### 8.3.1 The algorithm steps

1. The scatterer parameters for all range-arcs are first calculated. They are computed for each range-arc in isolation.

   (a) Initialise the index to the scatterer we shall estimate, $i = 1$, and initialise the correlation product $c_{pi}[k]$ to the initial processed range-arc, $c_{pi}[k] = c_p[k]$.

   (b) Initialise the threshold function to all zeros. The threshold function defines a magnitude limit the new scatterer candidate found as described in step 1c must exceed to be accepted as a proper scatterer.

The purpose and calculation of the threshold function is explained in section 8.3.2.3.

(c) Estimate the scatterer $\hat{s}_{ti}$.

i. Estimate the arc-angel $\hat{\theta}_{ti}$ of $\hat{s}_{ti}$. It is found by first finding the $k$-index along the arc which maximises $|c_{pi}[k]|$. Then $\hat{\theta}_{ti}$ is found at the maximum value of a second degree polynomial defined by $|c_{pi}[k-1]|$, $|c_{pi}[k]|$ and $|c_{pi}[k+1]|$. Hence, $\hat{\theta}_{ti}$ is not restricted to the arc-grid points.

ii. Estimate the magnitude $\hat{a}_{ti}$ of $\hat{s}_{ti}$. The same second degree polynomial defined in step 1(c)i is used. If $\hat{a}_{ti}$ does not exceed the threshold function, the scatterer $\hat{s}_{ti}$ candidate is rejected and the algorithm is terminated.

iii. Estimate the complex phase of $\hat{s}_{ti}$. It is found as a linear interpolation of the complex phase between the two $c_{pi}$ points closest to $\hat{\theta}_{ti}$ on the arc-grid.

(d) Increment $i$.

(e) Calculate a threshold-function using the magnitude and position of all previously estimated scatterers.

(f) Subtract the effect of all previously estimated scatterer parameters from the original processed SAR arc (the *clean*-algorithm subtraction) $c_{pi}[k] = c_p[k] - \left(\sum_{j=1}^{i-1} h[k](\hat{s}_{tj})\right)$. Here $h[k](\hat{s}_{tj})$ is the impulse-response for the scatterer $\hat{s}_{tj}$.

(g) Estimate a new scatterer $\hat{s}_{ti}$ using the procedure in step 1c.

(h) Adjust the scatterer parameters (arc-angle, magnitude and complex phase) for all found scatterers so far by the *relax* algorithm. The steps are repeated until convergence.

i. Set $v = 1$, the index to the estimated scatterer we will adjust.

ii. Subtract (*clean*) the effect of all scatterers except scatterer $v$ from the measured range-line $c_{pi}[k] = c_p[k] - \left(\sum_{j=1,\, j\neq v}^{i-1} h[k](\hat{s}_{tj})\right)$.

iii. Calculate a threshold-function using the position and magnitude of all scatterers from index 1 up to $v$.

iv. Re-estimate scatterer $v$ using the procedure in step 1c.

v. Increment $v$, continue from step 1(h)ii as long as $v \leq i$.

(i) Continue from step 1d.

2. Using the estimated scatterer parameters each range-arc is evaluated with respect to usability for scatterer modelling autofocus. The score $\sigma_r^2$ is calculated by the following expression

$$\sigma_r^2 = \frac{|\sum_k \left(c_p[k] - \left(\sum_{j=1}^{i} h[k](\hat{s}_{tj})\right)\right)|}{|\sum_k c_p[k]|} \tag{8.3.1}$$

A score equal to zero means the summed impulse responses matches the initial signal perfect. A high score indicates a poor match between the summed impulse responses and the initial signal.

3. To calculate the estimate of the phase error function we must first calculate a synthesised aperture domain signal $A_{ps}$ using the estimated scatterers. As explained in section 8.1 it is arbitrary which point on the arc-grid (which $k$) that is used when calculating the aperture domain signal. We will therefore use the centre point and suppress the $k$-index. But we will include the $l$-index identifying the arc-range. The synthesised aperture domain signal is therefore written as a function of position on the synthetic aperture (index $m$) and range-arc (index $l$), $A_{ps}[m][l]$.

   (a) A raw radar signal data-set $\hat{s}_s[n,\, m]$ is synthesised from a scene containing the estimated scatterers. For each scatterer a delayed and scaled version of the transmitted signal is defined where the delay is the two-way propagation time from the radar to the scatterer position, and the scaling is proportional to the scatterer magnitude. All the defined signals are summed together. A complete synthesised data-set is made by repeating the procedure for all positions on the synthetic aperture.

   (b) $A_{ps}[m][l]$ is now calculated using equation 8.1.2 where $\hat{s}[n,\, m]$ is replaced by $\hat{s}_s[n,\, m]$.

4. The measured aperture domain signal $A_p[m][l]$ is calculated from equation 8.1.2 (using the measurement data $\hat{s}[n,\, m]$).

5. The phase error function $\Delta\hat{\phi}_e[m]$ is estimated by

$$\Delta\hat{\phi}_e[m] = \angle \frac{\sum_l \frac{A_p[m][l]A_{ps}[m][l]^*}{\sigma_{rl}^2}}{\sum_l \frac{A_{ps}[m][l]A_{ps}[m][l]^*}{\sigma_{rl}^2}} \tag{8.3.2}$$

   The score $\sigma_{rl}^2$ is used as a measure of the variance of range-arc $l$.

6. The estimated phase error function $\Delta\hat{\phi}_e[m]$ is used in a new SAR processing run which gives a better focused SAR image.

The sequence of using this autofocus algorithm and then processing a new image using the estimated phase error function can be repeated until $\Delta\hat{\phi}_e[m]$ has converged to a small magnitude.

### 8.3.2 Algorithm evaluation

The final phase error function estimate shown in equation 8.3.2 is a weighted average over the estimate for each range-arc. Hence, the final estimation error depends on the estimation accuracy for each range-arc. We will therefore study a single range-arc in isolation.

If there is only one range-arc the phase error function estimate becomes

$$\Delta\hat{\phi}_e[m] = \angle A_p[m]\, A_{ps}[m]^* \tag{8.3.3}$$

The range-arc index $l$ has been suppressed for clarity. While the $A_p[m]$ function is calculated from the measured data, $A_{ps}[m]$ is calculated from the scatterers we have estimated on the associated range-arc of the SAR image. The estimation accuracy therefore depends on how well we manage to identify and estimate the scatterers. There are three ways the estimation procedure may fail or introduce errors

1. It may fail to identify one or more existing scatterers.
2. It may identify and estimate one or several non-existing scatterer.
3. It may identify and estimate an actual existing scatterer, but the scatterer parameters might be very inaccurate.

The procedure for identifying and estimating scatterers as described earlier in this section finds the first scatterer at the maximum of the SAR image function. To find the second scatterer the impulse response of the first scatterer is subtracted. The second scatterer will then be estimated at the maximum of the difference function.

#### 8.3.2.1 Zero phase error

To show the principles of the procedure we have conducted some simulations where the phase error function is zero. The range to the arc has been set to 2803 meters, the angular separation between the calculated points in the SAR image function is 0.74 milli-rad, corresponding to 2.08 meters on the arc. The SAR image-function is shown as a blue line, the magnitude of the summed impulse response for all identified scatterers is shown as a green line. The magnitude of the difference between the SAR image-function and the summed impulse response is shown as a red line.

**Simulation 1** In this scene there is only one scatterer at the azimuth angle 2.23 milli-rad. The magnitude of the functions are shown in figure 8.3.1.

The estimation algorithm has identified a scatterer at the maximum of the SAR image function shown by the small cyan circle. The phase of the functions are shown in figure 8.3.2.

This simulation shows that the calculation of the impulse response described in equation 8.2.1 is very close to the real impulse response (the blue and green functions are almost identical). The magnitude of the difference (the red line, figure 8.3.1) is thus very close to zero.

**Simulation 2** In this scene there are two scatterers located at the azimuth angles -2.23 and +2.23 milli-rad. The RCS of the scatterer at azimuth-angle -2.23 milli-rad is 0.04 relative to the other scatterer which gives a magnitude ratio of 0.2.

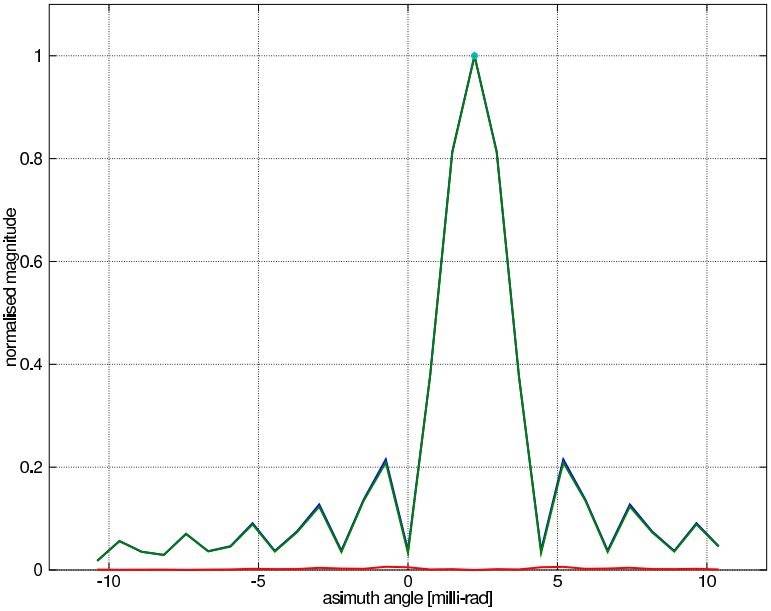


Figure 8.3.1: Magnitude of single scatterer

The magnitude of the functions after the first major scatterer has been estimated are shown in figure 8.3.3.

As can be seen, the second minor scatterer can easily be estimated after the subtraction (the red curve). Without the subtraction it is difficult to discriminate the minor scatterer from the side-lobes of the strongest scatterer. Figure 8.3.4 shows the functions after both scatterers have been estimated by the algorithm.

Both scatterers are estimated almost perfectly, the difference between the combined impulse responses and the SAR image function (the red curve) is small.

Both the SAR image function and the impulse responses are complex functions. In the simulations so far both scatterers have been at exactly equal range. If the range-difference between the two scatterers is set to $\lambda/8$ (corresponding to $\pi/4$ difference in angle) the functions after both scatterers have been estimated is shown in figure 8.3.5.

The scatterers have been estimated in almost exactly the same positions even if the SAR image function and the summed impulse response differ.

#### 8.3.2.2 Non-zero phase error

The following simulations includes a non-zero phase error function. The phase error function is a second-degree polynomial where the root-mean-square (RMS) phase error is $\pi/4$ radians.

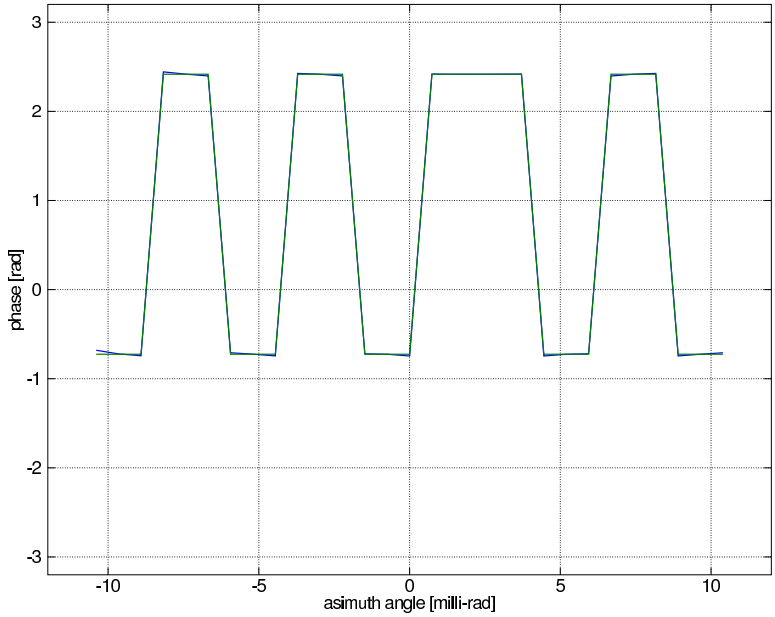


Figure 8.3.2: Phase of single scatterer

**Simulation 3** This scene has two scatterers located at the azimuth angles -5.0 and +2.0 milli-rad. The magnitude of the scatterer at azimuth-angle -5.0 milli-rad is 0.3 relative to the other scatterer. The range difference between the two scatterers is $\lambda/8$.

Figure 8.3.6 shows the magnitude curves after the first scatterer has been estimated.

Because of the phase error function the difference remaining after the *clean* subtraction is substantial. When continuing the search for the second scatterer, the peaks at the azimuth angles -3.0, 0.0 and 4.5 milli-rad are all stronger than the peak at -5.0 milli-rad. If no actions are taken we would wrongly estimate scatterers at some of the positions close to the strongest scatterer. This example shows the shortcomings of the *clean* operation when there is a phase error. It becomes very difficult to distinguish between the remainder after the *clean* operation and an actual weaker scatterer.

**Simulation 4** If we have a weak scatterer located further away from the strong scatterer the situation is better. This is shown in figure 8.3.7 which is equal to simulation 3 except that the two scatterers are located at the azimuth angels -6.0 and +7.0 milli-rad.

The peak in the position of the second minor scatterer at -6.7 milli-rad is

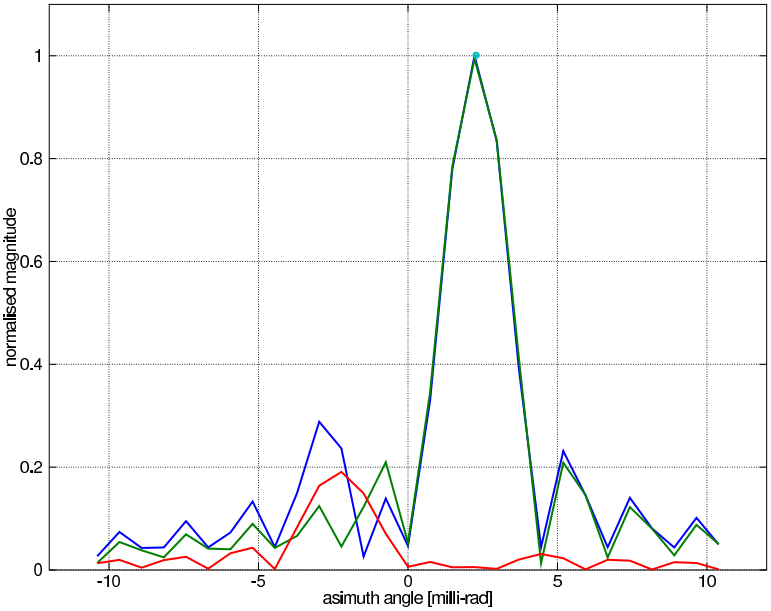


Figure 8.3.3: Scene with two scatterers after estimation of the first.

smaller than the peaks at the azimuth angles +4.5 and +9.6 milli-rad. But it is the highest peak within a close vicinity.

#### 8.3.2.3 Threshold-function

To be able to estimate the real existing scatterers in situations as described in simulation 4 we will introduce a threshold-function with the following purpose

1. It shall as far as possible prevent the remainder after the *clean*-algorithm subtraction to be falsely estimated as scatterers.

2. It shall contribute to correct estimation of weak scatterers located some distance away from a strong scatterer.

As the name implies, the function serves as a threshold the peaks of the difference-function must exceed before being identified as a scatterer. Only peaks on the difference-function that is larger than the threshold-function will be identified and estimated. The function is constructed as the sum of bell-shaped functions. For each estimated scatterer a new bell-shaped function is added where the bell centre is shifted to the azimuth position of the estimated scatterer. Figure 8.3.8 shows the same simulation as in figure 8.3.7 but with the threshold-function added in pink after the strongest scatterer has been estimated.

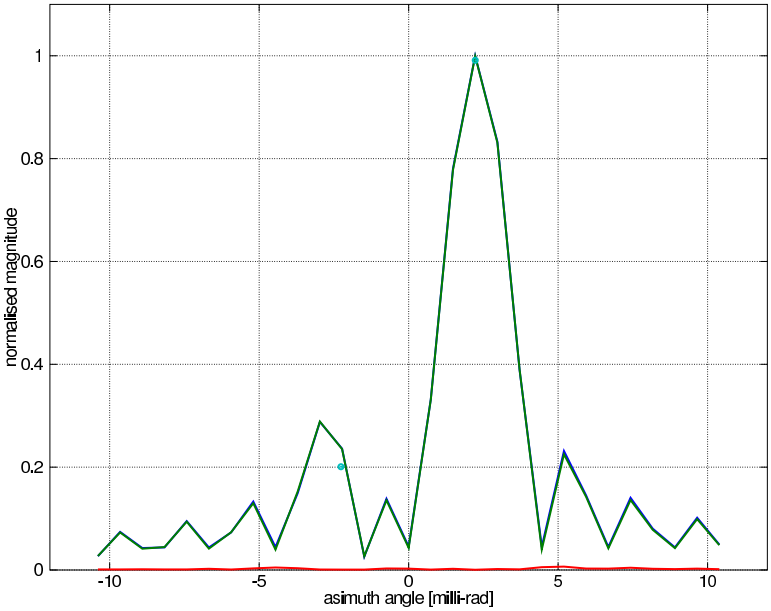


Figure 8.3.4: Scene with two scatterers at the end of the estimation procedure.

With this threshold-function the estimation algorithm will correctly estimate the weak scatterer at the azimuth position -6.4 milli-rad and not the stronger peaks closer to the first strong scatterer.

The shape of the prototype bell-function can be adjusted in three ways. The peak of the bell can be set to the magnitude of the estimated scatterer as in figure 8.3.9 or lower, the width of the bell-shoulders and on the floor level far away from the bell can also be adjusted. The shape used in figure 8.3.9 will enforce the estimation of the scatterer at the azimuth-position -6.7 milli-rad and prevent the peaks at +4.5 and +9.6 milli-rad to be estimated. Figure 8.3.9 shows the situation after the estimation of this second scatterer.

In this case the threshold function helped the estimation procedure to correctly estimate the two real existing scatterers and to avoid any of the peaks emerging from the incomplete subtraction of the impulse responses. Also notice that after estimation of the second scatterer there are no peaks left exceeding the threshold-function. In our implementation we use this as a criteria for ending the estimation of more scatterers.

Successful application of a threshold-function depends strongly on the shape of the bell-function. If we use a function with magnitude equal to the scatterer and wide shoulders (as done in the previous example), we effectively suppress peaks emerging from incomplete subtraction of the impulse responses. But at

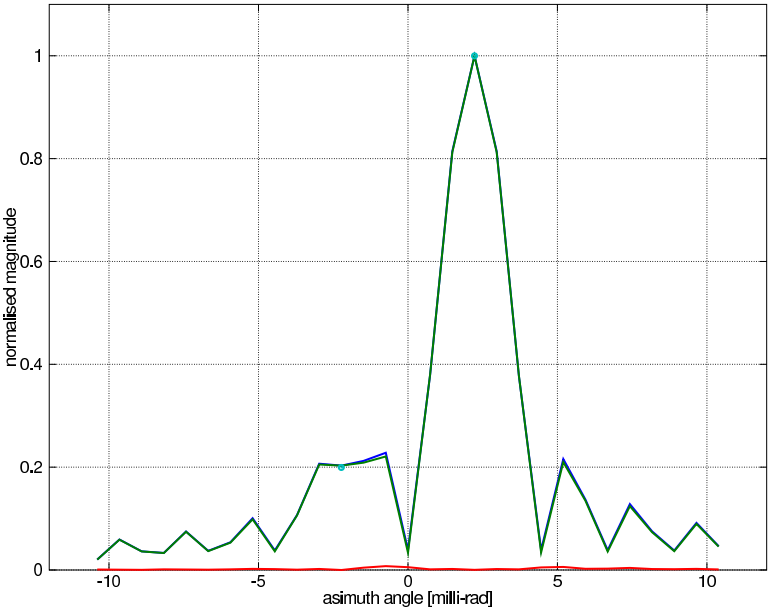


Figure 8.3.5: Estimation of two scatterers with phase difference.

the same time any real existing scatterers close to an other strong scatterer will be suppressed. If we try to use the same shape of the bell-function as used in simulation 4 in the more difficult case used in simulation 3 we have the situation shown in figure 8.3.10 after the estimation of the strongest scatterer.

As can be seen, we will fail to estimate the second scatterer because the threshold-function is too wide. If we use a too low and narrow threshold-function such as shown in figure 8.3.11 we will wrongly identify a scatterer at -0.8 milli-rad azimuth-angle.

Choosing the magnitude, width and the floor level of the bell-functions used in the construction of the threshold-function is a challenging task. If the SAR image appears to be very blurred or we have other reasons to believe the phase error function has large average magnitude, it is better to use bell-functions that have a magnitude equal to the magnitude of the estimated scatterer and wide shoulders. With this approach we will avoid false identification of scatterers close to strong scatterers. At the same time we may fail to identify real existing scatterers. The end result will be an estimate of the phase error function with significant errors, but normally the remaining phase error function has lower average magnitude then the initial. When the SAR image is re-processed using the estimated phase error function there will be less remainder after the subtraction of the impulse responses. In the second iteration usage of a bell-function with smaller magnitude and more

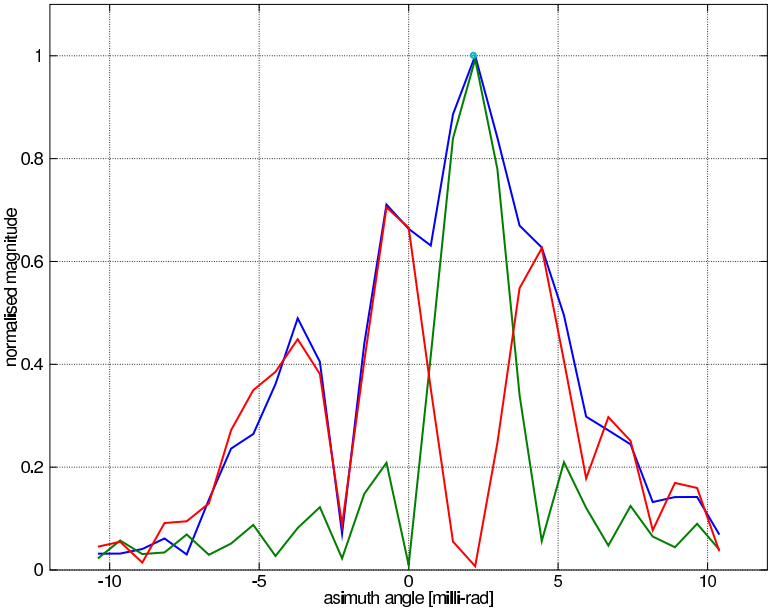


Figure 8.3.6: Two close scatterers with quadratic phase error.

| Scatter no. | Rel. mag. | Azimuth angle [milli-rad] | Range offset from arc [milli-meter] |
|---|---|---|---|
| 1 | 1.0 | +3.0 | +6.8 |
| 2 | 0.3 | -5.0 | +52.3 |
| 3 | 0.3 | -9.0 | +115.0 |

Table 8.3.1: Simulation 5 scatterers parameters

narrow shoulders is appropriate.

#### 8.3.2.4 Iterated estimation

By iterating the procedure described at the end of last section, an accurate estimation of the real existing scatterers without many false identifications is possible. The error in the estimate of the phase error function will then gradually become smaller.

**Simulation 5** To show the progress while iterating we have made a simulation where there are 3 scatterers with relative magnitude, position and phase as shown in table 8.3.1. The phase error is the same quadratic function as used in the previous simulations.

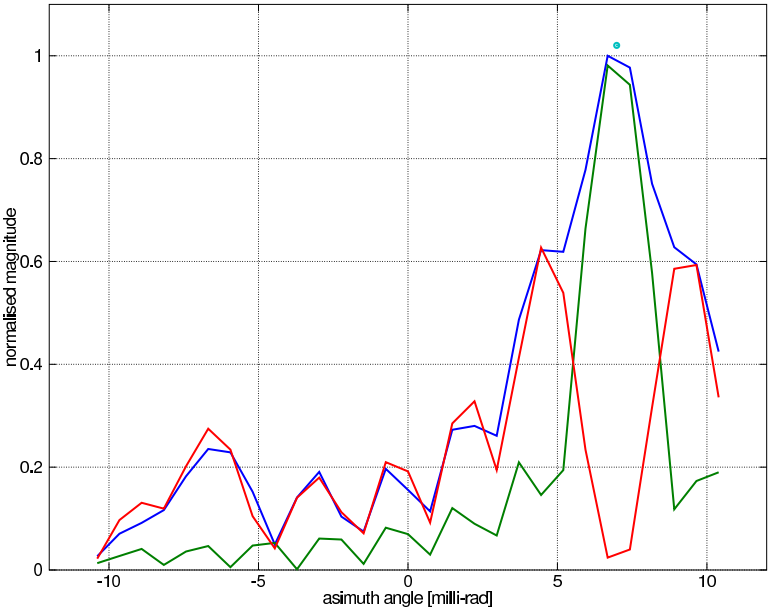


Figure 8.3.7: Two scatterers far apart with quadratic phase error.

Figure 8.3.12 shows the situation after the first run of the algorithm.

The azimuth position of the estimated scatterers (the cyan circles) are almost correct. The magnitude of scatterer number 2 is too high. The residual after the subtraction of the combined impulse responses (the red curve) is substantial. The graph also shows that successful identification of the three scatterers is very depending on the chosen shape of the bell-curves used to construct the threshold-function. Since the initial image-arc (the blue curve) is very blurred, the simulation setup represents a difficult case. The estimated phase error function constructed from the estimated scatterers, has been used to correct a second SAR processing. When the estimation algorithm is ran a second time with the better focused image-arc as input, we get the result shown in figure 8.3.13.

In this case it is much easier to visually identify the three scatterers. The combined impulse responses (the green curve) is almost identical to the image-arc giving only small a remaining-function. Also notice that the scatterer magnitudes are more correct, and that the bell-curves used to construct the threshold-function have a magnitude less than the magnitude of the associated scatterer. Figure 8.3.14 shows the initial phase error function (blue) and the estimated phase error function after the first (green) and second (red) run of the algorithm. Repeated iterations would have improved the estimate even more.

All these simulations are limited to one arc. By combining all arcs in the SAR

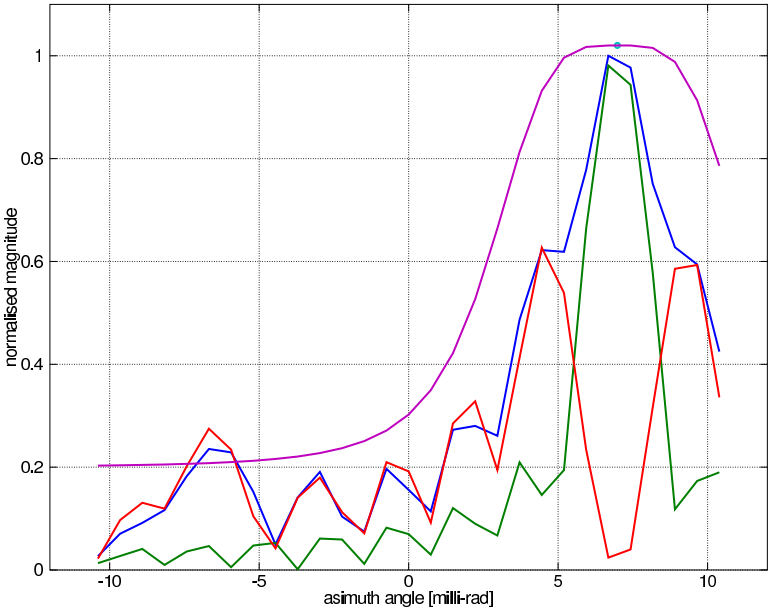


Figure 8.3.8: Threshold function after estimation of the strongest scatterer.

image one single estimate is found as described by step 5 in the algorithm. This combined phase error function estimate will generally be more accurate than each separate range-arc estimates. In particular, the effect of errors in the identification and estimation of some scatterers on some arcs will be reduced.

Even if single arc simulations using this algorithm show good results, it is possible to construct scenes where the assumption of independent range-arcs is at best only partly justified. In these cases the end results may be estimates of the phase error function with substantial errors. We have therefore investigated modifications of the algorithm which do not assume that the range-arcs are independent.

## 8.4 Two dimensional scatterer estimation algorithm

### 8.4.1 Problem description

Figure 8.4.1 shows a polar SAR magnitude image of a simulated scene containing two scatterers in the range and azimuth-angle positions 2806.5 meters, 1.4253 milli-rad and 2804.0 meters, -1.4253 milli-rad, respectively. The range difference between the processed range-arcs is one meter and the colour-bar values are in dB. The positions of the identified scatterers are indicated with white circles.

The threshold-function concept has prevented estimation of more than one

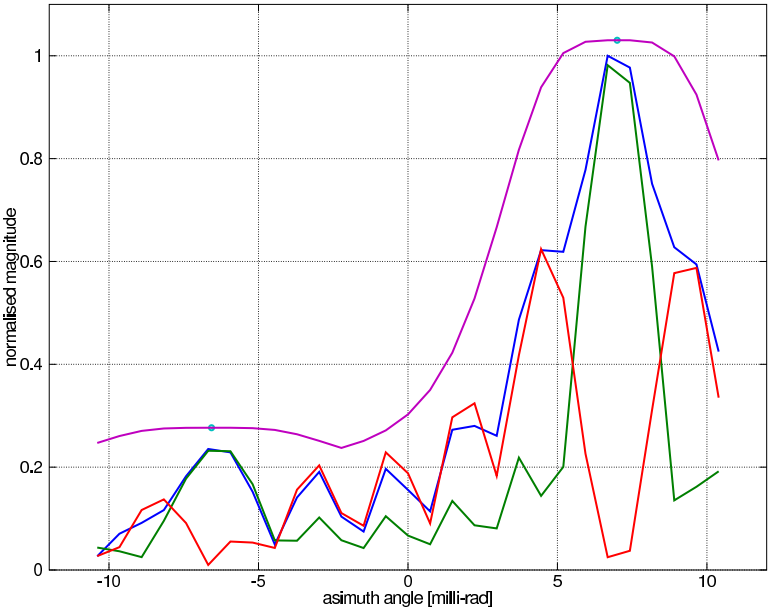


Figure 8.3.9: Threshold function after estimation of both scatterers.

scatterer on any range-arc. But since the algorithm work on range-arcs in isolation, at least one scatterer will be estimated on each range-arc. In figure 8.4.1 a total of 41 scatterers have been identified even if there is only two actual scatterers in the scene. This result is not optimal since the radar signal that will be synthesised given all these estimated scatterers, step 3 in the algorithm, will to some extent differ from the actual measured signal. In most situations the difference is clearly noticeable but still moderate. Most of the identified scatterers will be estimated to have weak magnitude.

The ideal would be if only scatterers on those range-arcs that are closest to the actual scatterers were estimated. The root of the problem is that the range-arcs are not completely independent, there are side-lobes in the range-dimension. If there is a weak scatterer located close to a range-arc, the range-side-lobe of a strong scatterer on a neighbourhood range-arc can easily be stronger than the response of the weak scatterer. A possible remedial action would be to use a window-function in the range dimension during the SAR processing, it may be combined with an increase in the range distance between the range-arcs. In this way the range-arcs will be more independent, but this solution has some shortcomings. A scatterer located at a range in the middle between two range-arcs will be estimated as two scatterers, one in each range-arc. If the scatterer is relatively weak, and the distance between the range-arcs is more than the range resolution, the scatterer may

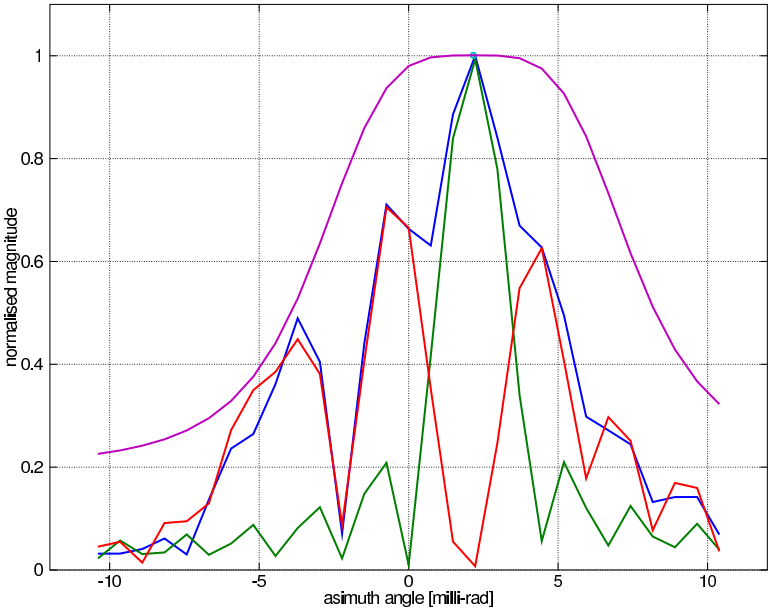


Figure 8.3.10: Two close scatterers with a wide threshold-function.

fail to be estimated at all. It is difficult to make the range-arcs truly independent and at the same time identify all scatterers and correctly estimate their position and magnitude. A part of the problem is that the algorithm will estimate the range position of a scatterer to always be the range of the processed range-arc only offset by a fraction of a wavelength to make the phase match the measured signal.

Having identified these drawbacks of one-dimensional scatterer estimation, we have therefore developed and implemented a two dimensional scatterer estimation algorithm.

### 8.4.2 The algorithm steps

Even if the main improvement is the usage of a two-dimensional algorithm for estimating the scattering positions, we have also introduced a step where the estimated phase-error functions calculated from some range-arcs are removed because they are evaluated to have large errors (step 4).

1. The scatterer parameters for all scatterers in the SAR image are calculated. This is done by the following two-dimensional sub-algorithm:

   (a) Initialise the index to the scatterer we shall estimate, $i = 1$, and initialise the correlation product $c_{pi}[k, l]$ to the original complex SAR image

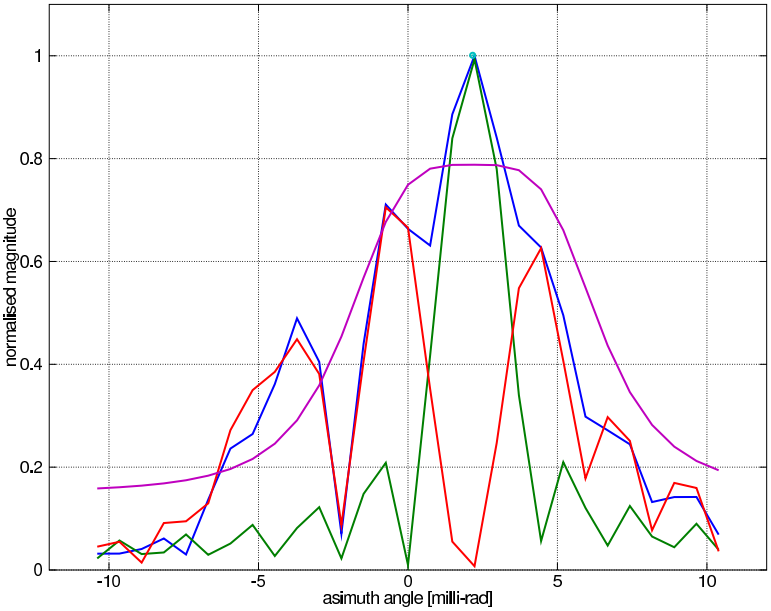


Figure 8.3.11: Two close scatterers with a narrow threshold-function.

, $c_{pi}[k,\, l] = c_p[k,\, l]$.

(b) Initialise the two-dimensional threshold function to all zeros. The purpose of the two-dimensional threshold function is equal to the one-dimensional as described in section 8.3.2.3. The calculation of the function is detailed in section 8.4.2.2.

(c) Estimate the scatterer $\hat{s}_{ti}$ (the arc-angle $\hat{\theta}_{ti}$, and range $\hat{R}_{ti}$ and the magnitude $\hat{a}_{ti}$). The estimation procedure is detailed in section 8.4.2.3.

(d) Increment $i$.

(e) Calculate a two-dimensional threshold-function using the magnitude and position of all previously estimated scatterers.

(f) Subtract the impulse responses of all previously estimated scatterer parameters from the measured image (the *clean*-algorithm subtraction)

$$c_{pi}[k,\, l] = c_p[k,\, l] - \left( \sum_{j=1}^{i-1} h[k,\, l](\hat{s}_{tj}) \right) \tag{8.4.1}$$

Here $h[k,\, l](\hat{s}_{tj})$ is the two-dimensional impulse-response for the scatterer $\hat{s}_{tj}$. The calculation of $h[k,\, l](\hat{s}_{tj})$ is detailed in section 8.4.2.4.

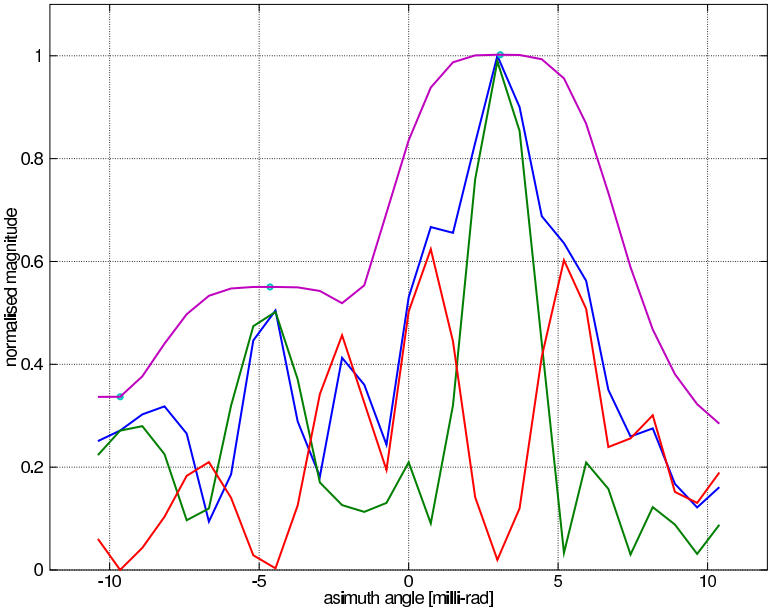


Figure 8.3.12: First run of scene with three scatterers.

(g) Estimate a new scatterer $\hat{s}_{ti}$ using the procedure in section 8.4.2.3. If the magnitude of the new scatterer is less than some defined limit relative to the strongest estimated scatterer, the estimation of new scatterers is aborted. The limit is defined relative to the overall maximum magnitude pixel. Continue from step 2.

(h) Adjust the scatterer parameters (arc-angle $\hat{\theta}_{tv}$, magnitude $\hat{a}_{tv}$ and range $\hat{R}_{tv}$) for all found scatterers so far by the *relax*-algorithm. The steps are repeated until convergence.

i. Set $v = 1$, the index to the estimated scatterer we will adjust.

ii. Subtract the effect of all scatterers except scatterer $v$ from the original complex SAR image $c_{pi}[k,\, l] = c_p[k,\, l] - \left(\sum_{j=1,\, j\neq v}^{i-1} h[k,\, l](\hat{s}_{tj})\right)$.

iii. Calculate a threshold-function using the position and magnitude of all scatterers from index 1 up to $v$.

iv. Re-estimate scatterer $\hat{s}_{tv}$ using the procedure in step 1c.

v. Increment $v$, continue from step 1(h)ii as long as $v \leq i$.

(i) Continue from step 1d.

2. Calculate a synthesised aperture domain signal $A_{ps}$ using all the estimated

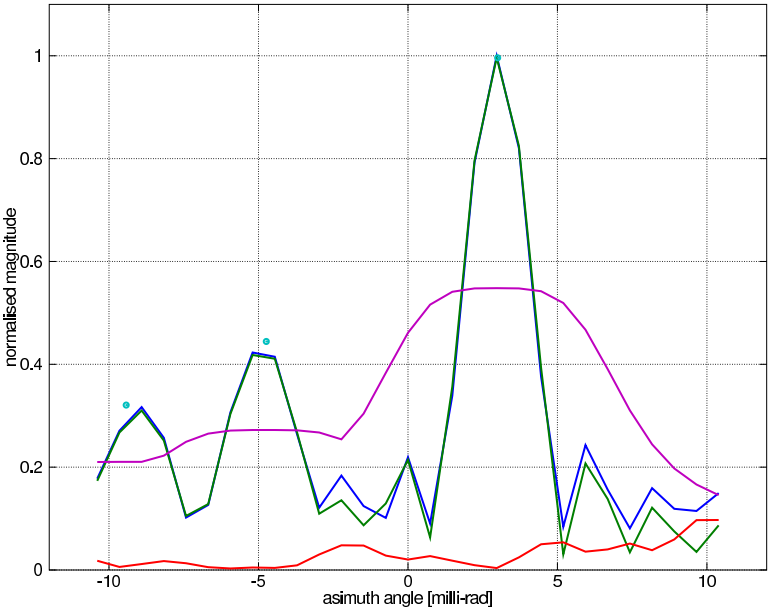


Figure 8.3.13: Second run of scene with three scatterers.

scatterers. As in the one-dimensional case we use the centre point on the arc-grid when calculating the aperture domain signals. The synthesised aperture domain signals are a function of the synthetic aperture position and therefore written as $A_{ps}[m][l]$ ($m$ is the index to the aperture position).

(a) A raw radar signal data-set $\hat{s}_s[n,\, m]$ is synthesised from a scene containing the estimated scatterers. For each scatterer a delayed and scaled version of the transmitted signal is defined where the delay is the two-way propagation time from the radar to the scattering position, and the scaling is proportional to the scattering magnitude. All the defined signals are summed together. A complete synthesised data-set is made by repeating the procedure for all positions on the synthetic aperture.

(b) $A_{ps}[m][l]$ is now calculated using equation 8.1.2 where $\hat{s}[n,\, m]$ is replaced by $\hat{s}_s[n,\, m]$.

3. A phase error estimate is calculated for each range-arc (index $l$) by

$$\Delta\hat{\phi}_e[m][l] = \angle A_p[m][l]\, A_{ps}[m][l]^* \tag{8.4.2}$$

In this respect it is still assumed that the range-arcs are independent.

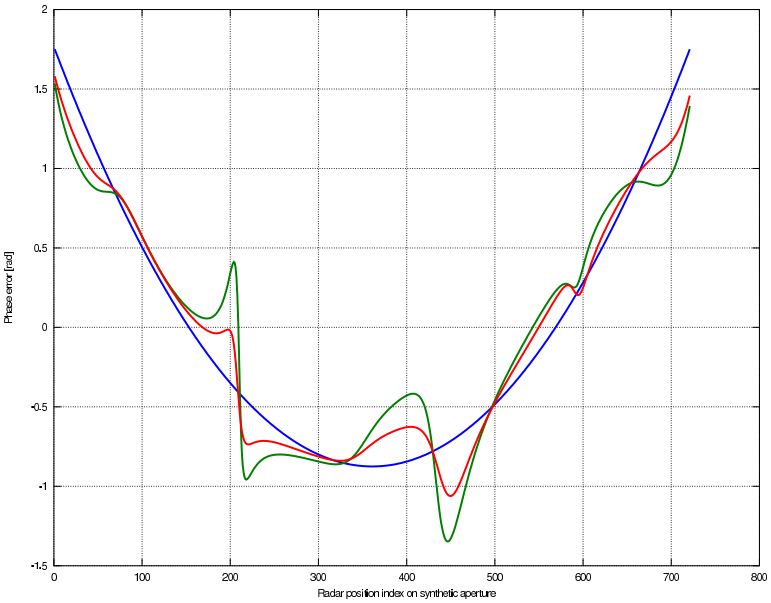


Figure 8.3.14: Phase error functions.

4. Remove the phase error function estimates which are evaluated to have large errors compared to the rest. In step 3 a phase error function is calculated for each range-arc. Ideally all these functions should be equal. In practice many are very equal but usually some differ substantially from the rest. In this step these last functions are identified as outliers that will only degrade the final single phase error function estimate, and therefore removed. The removal procedure is detailed in section 8.4.2.5

5. Calculate a single final phase error function estimate as a weighted average. The weights are proportional to the magnitude of the aperture function.

$$\Delta\hat{\phi}_e[m] = \frac{\sum_l |A_p[m][l]|\, \Delta\hat{\phi}_e[m][l]}{\sum_l |A_p[m][l]|} \tag{8.4.3}$$

   In equation 8.4.3 the sums do not include the phase error functions that were removed in step 4.

6. The estimated phase error function $\Delta\hat{\phi}_e[m]$ is used in a new SAR processing run which gives a better focused SAR image.

The sequence of using this autofocus algorithm and then processing a new image using the estimated phase error function can be repeated until $\Delta\hat{\phi}_e[m]$ has converged to a small magnitude.

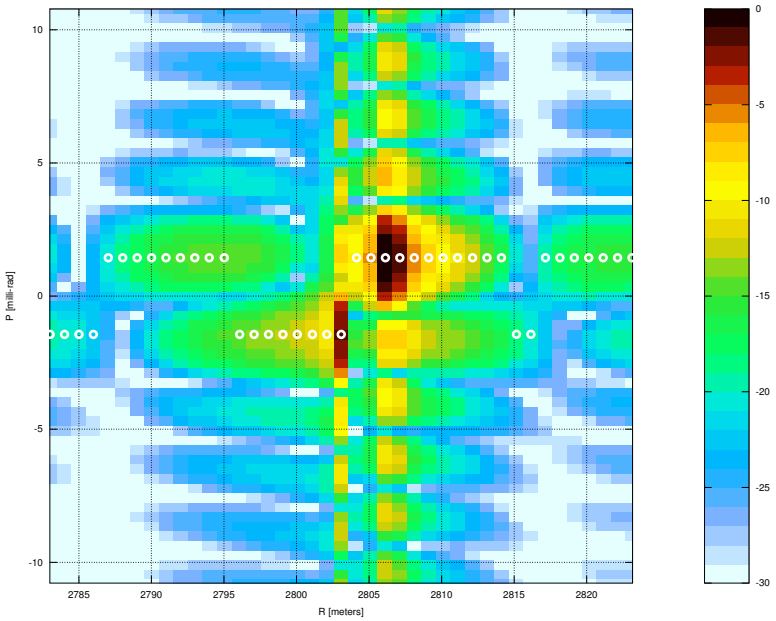


Figure 8.4.1: Estimated scatterers with one dimensional SMAA.

#### 8.4.2.1 Replacing clean-algorithm subtraction with scatterer removal

In situations where the phase error function magnitude is substantial, the clean-algorithm subtraction is very incomplete. The difference between a defocused point scatterer and the subtracted impulse response may have a large magnitude. The clean-algorithm subtraction may even wrongly produce peaks in the SAR image function which exceeds the threshold function and therefore are subsequently estimated. Experimentation has shown that in this situation it is a better approach to replace the *clean/relax*-algorithm, step 1f-1h. Instead the correlation product $c_{pi}[k, l]$ is multiplied with a scalar magnitude function that has zero value in the estimated scatterer position and unity value further away. In this way the major scatterers are estimated with fair accuracy while it must be accepted that closely located weaker scatterers are not identified. The idea is to achieve an initial reduction of the phase error function magnitude. Reprocessing the SAR image using the resulting phase error function estimate should produce a SAR image where the *clean*-algorithm subtraction is more complete, the difference between a defocused point scatterer and the impulse response has a smaller magnitude.

#### 8.4.2.2 Two-dimensional threshold function

The two-dimensional threshold function is constructed by the sum of prototype functions. These bell-shaped prototype-functions are shifted and scaled to the positions and magnitudes of the estimated scatterers. The prototype two-dimensional bell-shaped function is constructed by multiplying the one-dimensional threshold-function exactly as described in section 8.3.2.3 with an other bell-shaped function in range. The shape of this range function has been designed to cover the impulse-response with a small margin. It is not adjustable because the defocusing effect of phase-errors are mainly in the cross-range dimension, see section 6.2.

#### 8.4.2.3 Two-dimensional scatterer estimation

1. Find the maximum point of the magnitude of the SAR image function that exceeds the threshold function

$$|c_{pi}[k_m,\, l_m]| = \max |c_{pi}[k,\, l]| \tag{8.4.4}$$

   If no points of $|c_{pi}[k,\, l]|$exceeds the threshold function the estimation procedure is terminated.

2. Define a two-dimensional convex parabolic-function from the maximum point and its neighbourhood points in range and azimuth ($|c_{pi}[k_m,\, l_m]|$, $|c_{pi}[k_m + 1,\, l_m]|$, $|c_{pi}[k_m - 1,\, l_m]|$, $|c_{pi}[k_m,\, l_m + 1]|$, $|c_{pi}[k_m,\, l_m - 1]|$).

3. Use the maximum of the parabolic-function as the magnitude of the scatterer $\hat{a}_{ti}$ estimate. Use the position of the maximum as the scatterer position estimate (arc-angle $\hat{\theta}_{ti}$, and range $\hat{R}_{ti}$). In this way the estimated position is not restricted to the polar grid-points.

4. Adjust the estimated range $\hat{R}_{ti}$ by a fraction of a half wave length such that the complex phase of $\hat{s}_{ti}$ matches the phase of $c_{pi}$. This is done by a weighted average the phase of the maximum point $c_{pi}[k_m,\, l_m]$ and its neighbourhood points. The weights are set by their relative magnitudes. The phase of $c_{pi}[k_m,\, l_m + 1]$, $c_{pi}[k_m,\, l_m - 1]$ are first adjusted for the range offset.

For the SAR image function to be accurately interpolated by a convex parabolic-function the sample distance must be less than the resolution in both range and azimuth. Using a parabolic function for interpolation is justified since the polynomial expansion of the azimuth and range impulse responses both are even functions with a dominating second degree term, see section 8.4.2.4.

Since the adjustment of $\hat{R}_{ti}$ done in step 4 is only a fraction of a half wave length and the wave length is approximately 1/20 of the range resolution, the adjustment is insignificant with respect to the magnitude response.

#### 8.4.2.4 Two-dimensional impulse response

Section 8.2 explains how it is possible to approximate the azimuth component of the impulse-response with fair accuracy if a plane wave-front approximation is

used, see equation 8.2.1. Similar to the threshold function the two-dimensional impulse response will be constructed by multiplying the azimuth impulse-response expression with a range impulse-response expression.

We will approximate the frequency spectrum magnitude of the transmitted chirp-signal to be a rectangular function. The error introduced by this approximation is small. See [39] section 2.1.2.2.2. for an analytical derivation of the frequency spectrum and the rectangular approximation. The magnitude impulse response in range $R$ then becomes a sinc-function

$$h(R,\, R_t) = \frac{\sin\left(\frac{2\pi B w(R-R_t)}{c}\right)}{\left(\frac{2\pi B_w(R-R_t)}{c}\right)} \tag{8.4.5}$$

The magnitude of the two dimensional impulse response is given by the product of equation 8.2.1 and 8.4.5. The impulse response phase is set to a linear function of range where the phase at $R_t$ is set to zero. The complete two-dimensional impulse response then becomes

$$\begin{aligned} h(\theta,\, \theta_t,\, R,\, R_t) \quad = \quad & \frac{\sin(k\Delta x_r N_a(\sin\theta_t - \sin\theta))}{\sin(k\Delta x_r(\sin\theta_t - \sin\theta))} \times \\ & \frac{\sin\left(\frac{2\pi B_w(R-R_t)}{c}\right)}{\left(\frac{2\pi B_w(R-R_t)}{c}\right)} e^{-\jmath\frac{4\pi}{\lambda}(R-R_t)} \end{aligned} \tag{8.4.6}$$

In the derivation of equation we have approximated the wave front to be plane and the magnitude of the frequency spectrum to be a rectangular function. In a typical scene simulations show that peak relative error of this expression is less than 0.01.

#### 8.4.2.5 Removal of phase error function estimates with large errors

A new and assumed independent phase error function is calculated for each range-arc in step 3 in the algorithm. Ideally all these functions should be equal. In practice many are very conform but usually some differ substantially from the rest because there are some significant errors in the estimation of scatterers close to the associated range-arcs. Typically some scatterer has failed to be identified and estimated because it is positioned close to an other strong scatterer.

Figure 8.4.2 shows a simulated example where all 18 estimated phase error functions are plotted. Most of these curves resembles the actual simulated second degree phase error function, but some curves have strong deviations at many positions on the synthetic aperture.

Combining all these curves into one estimate by calculating the average is not optimal. The curves with large errors in some positions will in those positions pull the mean away from the correct estimate. This is because the sample phase distribution is characterised by outliers, samples that do not fit into a normal distribution model.

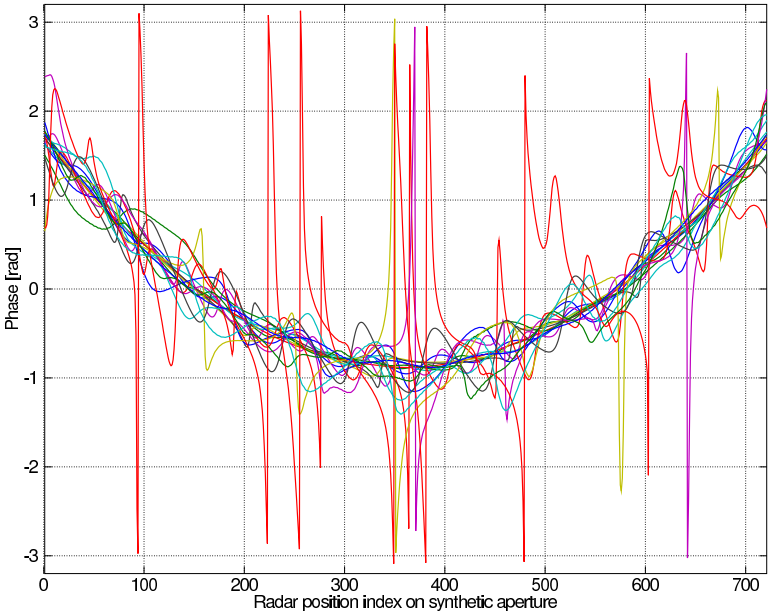


Figure 8.4.2: Estimated phase error functions.

Robust statistics provide methods that can substitute normal statistical estimators, but which are very insensitive to outlier data-points. In particular, the median is used as a robust estimator of central tendency. For a general introduction to robust statistics, see [42].

A different but related approach is to remove the estimated functions that are "very different from the rest" and use only the remaining functions to calculate one optimal estimate. This resembles removing outlier data-points in statistical distributions except that in this case the data-points are functions. The identification of outliers is a subjective task without any accepted mathematical definition of what constitutes an outlier. For more information on outliers in statistics, see [9].

In this work we have chosen to identify a set of phase error function estimates that are close in the sense they resemble each other. Those which are not in the close-set of functions are classified as outliers and removed. The function closeness is calculated as the euclidean distance. The rational behind this approach is as follows. If there are range-arcs where all actual nearby scatterers have been estimated correctly, the associated phase error function estimates will be almost equal to each other and very close to the actual function. Hence, a set of functions that are very equal is a strong indicator that these functions have small errors. Functions that are very different from all other functions usually have substantial

| Estimator | RMS error [milli-rad] |
|---|---|
| Mean | 75 |
| Median | 35 |
| Weighted mean of close-set | 23 |

Table 8.4.1: Root-mean-square errors of the different estimates.

errors. Using this approach we may end up removing more functions than would be done using traditional outlier identification criteria. Since the remaining functions are assumed to be closer to the true phase error function, the accuracy of the final estimate should be better.

This are the steps taken for identifying the functions in the close-set:

1. The euclidean distance between all possible pairs of functions is calculated.
2. The number of functions to include in the close set is initialised, $n_s = 2$.
3. The $n_s$ number of functions that have the minimum average distance between them are identified, and the average distance is recorded, $d(n_s)$.
4. $n_s$ is incremented and the algorithm is repeated from step 2 for all range-arcs in the data set.
5. The number of functions to include in the close-set must be determined. At the same time as we seek a set of functions that are very close to each other, we also want the number of functions in the set to be as large as possible. This trade-off situation can be solved by optimising some defined objective function. But in practice it is challenging to define an objective function which performs well in all situations. In this work we have therefore found it easier to determine the size of the close-set by manual inspection.
6. The functions that have the minimum average inter-distance for the optimal $n_s$, are defined to be in the close-set. The other functions are classified as outliers and not used in further processing.

A weighted average of the functions in the close-set is used as the single final estimate of the phase error function. This is described in step 5 in the main algorithm (section 8.4.2). Figure 8.4.3 shows the 6 phase error function estimates that are in the close set from the simulation in figure 8.4.2.

Figure 8.4.4 shows the actual true simulated phase error function (blue line), the mean of the estimated phase error functions (green line), the median (red line) and the estimate found using our algorithm (cyan line).

The root-mean-square (RMS) error of the different estimates are given in table 8.4.1. Both the figure and the table indicate that the weighted mean of a close-set of functions has smaller error than both the mean and median of all functions. It also shows that the median is clearly better than the mean.

Notice that in the calculations of the euclidean distance, the mean and the median needs be adapted to angular data which are defined on a circular domain.

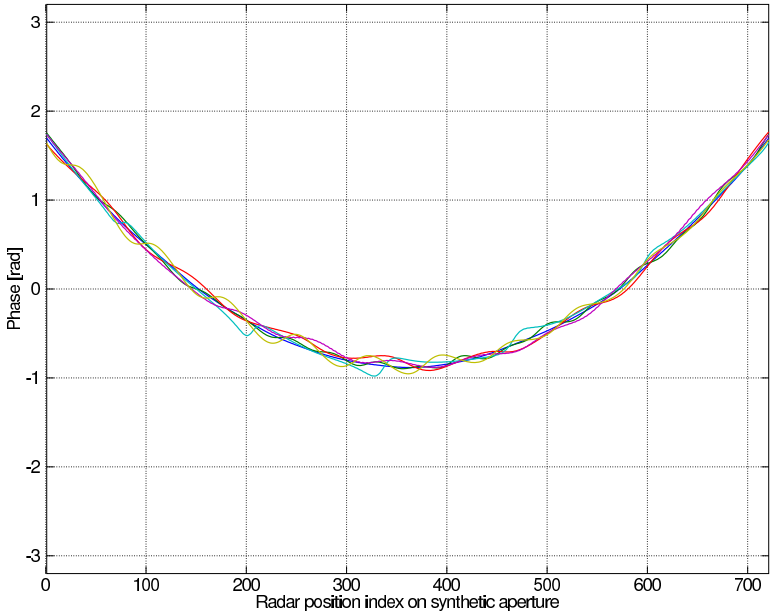


Figure 8.4.3: Estimated phase error functions in the close-set.

| Scatter number | X-position [m] | W-position [m] | RCS [m$^2$] |
|---|---|---|---|
| 1 | 585.1 | 2826.3 | 700 |
| 2 | 598.7 | 2796.3 | 560 |
| 3 | 554.7 | 2777.9 | 560 |
| 4 | 520.3 | 2856.0 | 560 |

Table 8.4.2: Position and magnitude of the 4 strongest scatterers

Central in circular data statistics is the fact that the distance between two data samples cannot be more than $\pi$-radians.

### 8.4.3 Simulation example

To demonstrate the algorithm we have conducted a realistic simulation.

#### 8.4.3.1 Simulation description

The target scene consists of totally 361 scatterers. The 4 strongest scatterers have the positions and radar cross-section (RCS) magnitudes as shown in table 8.4.2.

All of the remaining 357 scatterers have random RCS, exponentially distributed with mean 84 m$^2$ and random position within the target area. The strongest of

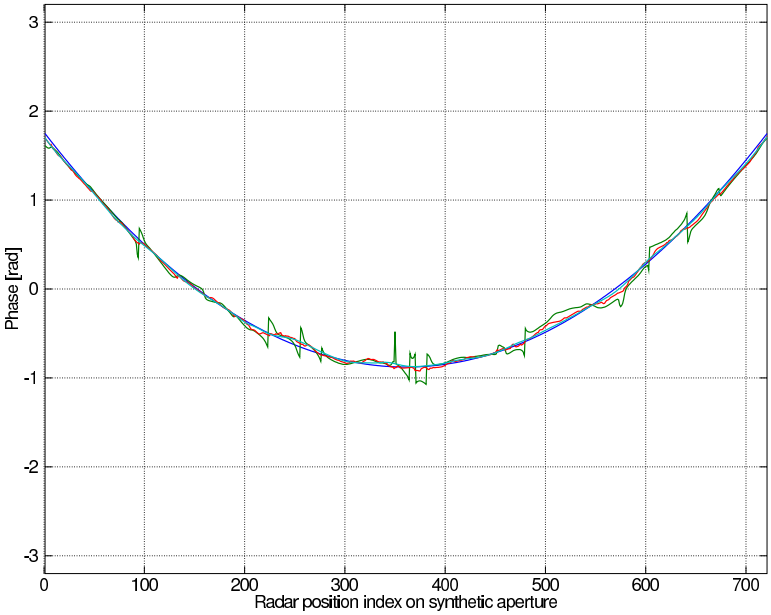


Figure 8.4.4: True simulated and estimated phase error functions.

these scatterers have a RCS of 385 $m^2$. The SAR image of the scene processed with zero simulated phase error function is shown in figures 8.4.5 and 8.4.6. In all these figures the colour-bar values are in dB. In figure 8.4.6 Kasier-windows with parameter 5 have been applied on both the range and the azimuth dimensions. When comparing these two figures it is easy to see how applying window functions in the SAR processing decreases the side-lobe level at the cost of lower resolution.

Due to the high number of scatterers there are several positions where there are two or more strong scatterers within one resolution cell. The very strong scatterer that appears in position X = 563.7, W = 2739.9 meters indicated with a circle, is an example. Similar to real measurements there are also many weak scatterers that are difficult or impossible to visually identify. The signals from these weak scatterers make the autofocus task challenging.

Figure 8.4.7 and 8.4.8 shows SAR images of the scene where a simulated phase error function is included. It is made by low-pass filtering Gaussian white noise in an effort to generate an arbitrary but plausible function. The standard deviation is $5\pi/16$ radians which is substantial. The signals in positions 280 and 450 on the synthetic aperture are in approximately opposite phase. To make the simulated received signal as realistic as possible, we have added Gaussian distributed white noise corresponding to a noise temperature of 1500 Kelvin. Compared to figure 8.4.5 and 8.4.6 the images appear very blurred in the azimuth direction indicating

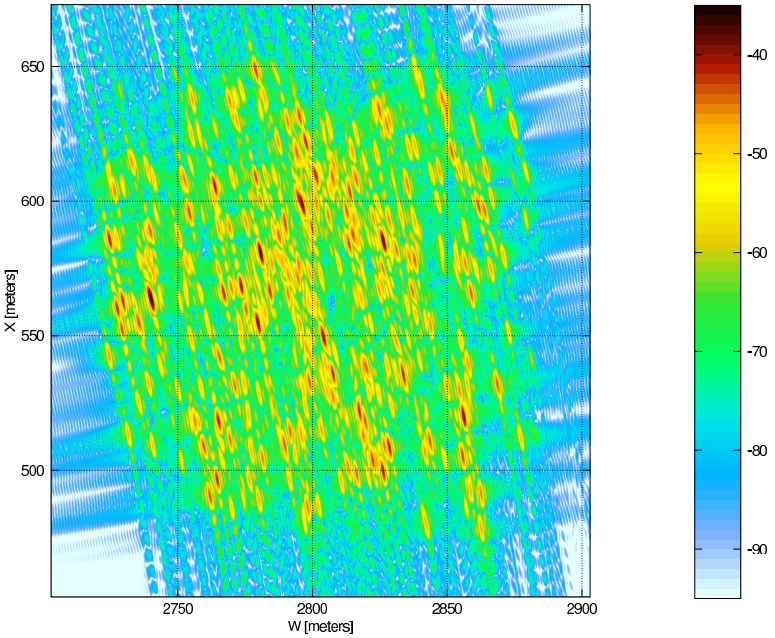


Figure 8.4.5: SAR image of simulated scene with zero phase error function

substantial phase errors along the synthetic aperture.

The simulated phase error function is shown as the blue curve in figure 8.4.9.

#### 8.4.3.2 First processing

The unfocused SAR image as shown in figure 8.4.7 is rather blurred in the azimuth direction indicating substantial phase errors along the synthetic aperture. In the first autofocus processing we have therefore replaced the clean-algorithm subtraction with a scatterer removal procedure as described in section 8.4.2.1.

Figure 8.4.10 shows the same unfocused SAR as in figure 8.4.7, but in linear colour scale. Imposed on the image are small black dots in the positions where the algorithm has identified scatterers. As can be seen, most of the strongest scatterers have been identified, but it is also possible to find weak scatterers that have not been identified such as in coordinates W = 2736, X = 579 meters. In this processing the estimation of scatterers was stopped when the maximum of the residual image was less than 0.4 compared to the strongest estimated scatterer. It makes little sense to try to estimate much weaker scatterers. The scatterer removal process, multiplication with a function that has zero-value in the position of the scatterer, may produce peaks in the close vicinity which are not peaks in the original image.

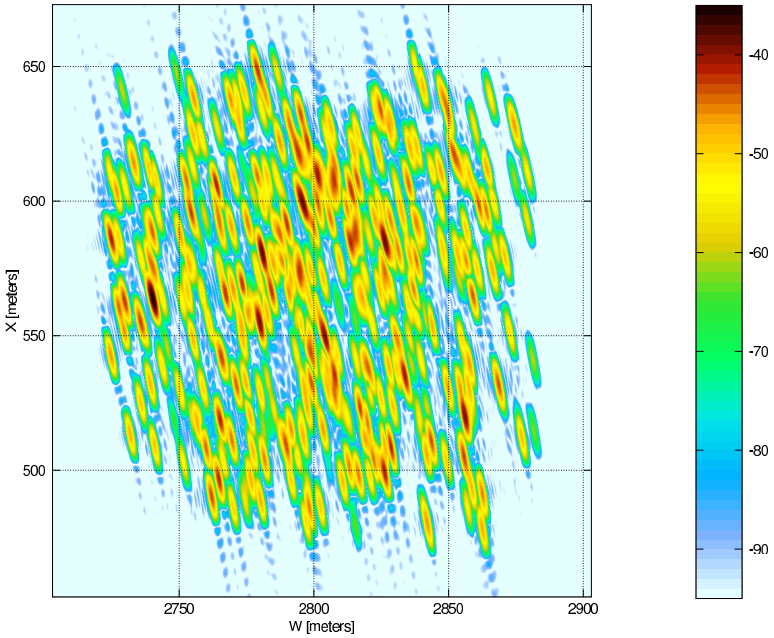


Figure 8.4.6: SAR image of simulated scene with zero phase error function, processed with Kaiser window.

The estimated phase error function is plotted as the green curve in figure 8.4.9. On some parts of the synthetic aperture the estimated phase error is close to the actual phase error function, blue curve. On other parts the estimate does not really reduce the error magnitude. On average the remaining phase error function has smaller magnitude.

#### 8.4.3.3 Second processing

Before the second autofocus processing a new SAR image was processed where the phase error estimate from the first autofocus processing was used as a correction. In this way the task of identifying scatterers became easier because of reduced blur. In this second processing we used the regular *clean*-algorithm subtraction and a threshold function as described in section 8.3.2.3. The final single phase error function estimate (the sum of the first and second processing estimates) is shown as the red curve in figure 8.4.9. As can be seen the estimate is very close to the simulated phase error function for all positions on the synthetic aperture.

Figures 8.4.11 and 8.4.12 show the SAR image when the radar data has been corrected with the final phase error function estimate.

In the last figure Kaiser windows have been applied in the processing. When

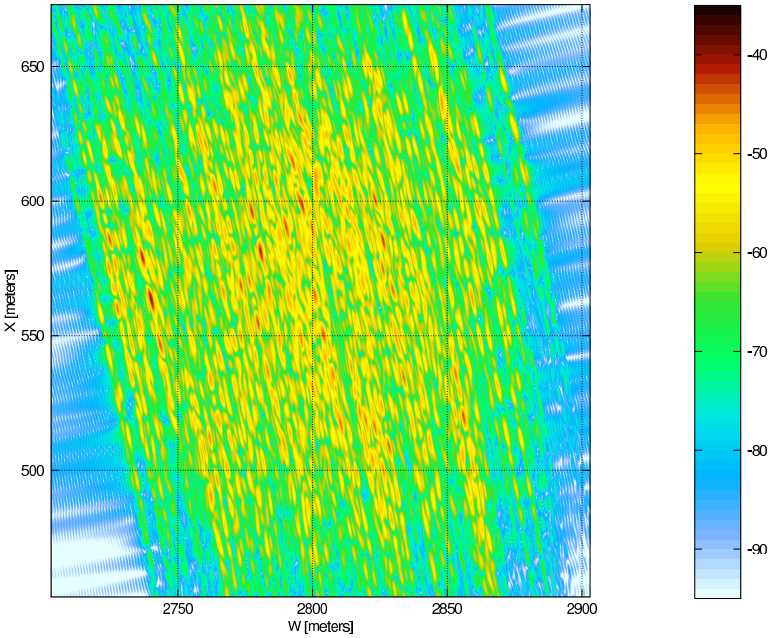


Figure 8.4.7: SAR image of simulated scene with non-zero phase error function.

comparing figure 8.4.11 to figure 8.4.5 and figure 8.4.12 to figure 8.4.6 we see that all strong scatterers are essentially equal. The only visual difference is the very weak residual response outside the target area.

## 8.5 Error analysis

The SMA-algorithm relies on all scatterers in the scene being estimated correctly, both magnitude and position. But since the estimation is done using the SAR image data processed with uncompensated phase errors, the scatterer estimations will have errors. In this section we will analyse the impact of errors done in the estimation of the scatterers.

As described in section 8.4.2 the phase error estimate for range-arc $l$ is calculated by

$$\Delta\hat{\phi}_e[m] = \angle A_p[m]\, A_{ps}[m]^* \tag{8.5.1}$$

where $m$ is the index to the position on the synthetic aperture. The measured aperture function $A_p[m]$ and the aperture function calculated from the estimated scatterers $A_{ps}[m]$ are related to the actual and estimated scatterers by

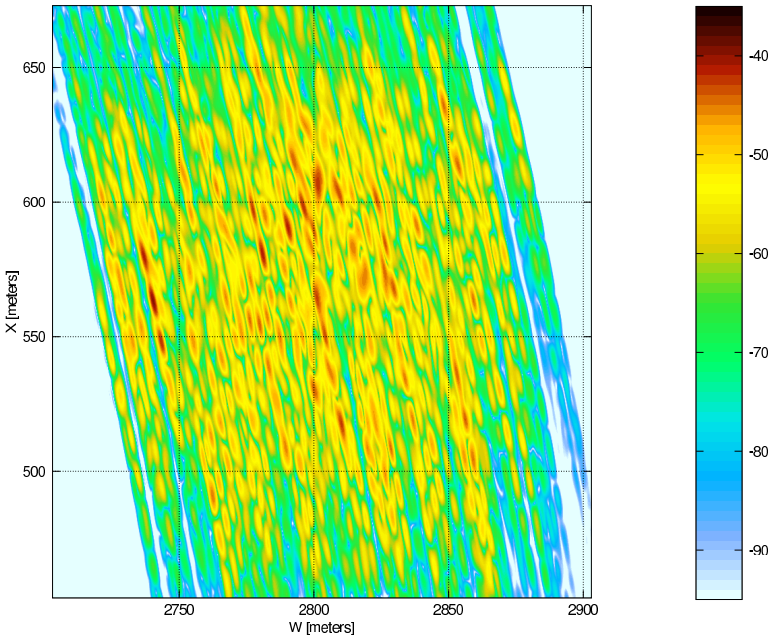


Figure 8.4.8: SAR image of simulated scene with non-zero phase error function, processed with Kaiser window.

$$A_p[m] = \sum_{n=1}^{N} a_{tn} e^{\jmath(\phi_{tn}[m]+\Delta\phi_e[m])} \tag{8.5.2}$$

$$A_{ps}[m] = \sum_{n=1}^{N} \hat{a}_{tn} e^{\jmath\hat{\phi}_{tn}[m]} \tag{8.5.3}$$

Here $a_{tn}$ and $\hat{a}_{tn}$ are actual and estimated scatterer magnitude, $\phi_{tn}$ and $\hat{\phi}_{tn}$ are the actual and estimated scatterer phase, both for scatterer $n$. The actual phase error function is given by$\Delta\phi_e[m]$. Inserting equations 8.5.2 and 8.5.3 into equation 8.5.1 gives

$$\Delta\hat{\phi}_e[m] = \underbrace{\angle\sum_{n=1}^{N} a_{tn} e^{\jmath\phi_{tn}[m]} - \angle\sum_{n=1}^{N} \hat{a}_{tn} e^{\jmath\hat{\phi}_{tn}[m]}}_{\phi_{err}[m]} + \Delta\phi_e \tag{8.5.4}$$

If $\hat{a}_{tn} = a_{tn}$ and $\hat{\phi}_{tn} = \phi_{tn}$ then $\phi_{err}[m] = 0$ and the phase error function estimate is correct, $\Delta\hat{\phi}_e = \Delta\phi_e$. Errors in the estimated scatterer magnitudes and/or phases will generally give $|\phi_{err}[m]| > 0$.

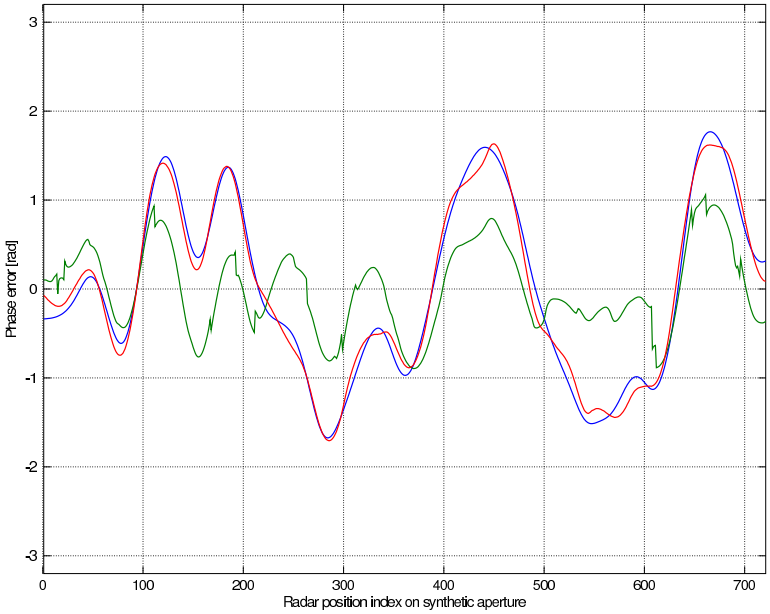


Figure 8.4.9: Blue: simulated phase error function. Green: estimated phase error function after first processing. Red: estimated phase error function after second processing.

### 8.5.1 Error in the estimated scatterer position

To simplify we will assume that there is only on scatterer in the scene, $N = 1$. The phase of the scatterer is given by the distance from the radar to the scatterer

$$\phi_t[m] = \frac{4\pi}{\lambda}\sqrt{(R_t \sin\theta_t - m\Delta x_r)^2 + (R_t\cos\theta_t)^2} \tag{8.5.5}$$

where $R_t$ and $\theta_t$ are the radial range and arc-angle to the scatterer and $\Delta x_r$ is the separation between positions on the synthetic aperture. Since we assume $a_t = \hat{a}_t$, we have $\phi_{err}[m] = \phi_t[m] - \hat{\phi}_t[m]$.

#### 8.5.1.1 Error in the estimated scatterer range $\hat{R}_t$

Expressing $\phi_{err}[m]$ as a function of the error in the estimated range $\Delta R_t$ gives

$$\phi_{err}[m] \approx \frac{\partial\phi_t}{\partial R_t}\Delta R_t = \frac{4\pi}{\lambda}\frac{R_t - m\Delta x_r\sin\theta_t}{\sqrt{R_t^2 - 2R_t m\Delta x_r\sin\theta_t + (m\Delta x_r)^2}}\Delta R_t \tag{8.5.6}$$

Since $R_t \gg m\Delta x_r$ and $\theta_t$ is a small angle, we may approximate

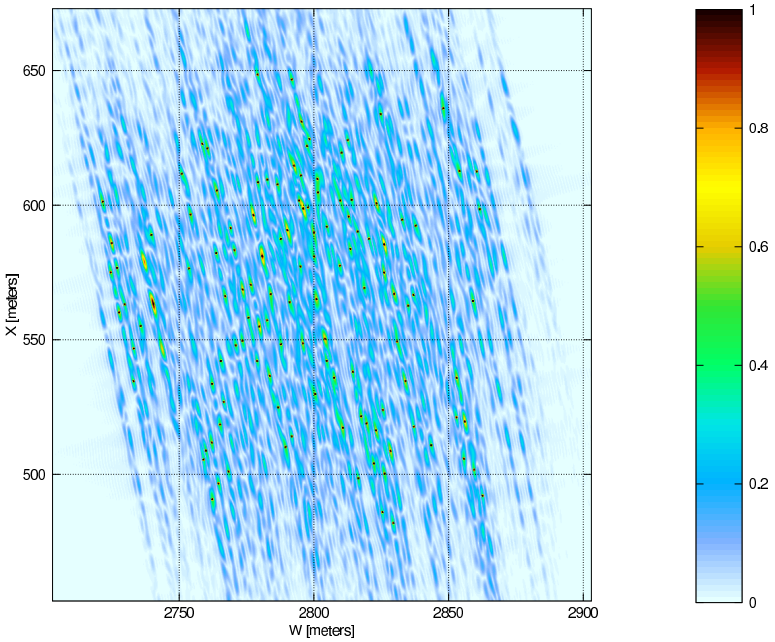


Figure 8.4.10: Estimated scatterers after first autofocus processing.

$$\phi_{err}[m] \approx \frac{4\pi}{\lambda}\Delta R_t \tag{8.5.7}$$

An error in the estimated scatterer range gives a directly proportional error in the estimated phase error. But since it is a constant function (not a function of the position on the synthetic aperture), is will not cause any defocus effects and cannot be corrected by autofocus procedures.

#### 8.5.1.2 Error in the estimated scatterer arc-angle $\hat{\theta}_t$

Expressing $\phi_{err}[m]$ as a function of the error in estimated arc position$\Delta\theta_t$ gives

$$\phi_{err}[m] \approx \frac{\partial\phi_t}{\partial\theta_t}\Delta\theta_t = -\frac{4\pi}{\lambda}\frac{R_t m\Delta x_r \cos\theta_t}{\sqrt{R_t^2 - 2R_t m\Delta x_r \sin\theta_t + (m\Delta x_r)^2}}\Delta\theta_t \tag{8.5.8}$$

Since we still have that $R_t \gg m\Delta x_r$ and $\theta_t$ is a small angle, we may approximate

$$\phi_{err}[m] \approx -\frac{4\pi}{\lambda}m\Delta x_r\Delta\theta_t \tag{8.5.9}$$

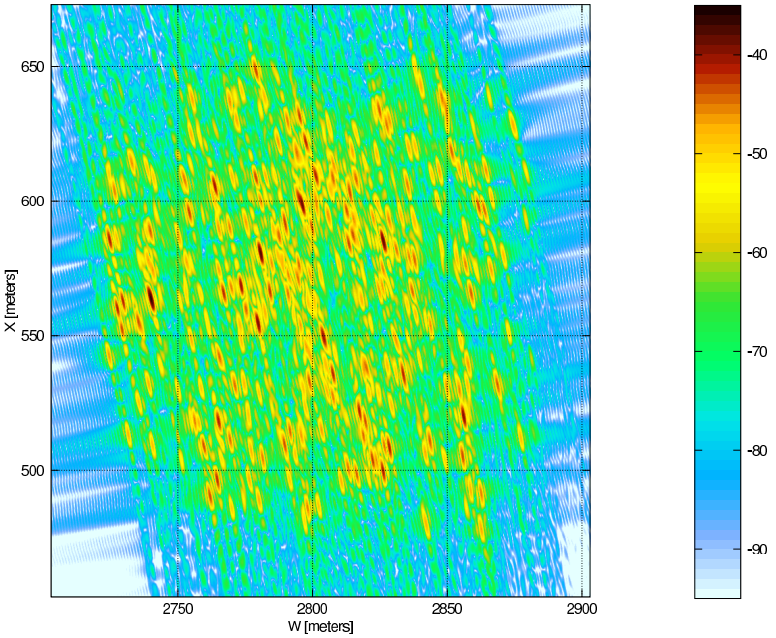


Figure 8.4.11: SAR image of simulated scene processed with final estimated phase error function.

An error in the estimated scatterer arc-angle gives an error in the estimated phase error which is a first order function along the synthetic aperture. The largest error will be at the end of the synthetic aperture, $m\Delta x_r = L_a/2$. Using values for GinSAR from chapter 10 and $\Delta\theta_t = 0.357$ milli-rad (1 meter on the arc at $R_t = 2803$ meters), gives $\phi_{err} = 30$ degrees. If there are two or more scatterers with different magnitude, the error function $\phi_{err}[m]$ will in general be of higher order.

### 8.5.2 Error in the estimated scatterer magnitude $\hat{a}_t$

In this case we assume that the estimated phase is correct, $\hat{\phi}_t = \phi_t$. Then if there is only one scatterer in the scene, an error in the estimated scatterer magnitude $\hat{a}_t$ will not generate any error in the phase error function estimate. But with two or more scatterers it is possible. This is explained in figure 8.5.1.

In this example there are two scatterers where the aperture functions for each scatterer is shown as vectors in the complex plane. Since we are interested in the sum, the vectors are drawn head to tail. The actual measured scatterers are shown as blue vectors with magnitudes $a_{t1}$ and $a_{t2}$. The aperture functions for the estimated scatterers are shown as red vectors with magnitude $\hat{a}_{t1}$ and $\hat{a}_{t2}$.

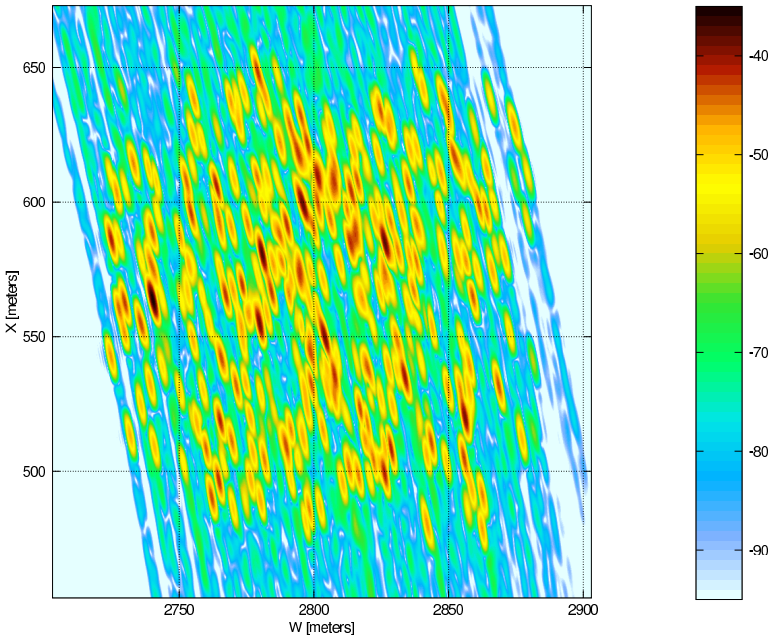


Figure 8.4.12: SAR image of simulated scene processed with final estimated phase error function, processed with Kaiser window.

As can be seen, the angle for each scatterer/vector is correct but the magnitudes have errors. Because of these error there will an error in the phase error function estimate. The magnitude of $\phi_{err}$ depends on the magnitude ratio $a_{t2}/a_{t1}$ and angle difference $\phi_{t2} - \phi_{t1}$. The worst situation is when $a_{t2}/a_{t1} \approx 1$ and $\phi_{t2} - \phi_{t1} \approx \pi$ radians, ie. when the signal from the two scatterers almost cancel each other. In this case a small error in either $\hat{a}_{t1}$ and/or $\hat{a}_{t2}$ may turn the sum vector close to $\pi$ radians.

Figure 8.5.1 shows the situation for one fixed position on the synthetic aperture. As the position on the synthetic aperture is changed, the angles $\phi_{t1}$ and $\phi_{t2}$ changes according to equation 8.5.5. If there are two scatterers of approximately equal magnitude at different arc-angles, there will typically be one or more positions on the synthetic aperture where $\phi_{t2} - \phi_{t1} \approx \pi$ and the $\Delta\hat{\phi}_e$-estimate becomes very uncertain. These positions can be identified by the sum $\sum_{n=1}^{N} a_{tn} e^{j\phi_{tn}[m]}$ being small. When calculating the weighted average from all range-arcs in the close set (see section 8.4.2) this range-arc at the position with uncertain $\Delta\hat{\phi}_e$-estimate is given a small weight factor.

If there are one strong and one weak scatterer in the scene but for some reason we have only identified the strong scatterer, we have the situation shown in figure

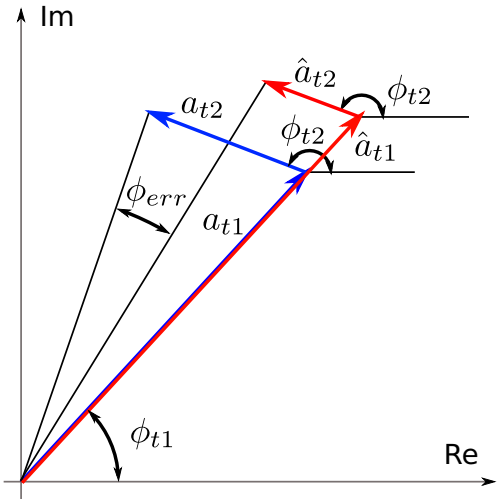


Figure 8.5.1: Error in estimated scatterer magnitude.

8.5.2.

As the position on the synthetic aperture is changed, the tip of the weak scatterer vector rotates around the tip of the strong scatterer vector. The bounds on the error in the phase estimate becomes

$$|\phi_{err}| \leq \arcsin \frac{a_{t2}}{a_{t1}} \tag{8.5.10}$$

From this result we conclude that the identification of weak scatterers becomes important in the last iterations to achieve the most accurate phase error function estimate. In practice there is a limit where trying to estimate more scatterers does not give smaller errors. This is because the estimates of weak scatterers typically have larger errors in position and magnitude than strong scatterers due to lower signal-to-noise ratio.

All these analysis concerns only one range-arc. When estimating one single phase error function we first identify the function estimates that resembles each other into a close-set. The final single estimate is calculated as a weighted average. Using this procedure the final estimate is rather insensitive to large errors in some scatterer estimates as long as there are other range-arcs that have small errors.

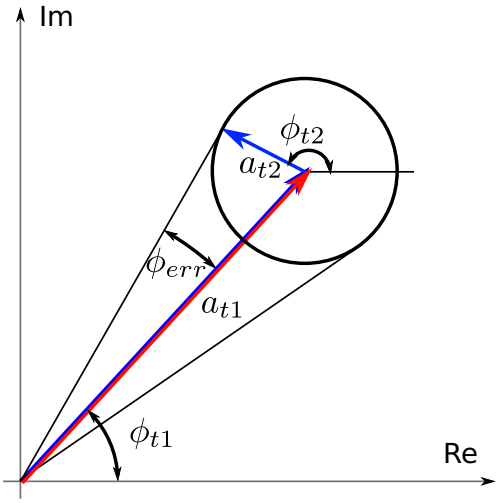


Figure 8.5.2: Error when a scatterer has failed to be estimated.

# Chapter 9

# Synthetic aperture length

As described in section 10.1.2 the position of the radar on the synthetic aperture was measured by a distance wheel rolling on the back-most rail. The distance wheel had an optical encoder attached to its axis. The starting position was fixed by a solid metal structure. But the stop position after having rolled along the whole railway length, showed some variations in the milli-meter range corresponding to a relative error less than 1/1000. By inspection the variation was slowly changing, the difference in stop position between to consecutive measurements were very small. Since we were unable to observe any variations in the stop-angle of the distance wheel, there must have been some variable slip between the wheel and the rail. The distance wheel axis rolling friction is very small due to roller bearings, it seemed unlikely that the observed variations could have this explanation. The most likely cause is that the distance wheel axis was not exactly perpendicular to the rail at all times forcing some movement/slip between the contact areas on the wheel and the rail. The amount of movement/slip will likely vary as a function of factors such as temperature, humidity, dust on the rail etc. Since variations in the length of the synthetic aperture may very well occur for other arrangements than a railway too, we have analysed the impact and sought some compensating action.

**Impact of errors in synthetic aperture length** The distance between pulse transmission positions on the aperture is given by

$$d = \frac{2L}{M-1} \tag{9.0.1}$$

where $2L$ is the total length of the synthetic aperture and $M$ is the number of pulse transmission positions. We will make the assumption that $d$ is constant for each SAR measurement. And we will also assume that the waves impinging on the synthetic aperture have a plane wave front (reflecting scatterer at infinity). The scattering squint angle shown in figure 9.0.1 is then related to $d$ by

$$\theta_t = \arcsin \frac{\lambda}{4\pi} \frac{\Delta\phi}{d} \tag{9.0.2}$$

where $\Delta\phi$ is the measured phase difference between the two adjacent pulse transmission positions, see figure 9.0.1. An error in the assumed distance between pulse transmission positions on the aperture $d_a$ will have no impact if $\Delta\phi = 0$ since then we also have $\theta_t = 0$ (a broadside located scatterer). If $\Delta\phi > 0$ and $d_a < d$, $\theta_t$ will be calculated to be larger than the correct squint angle. Since the effect is proportional to $\theta_t$, the SAR image appears to be stretched away from the azimuth centre. When comparing many SAR images the squint angle of a fixed target will therefore show some variation due to variations in $d$.

In addition there will be variations in the calculated interferometric phase of a squinted target position because it is only the stop position that varies. The net effect is that the centre of the synthetic aperture is moved by half of the variation in the stop position. The range to a squinted target will change equal to the change in synthetic aperture centre position projected into the direction towards the target position. This is shown in figure 9.0.1 as $\Delta r$. The assumed synthetic aperture length is $2L_a$, and the corresponding pulse transmission positions are indicated with the red crosses. The actual length is $2L = 2(L_a + \Delta L)$ where the associated pulse transmission positions are indicated with blue circles.

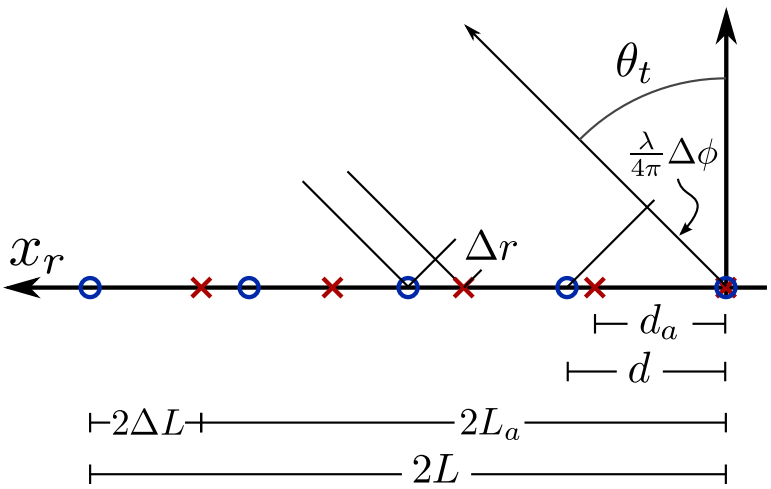


Figure 9.0.1: Range error caused by error in synthetic aperture length. For simplicity there is only 5 positions on the synthetic aperture in this figure.

The change in range towards the squinted target becomes $\Delta r = \Delta L \sin\theta_t$.

For a reflector at finite distance there will an additional effect similar to a second order phase error function (PEF). But for the synthetic aperture lengths and target area ranges typically encountered in GinSAR, this second order PEF has small magnitude.

**Compensation** We will make the assumptions that there is a strong fixed point scatterer at some squint angle $\theta_t$ and that the measured interferometric phase difference $\Delta\phi_n$ for SAR image $n$ has no errors (it is correct for the given $d_n$). The calculated squint angle for SAR image $n$ then becomes using equation 9.0.2

$$\theta_{tna} = \arcsin \frac{\lambda}{4\pi} \frac{\Delta\phi_n}{d_{na}} \tag{9.0.3}$$

where $d_{na}$ is $d_a$ for SAR image $n$. If $d_{na}$ was replaced by the correct $d_n$ in equation 9.0.3 the correct and constant $\theta_t$ would have been calculated. Hence, the ratio $\Delta\phi_n/d_n$ is constant.

To find an estimate for $d_n$ we will demand

$$\frac{\Delta\phi_n}{d_n} = \frac{\bar{\Delta\phi}}{d_{na}} \tag{9.0.4}$$

where $\bar{\Delta\phi}$ is the average of all $\Delta\phi_n$. By solving for $d_n$ we get

$$d_n = d_{na} \frac{\Delta\phi_n}{\bar{\Delta\phi}} = d_{na} \frac{\sin\theta_n}{\frac{1}{N}\sum_{n=1}^{N} \sin\theta_n} \tag{9.0.5}$$

where $N$ is the total number of SAR images. The estimate of the error in the length of the synthetic aperture becomes

$$\Delta L_n = \frac{1}{2}(M-1)d_n - L = L\left(\frac{\sin\theta_n}{\frac{1}{N}\sum_{n=1}^{N} \sin\theta_n} - 1\right) \tag{9.0.6}$$

where $M$ is the number of positions on the synthetic aperture. Note that this estimate of $\Delta L_n$ is found by averaging the sinus of the squint angle. Hence, the estimation is only able to estimate the variations in $\Delta L_n$ and not a common offset.

# Chapter 10

# Radar on rails measurements

## 10.1 Measurement description

The railway was set up on the roof of NGI's building in Oslo approximately 17 meters above ground level illuminating the hill "Vettakollen". This site was chosen because it was practical. Testing the radar in some location where there actually is an unstable slope would have been better, but with limited resources we concluded that the chosen site was our best option. Hence, the purpose with these measurements have been to determine the performance of the radar including all post processing as discussed in previous chapters. It was not to conduct geo-technical useful or interesting measurements.

### 10.1.1 The radar site

The target area is described in section 10.1.3, here we will discuss the potential problem of placing the radar on the roof of a building. Since we calculate any movement within the target area by distance measurements between the radar and the target area, the radar should not move between the measurements. As a concrete structure the building will expand and contract with temperature changes. Course calculations have shown that the position of the radar on the roof will move 0.3 milli-meters towards the target area for each degree Kelvin increase in the concrete. The temperature span during the measurements was 3.5 C° which should give approximately 1 milli-meter movement. The actual movement is likely much less since the inside of the building is air-conditioned with constant temperature. We tried to measure the length of the roof using a laser distance meter during part of the measurement period without being able to observe any changes. We therefore conclude that the temperature induced movement of the roof is so marginal that no compensating action was required.

After having setup the radar and conducted some measurements it became evident that the second amplifier in the receiver saturated. We firmly believed that the problem was caused by the side-wall of a school-building on the other side of the road approximately 200 meters away from the radar. An antenna-side-

lobe that illuminated this wall gave a too strong reflected signal because of the short distance. We were therefore forced to reduce the amplification in the receiver to avoid saturation. In general, when given a slope to monitor, finding a suitable place to setup the radar can be a challenging task.

### 10.1.2 The railway

The length of the rails were 13.5 meters. We would prefer to use a length of 30 meters as that would give approximately equal resolution in range and cross-range, but the length was limited by the size of the roof. The moving distance of the wagon, the length of the synthetic aperture was measured to be $L_a = 12.133$ meters. The rails were made of rectangular aluminium tubes of length of 3 meters. They rested on sleepers in both ends at the joint to the next rail. The height and width of the rails were 80 and 50 milli-meter, respectively. We were not able to observe any vertical deflection of the rails due to the weight of the wagon. When setting up the railway we tried as far as possible to make the synthetic aperture a straight line by adjusting the sleeper support individually. By using a laser beam pointing at a flat target screen that were moved along on the top of the rails, the deviation from a straight line seemed to be less than 10 milli-metres.

The wagon was constructed with three wheels to maintain constant weight on each wheel as the wagon rolled, two wheels on the front-side and one on the back-side rail. This construction gave less sidewise wobbling. The antennas were mounted on top of the wagon approximately 1.3 meters above the rails. The mechanical antenna mounting allowed adjustment of the pointing direction both in elevation and in azimuth. The position of the wagon along the rails was measured using a distance wheel connected to an optical encoder which rolled on the back-side rail. The start position on the rails was mechanically fixed. The stop position, set by the distance wheel measurements, showed some slowly changing milli-meters variation. The wagon was moved forward by an electric motor pulling a tight wire. The motor was controlled by the radar micro-processor. Both front-side wheels were made with flanges both on the inside and outside to limit the sidewise position of the wagon on the rails. The opening between the inner and outer flange were 2 milli-metres wider than the width of the rail. By observation both the inner and outer flanges where in contact with the rail at different times during the travel along the rail. But the sidewise position of the wagon on the rails seemed very repeatable among the runs.

The radar was programmed to conduct 721 frequency sweeps along the synthetic aperture giving 16.9 milli-meter between each pulse transmission. The time to finish all 721 measurement pulse transmissions (one complete SAR measurement) was 244 seconds, which gives a speed on the rails equal to 49.7 milli-meters per second. The pulse transmission time (chirp sweep-time) was programmed to 15.358 milli-second. The movement on the rails during the pulse transmission time then became 0.76 milli-meters. Figure 2.4.5 shows the wagon with the antennas and the electronics on the railway. Figure 10.1.1 shows the radar on the roof of the building. Figure 10.1.2 shows the distance-wheel and the wire-wheel connected to


Figure 10.1.1: The radar on the roof of the building.

the electrical motor.

### 10.1.3 Target area

The target area "Vettakollen", is a hill where the most distant part are more than 3000 meters away from the radar. This hill is geological stable. Ideally our measurements should therefore indicate zero movement. Unfortunately the area consist of forest with rather dense vegetation. We were only able to find two positions on the ground with a clear view towards the radar. At both these openings we mounted flat plate reflectors. The reflector at the top of the hill furthest away from the radar had a theoretical radar cross section (RCS) of 826 $m^2$, the RCS of the lower reflector were theoretically 293 $m^2$. The actual RCS were less because of pointing direction errors and the plates not being perfect flat.

Figure 10.1.3 shows a topographic map of the target area.

The position of the reflectors are indicated with red shaded circles. Relative to the synthetic aperture the reflectors are located at squint (azimuth) angles of 11.5 degrees (top reflector) and 10.7 degrees (lower reflector). The pointing direction of the antennas were adjusted to point towards the reflector both in azimuth and elevation. Figure 10.1.4 shows a photo of the target area as seen from the radar.

Figure 10.1.5 shows a vertical cross-section of the propagation path. Note that the scale of the horizontal and vertical axis are different.

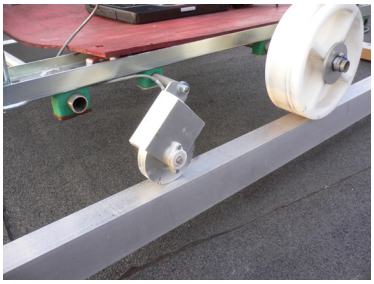


Figure 10.1.2: The distance-wheel and the electrical motor with the wire-wheel.

### 10.1.4 Completion of measurement series

In total 175 measurements were conducted during a period of almost 25 hours starting on the 23'th October 2011 at time 15:24. With a few exceptions the average time between the measurements were approximately 8 minutes. Detailed data of the meteorological conditions during the measurement period is described in section 10.3.1.1. Here we will limit us to say that the conditions were fairly stable, relative small temperature changes, little wind, overcast but no fog.

## 10.2 Autofocus and SAR magnitude image

### 10.2.1 SAR magnitude image without autofocus

Figure 10.2.1 shows the processed SAR magnitude image for one arbitrary measurement.

The colour-coding is in Decibel. The received power level which saturates the receiver is used as 0 dB reference level. In this processing it is assumed that the synthetic aperture is a straight line (no autofocus) and the the length of the aperture is exactly 12.133 meters.

The two reflectors are clearly visible at the w- and x-coordinates (2800, 568) meters (reflector 1) and at coordinates (2343, 443) meters (reflector 2). Except for the placed out reflectors the strongest natural reflectivity is mostly found in the same areas as the reflectors. This is as expected because in these areas there are some smaller patches with bare rock surface. In general the natural reflectivity is rather small because of dense vegetation.

Figures 10.2.2 and 10.2.3 show scaled subsections of figure 10.2.1 around the reflectors. Both reflectors and the other natural scatterers appears somewhat blurred indicating phase errors in the SAR processing. Notice that both reflector responses appears to be similarly blurred.

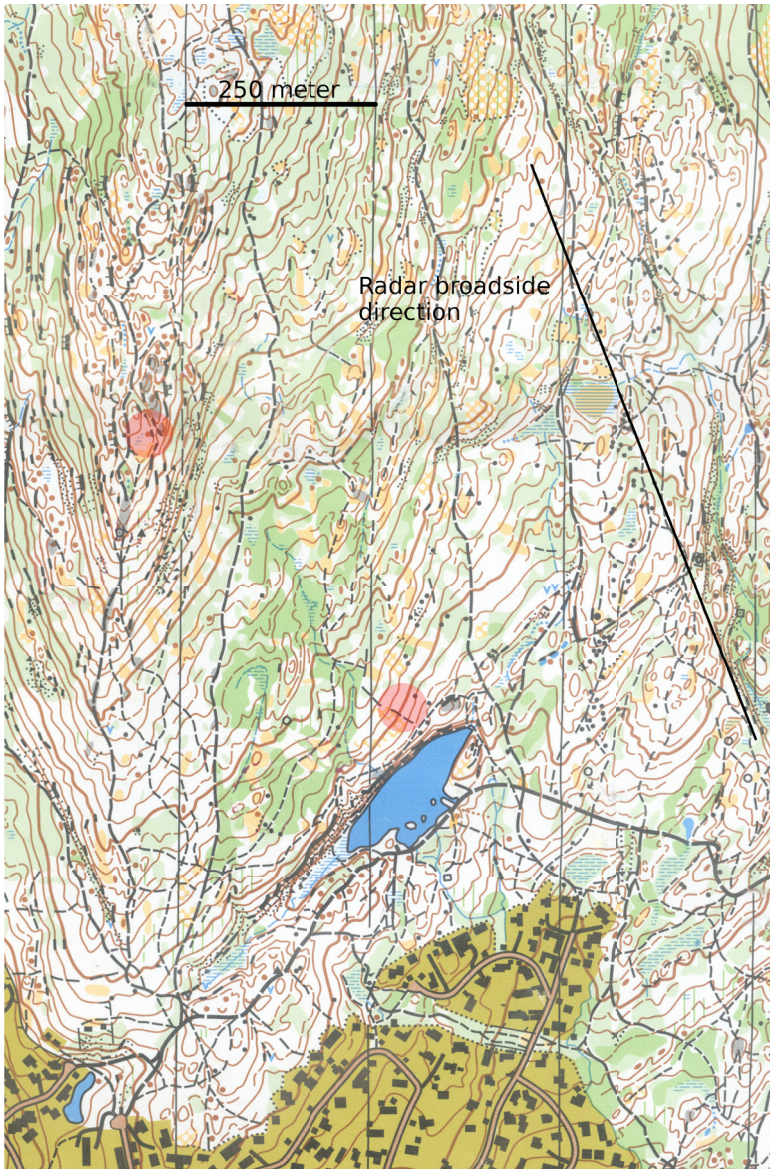


Figure 10.1.3: Topographic map of target area.

Figure 10.1.4: Photo of target area seen from the radar.

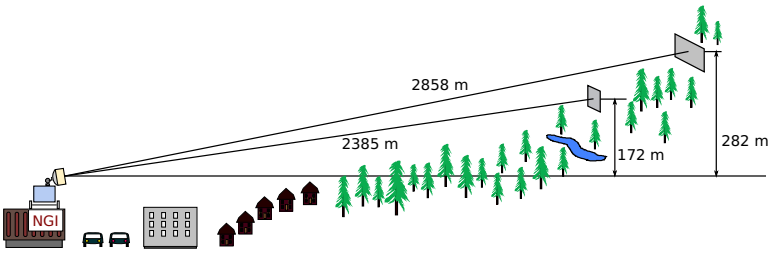


Figure 10.1.5: Vertical cross-section of the propagation path

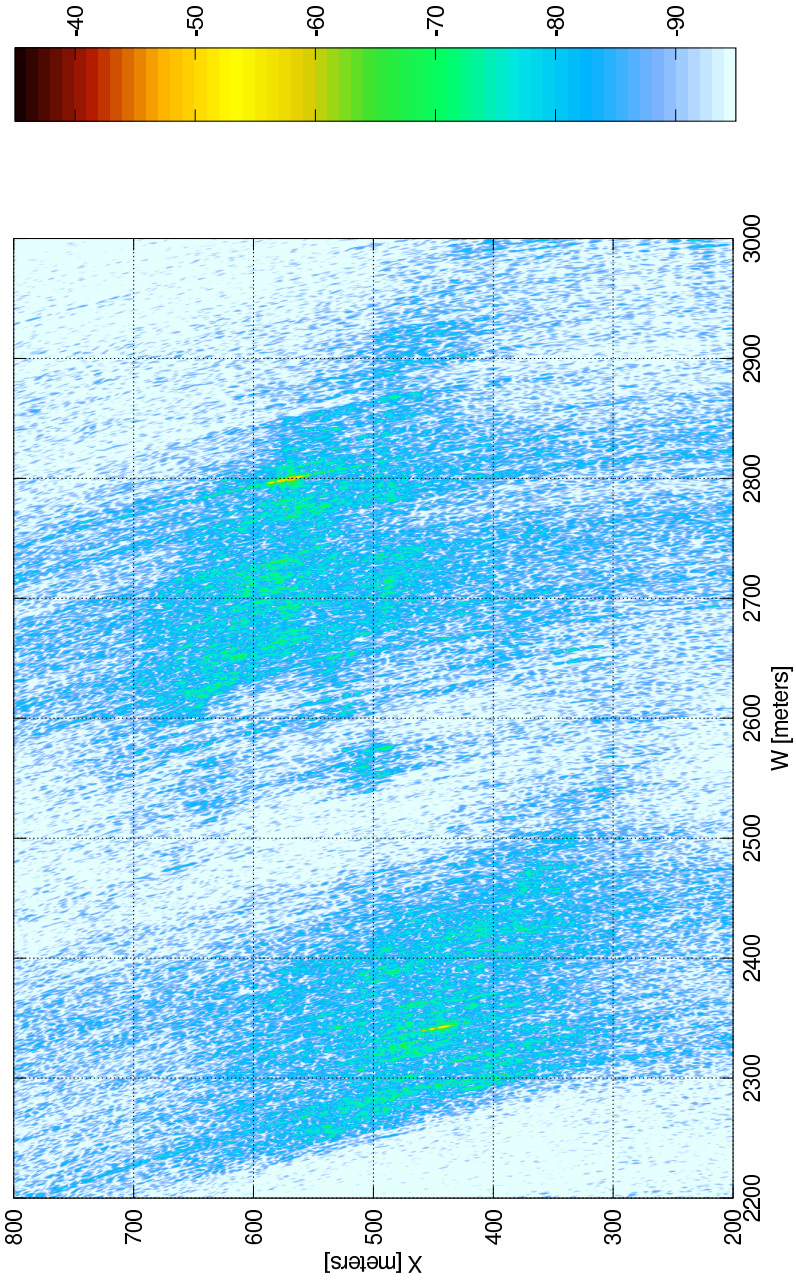


Figure 10.2.1: SAR magnitude image without autofocus.

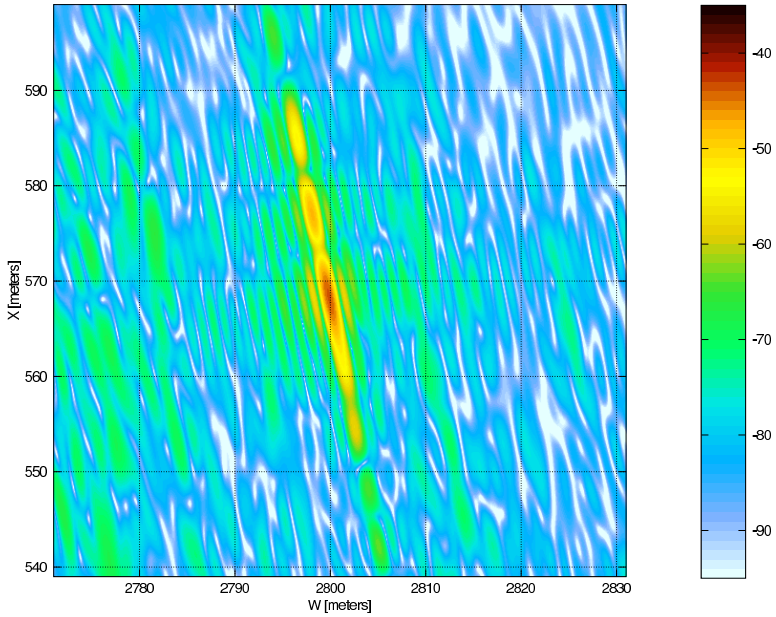


Figure 10.2.2: SAR magnitude image at reflector 1.

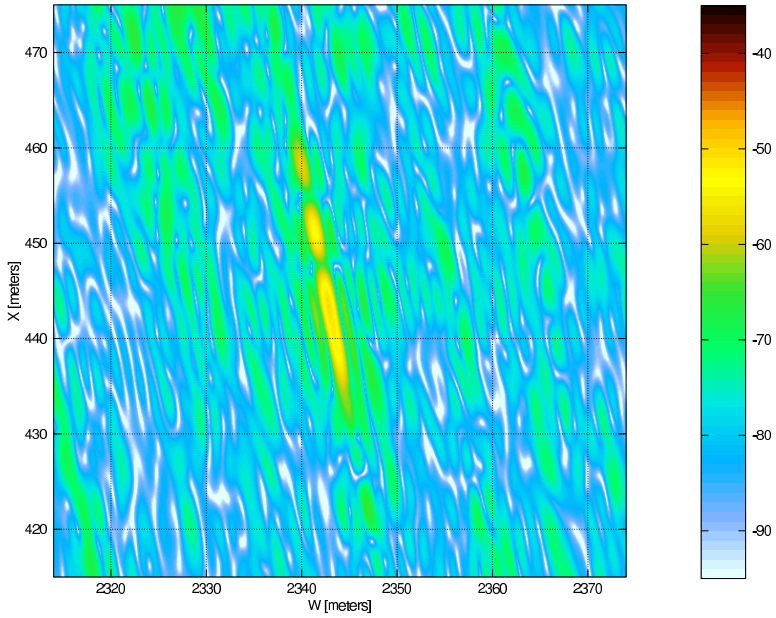


Figure 10.2.3: SAR magnitude image at reflector 2.

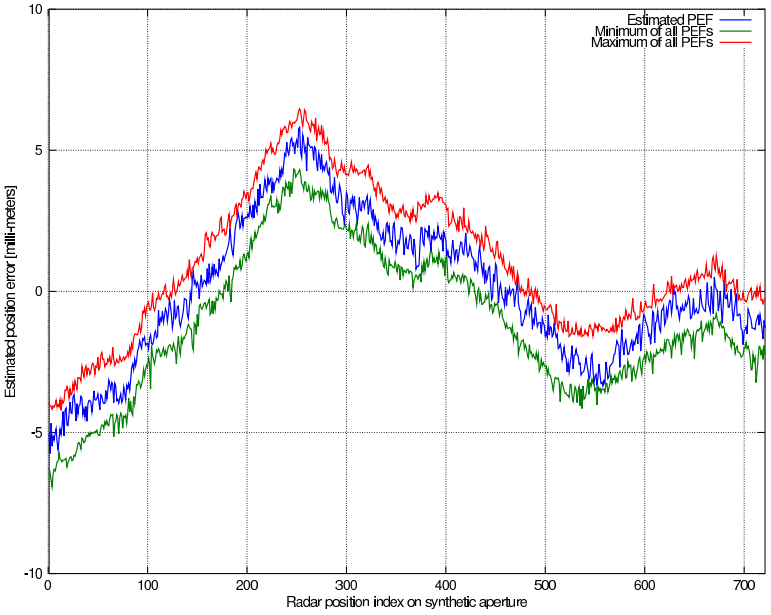


Figure 10.2.4: Estimated phase error function.

## 10.2.2 Autofocus

### 10.2.2.1 First iteration

We have estimated the phase error function (PEF) using the scatterer modelling autofocus algorithm (SMAA, 2 dimensional) described in section 8.4. In the first iteration the threshold function maximum was set equal to the magnitude of the identified scatterers. The threshold function width was set to approximately 2 times the azimuth resolution, and the floor level was set to 0.16 of the peak value. When using this threshold function only the two reflectors were identified as scatterers. This may seem as a very conservative choice of threshold function, but we have found that only estimating the strongest scatterers in the first iteration constitute a robust approach.

The middle blue curve in figure 10.2.4 shows the estimated position error of the same measurement as imaged in section 10.2.1. Instead of plotting all 175 estimated PEFs we have only shown the maximum (red upper curve) and minimum (lower green curve) position error that were estimated for each position on the synthetic aperture.

All the curves resembles each other rather well. The span between the maximum and minimum is approximately 2 milli-meters. This result supports our impression from section 10.1.2 that the sidewise position of the wagon on the rails

| scatterer no. | Relative Magnitude | X-position | W-position |
|---|---|---|---|
| 1 | 1.000 | 568.4 | 2799.9 |
| 2 | 0.2751 | 443.8 | 2342.8 |
| 3 | 0.0188 | 576.8 | 2731.1 |
| 4 | 0.0072 | 486.6 | 2388.8 |
| 5 | 0.0070 | 475.9 | 2328.9 |
| 6 | 0.0065 | 477.0 | 2326.5 |
| 7 | 0.0060 | 575.2 | 2781.5 |
| 8 | 0.0060 | 490.9 | 2575.8 |
| 9 | 0.0049 | 567.0 | 2692.4 |

Table 10.2.1: Scatterer magnitude and position estimated by the autofocus algorithm.

seemed very repeatable among the runs. However, due to small wind gusts we do not expect the estimated position error functions to be exactly equal. The variations among the estimated PEF can therefore not be interpreted as errors in the estimation.

The estimated PEF (blue curve) show some high frequency oscillations that are typical for all estimated PEFs. The magnitude is less than 1 milli-meters. We believe these oscillations are mostly electronic/measurement noise, a minor part may stem from vibrations in the antennas as the wagon rolls on the rails. Some of the slow drifts in the estimate could be caused by changes in the state of the atmosphere during the measurement time (244 seconds). Notice that neither the shown PEF (blue curve) or any other estimated PEF contain zero or first order terms.

#### 10.2.2.2 Second iteration

The estimated PEF found in the first iteration was used to correct the $w$-position of the radar in a second SAR processing. Using the resulting SAR magnitude image, a new PEF was estimated. In this iteration the width of the threshold function was reduced to 1.3 of the azimuth resolution and the floor level was set to 0.0049 of the peak value. Figure 10.2.5 shows the PEF estimated after the first iteration (blue curve, almost hidden by the red curve), the PEF estimated in the second iteration (green curve) and the accumulated PEF (red curve).

The PEF found in the second autofocus processing has a maximum magnitude of only a fraction of a milli-meter. Table 10.2.1 shows the magnitude and position of the identified scatterers.

Since the magnitude of the third strongest scatterer was only 0.019 relative to reflector 1, the impact of all the natural scatterers on the PEF were small. The error analysis outlined in section 8.5 supports that conclusion. For all practical purposes the optimal PEF was found already in the first iteration where only the two reflectors were identified as scatterers.

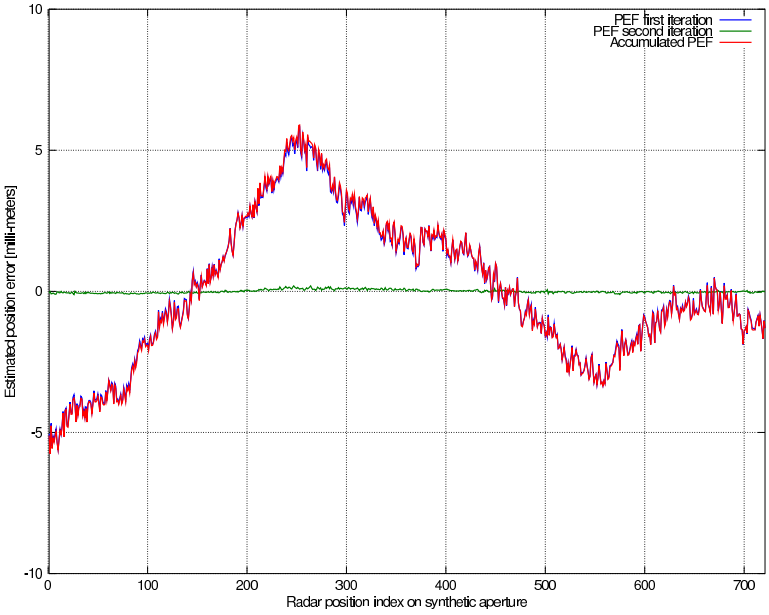


Figure 10.2.5: Estimated phase error functions after second iteration.

### 10.2.3 Synthetic aperture length

As a part of the autofocus algorithm the position to all identified scatterers are found. Using the positions of the strongest scatterer for each measurement, the length variation of the synthetic aperture is calculated as described in chapter 9. Figure 10.2.6 shows the estimated positions for the strongest scatterer among all measurements.

The spread in the azimuth direction is approximately 0.65 meters. In the estimation procedure we assume this is caused by variations in the length of the synthetic aperture. Figure 10.2.6 also shows that the estimated range to the scatterers are located in 3 range bins. This is a result of the algorithm used to estimate the scatterer position during the autofocus procedure described in section 8.4.2.3, step 4. The estimated range is adjusted by a fraction of a half wave length to make the phase equal to the phase of the actual measured scatterer. Since the range resolution is many times larger than the half of the wave length, there are several range-values close to the maximum of the magnitude function in the range dimension.

Figure 10.2.7 shows the estimated positions for the strongest scatterer among all measurements after the second iteration SAR and autofocus processing where the estimated deviation of the synthetic aperture length has been applied. The

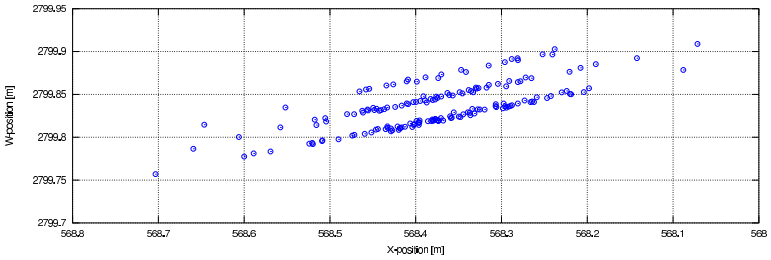


Figure 10.2.6: Estimated positions of the strongest scatterer.

spread in the azimuth direction is reduced to approximately 0.15 meters.

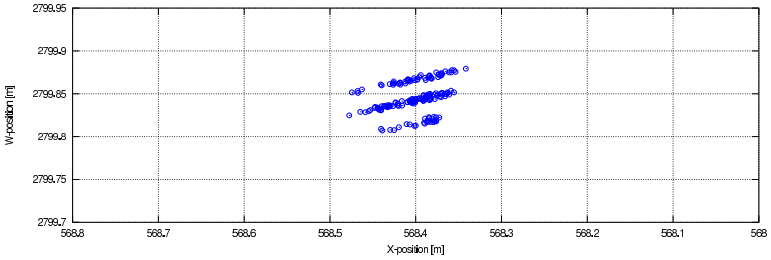


Figure 10.2.7: Estimated positions of the strongest scatterer after first iteration.

The estimated deviation in the length of the synthetic aperture is shown in figure 10.2.8.

When we observed the rolling distance during some parts of the measurement period, it changed slowly. We therefore believe the high frequency changes are mainly because of measurement noise and not deviations in rolling distance. The impulse response in the azimuth direction resembles a sinc-function which is flat on the top. Even noise of small magnitude can displace the peak position substantially. But the slowly varying part of the estimated deviations seems reasonable. The standard deviation of the estimated length is approximately 2.1 milli-meters. When projected into the direction towards the scatterer, it corresponds to 0.42 milli-meters. Since the change in interferometric range is only half of the span, the estimated magnitude variations in synthetic aperture length has only moderate impact even if not compensated.

### 10.2.4 SAR magnitude image with autofocus

Figure 10.2.9 shows the SAR magnitude image after the estimated autofocus function has been used in the SAR processing. The raw data stems from the same measurement as used in section 10.2.1.

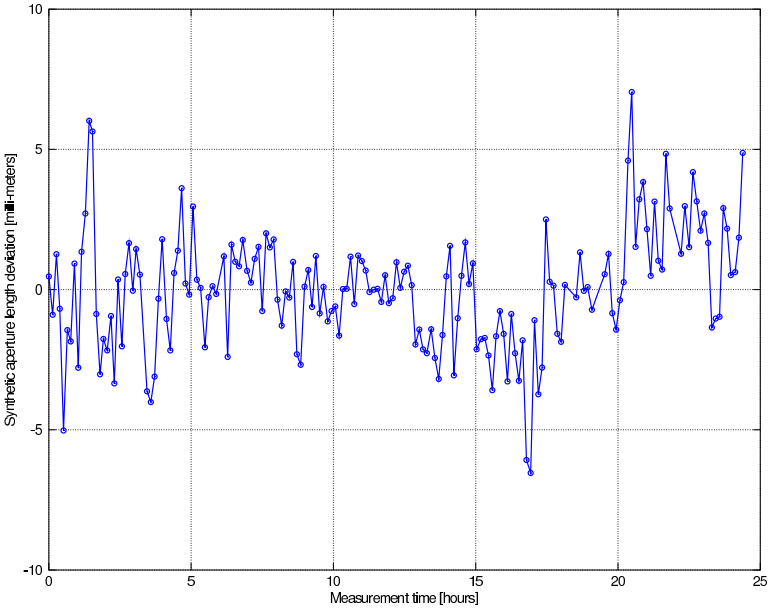


Figure 10.2.8: Estimated deviation in the length of the synthetic aperture.

The image shows that the magnitude difference between the reflectors is 5.6 dB. Theoretically this difference should only be $10\log\left((\sigma_1/\sigma_2)(R_2/R_1)^4\right) = 1.4\,\text{dB}$. We believe this can be explained by reflector and antenna pointing errors. The width of the reflecting lobe for our flat plate reflectors are very narrow around the normal vector. It was difficult to obtain accurate pointing direction when mounting the reflectors. In addition the reflectors used were not completely flat. By observation, the deviation from an exact flat surface was less than 2 millimeters in magnitude. Likewise the pointing direction of the antennas could also have been inaccurate even if we tried to point the antennas to the mid-point between the reflectors. The angle between the reflectors seen from the radar was 1.5 degrees. The half power lobe width of the antennas (transmission and reception combined) was approximately 4 degrees. Hence, if the antennas pointed exactly towards reflector 1, the response from reflector 2 would be reduced by almost 3 dB.

When comparing figure 10.2.9 to the same SAR magnitude image but without autofocus (figure 10.2.1), it appears to be less blurred in the azimuth direction. This is perhaps easier to see when comparing the scaled subsection around reflector 1 shown in figure 10.2.10 with figure 10.2.2.

The maximum magnitude of the reflectors is 1.63 dB higher (-42.04 - (-43.67)). The image in the vicinity of the reflector much better resembles a two-dimensional

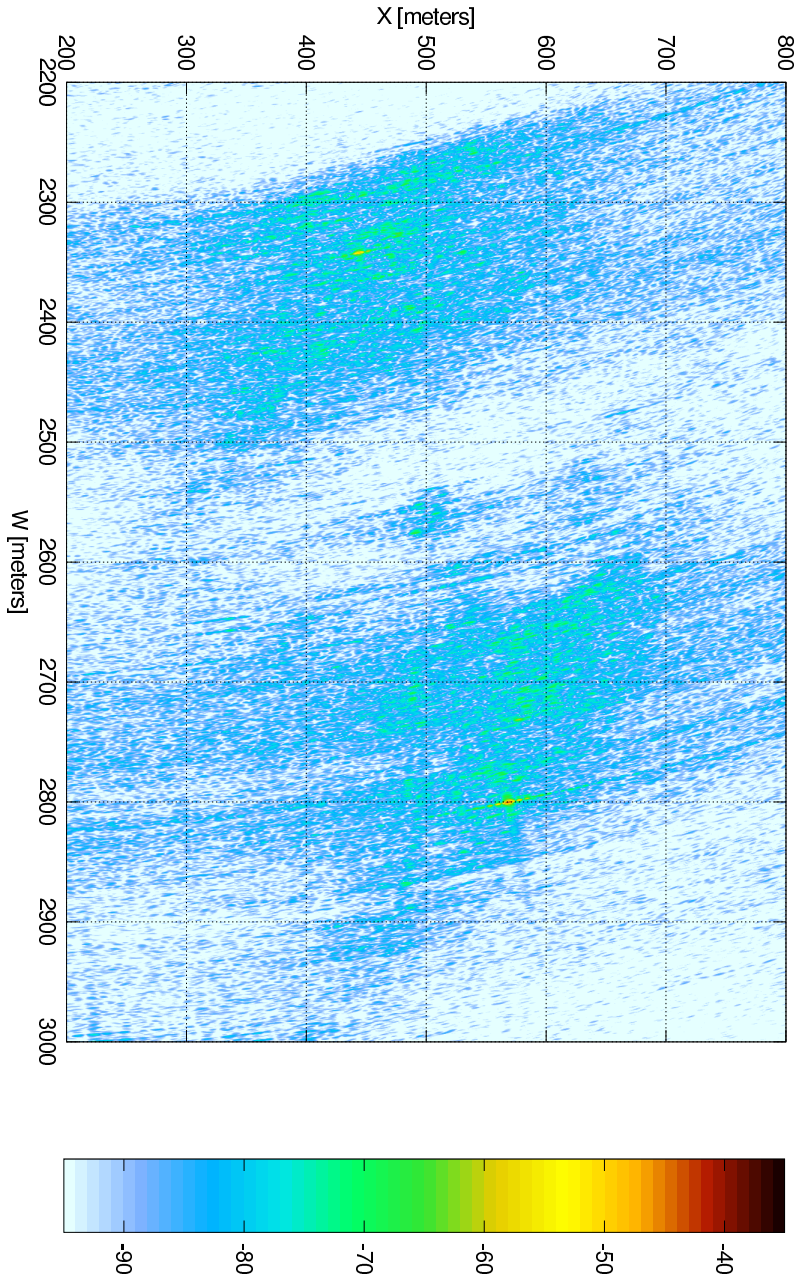


Figure 10.2.9; SAR magnitude image with autofocus.

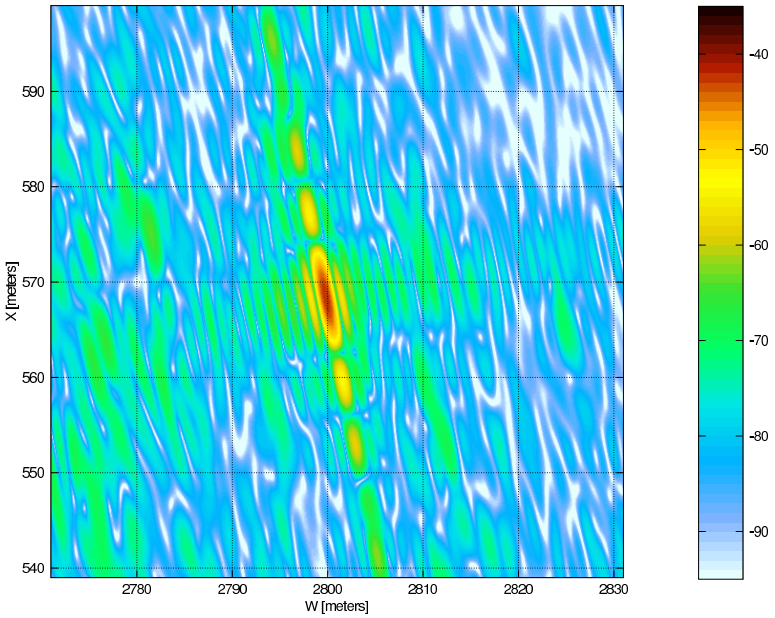


Figure 10.2.10: SAR magnitude image at reflector 1 after autofocus processing.

sinc-function as is expected if the PEF is zero.

As a part of this work we have made a SAR simulator which is briefly described in appendix E. Here we want to compare the processed autofocus compensated SAR image with the similar image processed from simulated data. Very equal images are a strong indication of an accurate estimate of the PEF.

Figure 10.2.11 shows the SAR magnitude image of a point scatterer processed from the simulator output. The point scatterer has the same magnitude and are defined to be in the same position as reflector 1. The simulated PEF is zero.

The reflector responses are very similar. The distance between the first zeros in both range and azimuth are very similar, so are the magnitudes of the first and second side-lobes. The main difference is the reflectivity of the natural scatterers in the real SAR image that partly mask the far out weak side-lobes of the reflector response. Based on the similarity we conclude that the SMAA has estimated the PEF fairly accurately.

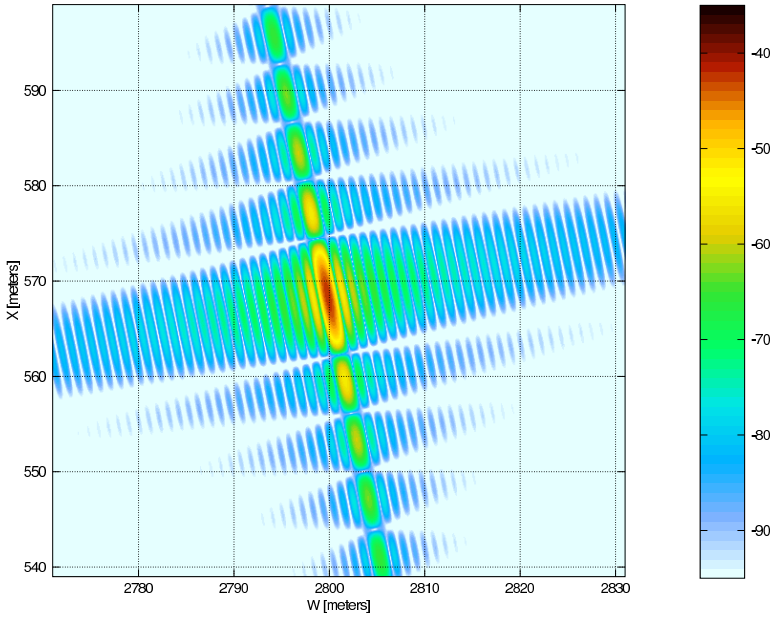


Figure 10.2.11: SAR magnitude image processed from simulated data.

## 10.3 Interferometric range

### 10.3.1 Interferometric range with atmospheric compensation

Appendix B gives a general introduction to the atmospheric influence on the propagation time. In section B.2 the sensitivity with respect to temperature, pressure and the partial pressure of water vapour is stated. The magnitude of these sensitivities shows that changes in the state of the atmosphere must somehow be compensated to achieve an acceptable accuracy level. In this section we construct a model of the atmosphere from meteorological measurements. The model is used to calculate the propagation speeds applied in the SAR processing.

#### 10.3.1.1 Estimation of the refractivity

The Norwegian Meteorological Institute has a high number of measurement stations spread out through Norway. The locations of the two stations closest to our radar range are shown with blue circles in figure 10.3.1. The altitude of the weather station at Blindern (south-most) is -8 meters relative the radar. Both temperature, pressure and relative humidity is measured at this station. The station at Tryvannshøgda (north-most) has an altitude of +412 meters relative the

radar. At this station only temperature is measured. These state variables are measured each whole hour.

Figure 10.3.2 shows the measured meteorological state-variables. The refractivity $N$ is a function of temperature $T$, pressure $P$ and partial water vapour pressure $P_w$ as given in equation B.1.6. We have assumed that all these state variables are a function of height $h$ only. First the temperature $T(h)$ was modelled as a linear function (constant gradient) using the measured temperatures at the two stations, see equation B.3.2. The pressure function $P(h)$ was then estimated by the barometric formula, equation B.3.3. During the measurement period there were no condensation in the altitude interval of interest. We have therefore assumed that the mole-fraction of water molecules were constant with height. The partial water vapour pressure function $P_w(h)$ could then be calculated by

$$P_w(h) = P(h)\frac{P_{wB}}{P_B} \tag{10.3.1}$$

Here $P_B$ and $P_{wB}$ are the total pressure and partial water vapour pressure at Blindern, respectively. $P_{wB}$ is calculated from the measured relative humidity $R_{hB}$ using Clausius-Clapeyron's relation, see equation B.1.7. By usage of equation B.1.6 $N(h)$ can now be calculated.

As can be seen from equation B.1.4 the increase in propagation time is given by the integral of $N$ along the propagation path. Since $N$ is only a function of height $h$ in our model, it is sufficient to calculate the average refractivity $\bar{N}$ for the propagation height interval. There is therefore a small difference in $\bar{N}$ between reflector 1 and 2. This is shown in figure 10.3.3.

The red dots show the times for the meteorological observations, while the green and blue circles show the times for the radar measurements. The temporal interpolation is done using piecewise cubic Hermite interpolating polynomials [46]. The derivatives are continues but the functions are still close to linear interpolation.

As expected $\bar{N}_1 < \bar{N}_2$ because the propagation speed increases with altitude. The curves have very similar shape since the distance between the paths is small relative to the typical correlation distance for the meteorological state variables. The time-average refractivities for reflector 1 and 2 are 317.1 and 318.6, respectively. It is instructive to relate the increase in propagation time to an equivalent increase in range $\Delta R$ if $\bar{N} = 0$. By usage of equation B.1.4 we have

$$\Delta R = \frac{c_0}{2}\Delta t_d = 10^{-6}\int_0^{s_{scatter}} N(r(\vec{s}))\,ds = 10^{-6}\bar{N}R \tag{10.3.2}$$

Inserting $R_1 = 2858$ and $R_2 = 2385$ meters, we get $\Delta R_1 = 0.906$ and $\Delta R_2 = 0.760$ meters. The impact of the atmosphere is order of magnitudes higher than the movements of the target area we hope to monitor. If the atmospheric state variables were constants this would be of no concern, but even small uncompensated changes in the refractivity imposes large errors. Just for comparison, the similar equivalent range increase for satellite SAR $\Delta R_{satellite} \approx 2.3$ meters [36]. Notice that the calculation of the average refractivity for a given radar measurement is both a spatial model based interpolation between the meteorological stations and


Figure 10.3.1: Meteorological stations and radar propagation path.

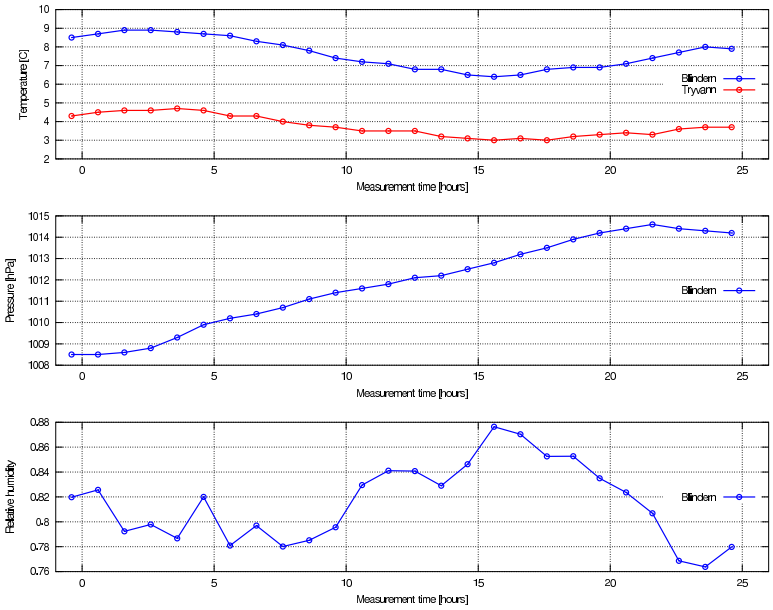


Figure 10.3.2: Measured meteorological state variables.

a temporal interpolation between the meteorological measurement times.

#### 10.3.1.2 Interferometric range

Figure 10.3.4 shows the interferometric ranges of the two pixels in the SAR image at the maximum magnitude of the reflector responses where we have assumed constant propagation speed $c_0$ in the SAR processing. The standard deviations for reflector 1 and 2 are 2.70 and 2.47 milli-meters, respectively. Figure 10.3.5 shows the same interferometric ranges where the refractive calculated in figure 10.3.3 have been applied in the SAR processing. In this case the standard deviations for reflector 1 and 2 are 1.94 and 1.67 milli-meters, respectively.

First notice that the curve legends says the range to the pixels of the maximum reflector responses are shorter in figure 10.3.5. The differences are $\Delta R_1 = 2857.92 - 2857.06 = 0.86$ and $\Delta R_2 = 2385.22 - 2384.57 = 0.65$ meters. These values are close but not exactly equal to the values calculated in section 10.3.2.2. The difference is because the positions used in figure 10.3.4 and 10.3.5 are restricted to be on the position grid of the SAR image.

Since we assume that the reflectors are not moving and other error sources are marginal, the curves in figure 10.3.5 should ideally be constant functions with standard deviation equal to zero. Compared to figure 10.3.4 the standard deviation is smaller but it is only reduced by approximately 30 %. And the variation still

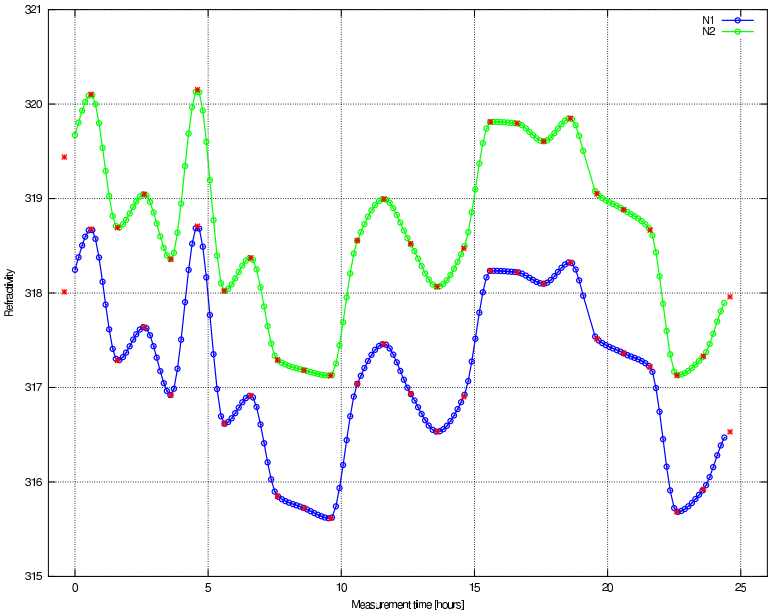


Figure 10.3.3: The average refractivity of the propagation path to the two reflectors.

spans 8 milli-meters.

#### 10.3.1.3 Discussion

Our main explanation of these discouraging results are inaccurate meteorological data. We have assumed that the temperature is a function of height only. The part of the propagation path closest to the radar passes above urban areas where the air may be slightly artificially heated giving raise to horizontal gradients. We have also assumed a linear temperature gradient. While this is what is normally observed in the troposphere, deviations occur. In the calculation of the linear temperature profile we used the station at Tryvannshøgda as the measurement at high altitude. Ideally the measurement should not be taken at ground level but elevated in free air. Ground outwards black-body radiation at night time can cool the air close to the ground more than elevated air at the same altitude but at a different horizontal position.

Since the meteorological observations are only done with one hour intervals, temporal interpolation was necessary. When studying the meteorological data in figure 10.3.2 the lack of smoothness particularly in the relative humidity but also to some extent in the temperature indicates that there can be significant interpolation errors. Errors in the temperature will not only give errors in the

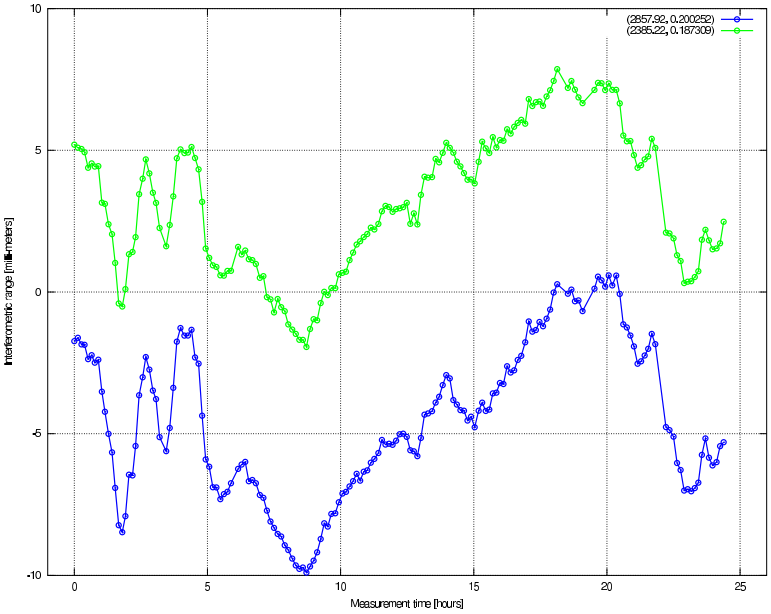


Figure 10.3.4: Interferometric range to the reflector positions, constant propagation speed.

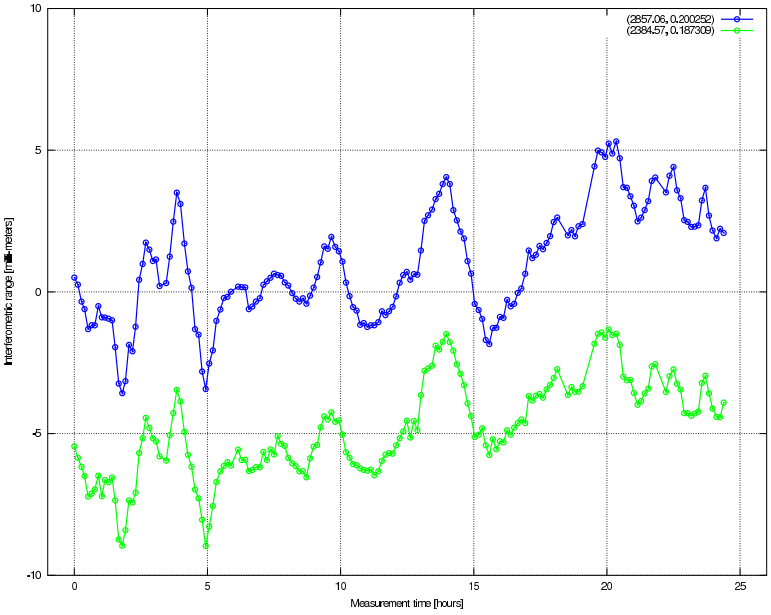


Figure 10.3.5: Interferometric range to the reflector positions, estimated propagation speed.

refractivity estimate by itself, is it also used in the calculation of the pressure profile which again is used to calculate the partial water vapour pressure.

To properly compensate for the errors induced by the changes in the atmosphere, much more accurate meteorological measurements are needed. We recommend to use two measurement stations, one located close to the radar and one inside the target area. These stations should both measure temperature, pressure and relative humidity. And they should be programmed to take a new measurement at the same time as each radar measurement is conducted.

### 10.3.2 Interferometric range using a reflector as reference

If there is a persistent scatterer or reflector illuminated by the radar which has a known position, the interferometric range of this reflector can be used as a reference. The change in range to all other scatterers are taken to be relative to the reference. The position of the reference do not have to be static, it only needs to be known. A practical arrangement may be that the position of the reference is measured accurately by other means such as with optical surveying or with a geodetic GPS receiver.

In this arrangement there are only differential errors. All error sources that are common to all scatterers such as zero order phase errors will cancel out. The only remaining error sources are electronic measurement noise and the propagation speed difference between the paths to different scatterers. Since the propagation paths to the reference and to other scatterers are close, the propagation speed error is generally small.

#### 10.3.2.1 Direct subtraction

By using reflector 2 as a reference the range to reflector 1 has been plotted in figure 10.3.6. This is equal to the difference between the two curves in figure 10.3.4. The standard deviation is 0.64 milli-meters which is a reduction to less than the half of what we achieved in section 10.3.1.2.

#### 10.3.2.2 Calculation of refractivity

If we assume that the main source for the variations in interferometric range is changes in the refractivity, a simple subtraction will only compensate for the propagation delay to the reference reflector. All scatterers located at different ranges will be compensated by the same amount. In this section we will assume that the refractivity is spatially constant in the volume between the radar and the whole target area. The temporal variations in the refractivity is calculated from the changes in the range to the reference reflector. In this way the compensation applied to some scatterer depends on the scattering range. Figure 10.3.7 shows the range to reflector 1 when using reflector 2 as the source for calculating the refractivity.

The standard deviation is 0.71 milli-metres which surprisingly is 0.07 millimeters higher than what we achieved in section 10.3.2.1. The difference is small

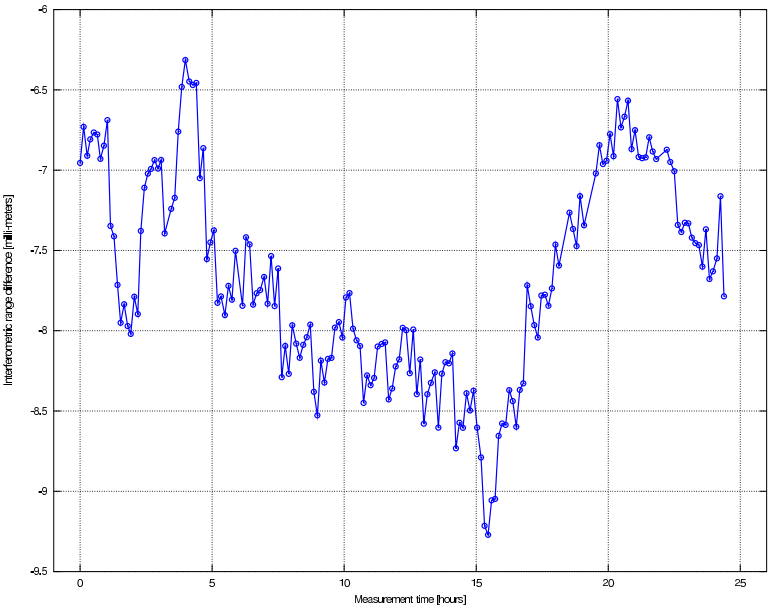


Figure 10.3.6: Difference in interferometric range between reflector 1 and 2.

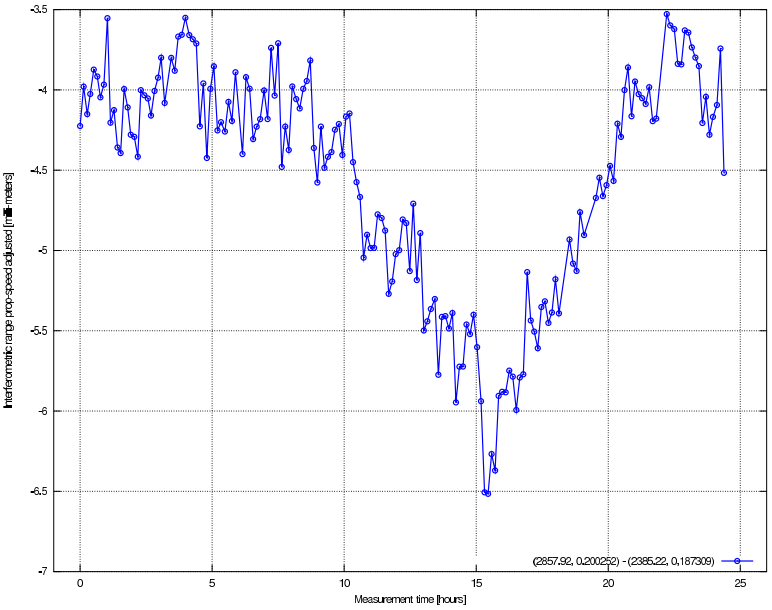


Figure 10.3.7: Propagation speed adjusted interferometric range to reflector 1.

but still a step in the wrong direction. We believe our assumption of constant refractivity in the volume between the radar and the whole target area to some extent is wrong. The variations in temporal refractivities can be calculated if we assume constant interferometric ranges to the reflectors.

$$\tilde{N}_i = 10^6(R_i/\bar{R}_i - 1) \tag{10.3.3}$$

$i$ is the reflector index ($i \epsilon \{1, 2\}$) and $\bar{R}_i$ is the average range. The curves are shown in figure 10.3.8.

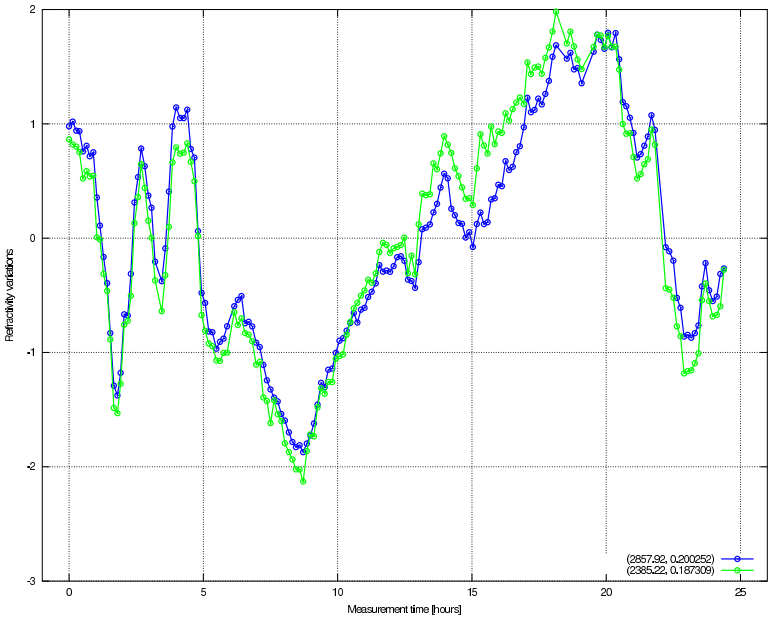


Figure 10.3.8: Calculated refractivities when assuming constant interferometric ranges.

By the nature of equation 10.3.3 the average of both curves are zero and the shape of the curves are equal to the interferometric ranges shown in figure 10.3.4. The difference between the curves which should ideally by zero, reflects the propagation speed adjusted interferometric range of reflector 1 shown in figure 10.3.7. Based on the theory given in appendix B the refractivity is a function of altitude where the altitude dependency changes with time. Hence, such variations as shown between two reflectors located at different altitudes must be expected.

If there are more than two persistent scatterers in the target area, a possible extension is to calculate the refractivity as a (possibly weighted) average of all these scatterers [83]. The variation in interferometric range due to changes in

the propagation speed should be proportional to scatterer range when assuming a homogeneous atmosphere. The refractivity can then be estimated as the constant of proportionality. It is not necessary to make the assumption that any scatterer has a known or a static fixed position. But in that case the component of the actual scatterer movement which is proportional to the range will wrongly be interpreted as changes in the propagation speed and subsequently removed.

#### 10.3.2.3 Discussion

Calculation of the refractivity from reference reflectors and scatterers has the potential to remove most error sources in interferometric range measurements. In particular most of the error introduced by changes in the atmosphere is removed. When using one reflector as a reference, the standard deviation in the interferometric range to the second reflector was less than 1 milli-meter. By averaging through many weeks the accuracy of the interferometric range estimates should be even better since the state of the atmosphere show little correlation during such long periods.

The main drawback with using reference reflectors is that in practice it is often difficult to find scatterer or reflector positions that are both in known static positions and also illuminated by the radar. Measuring the reference by other means is possible but makes the monitoring task more extensive.

# Chapter 11

# Conclusions

Through this work a complete functional ground interferometric SAR called GinSAR has been designed and constructed including electronics, mechanics and operational software. Since this has been a substantial part of the work, the design is described relatively detailed. We conclude that it is possible to make a functional ground SAR using only modest priced commercially available components.

To test the performance of the electronics we replaced the antennas with a long cable connecting the transmitter directly to the receiver. In this configuration there were no free radiation giving a much more controlled environment. After having filtered out unforeseen cable temperature expansion effects, the noise figure of the receiver was measured to be 5.5.

The radar has been developed in two versions. The first version with two vertically aligned receiver antennas was designed to (i) test the real aperture radar (signal budget, design and construction) on long range typically encountered at sites where there are unstable slopes (ii) test basic SAR processing algorithms (iii) test the capability of the radar to do repeat pass interferometry and thereby measure interferometric range (iv) test the generation of a digital elevation model by interferometric processing between the two receivers.

Our measurements has proved the functionality of the real aperture radar and the software for basic SAR processing implemented in the time domain. Because the length of the synthetic aperture was less than 3 meters, the horizontal cross-range resolution was poor. The repeat pass interferometry results proved the capability of the radar to monitor milli-meter movements. Our results also showed that variations in the propagation speed because of changes in the state of the atmosphere, are a dominating error source. The efforts to generate a digital elevation model were mostly discouraging. The measured altitude of placed out reflectors were fairly correct, but the estimated terrain resembled the actual terrain poorly. We believe better results should be achievable with higher horizontal cross-range resolution. Practically, the size of the three vertically aligned antennas were demanding to handle. The structure was also vulnerable to wind generated vibrations.

The development of a suitable autofocus algorithm for a ground SAR using

time domain SAR processing has been one of the main achievements of this work. Existing algorithms have been described and evaluated with respect to our application. The scatterer modelling autofocus algorithm was originally defined to be used with frequency domain SAR processing. We have used the basic ideas behind the scatterer modelling autofocus algorithm as a starting point for developing an algorithm suitable for ground SARs using time domain processing.

Our algorithm requires that the SAR image points are laid out on a polar grid. This makes an efficient implementation possible since the impulse response may then be pre-calculated. It is shown how the so called aperture domain can be used to estimate the phase error function for general SAR geometries. To improve the robustness in identifying scatterers, a threshold function is introduced. By extending the identification and impulse response subtraction to two dimensions, the numbers of false scatterer estimations are reduced. The combination of the phase error function estimates from different range-arcs uses concepts from robust statistics.

The developed algorithm has been evaluated by many simulated examples. We conclude that it is robust in the sense of being capable of estimating the true phase error function with small errors. The algorithm has also been used in the processing of actual measurements. The resulting reflector impulse response resembles the theoretical ideal impulse response very well. We believe our autofocus algorithm is capable of estimating the phase error function very accurately and therefore well suited for freely moving ground SARs.

In the second and final version the radar was mounted on a wagon that rolled on rails. In addition to test the autofocus algorithm, the main purpose was to determine the accuracy of interferometric range movements measurements. Totally 175 measurements were conducted during approximately 24 hours. The measurement results show that changes in the propagation speed due to changes in the atmosphere is the main error source for the interferometric ground SAR. Our efforts to compensate by using available meteorological data in a model of the atmosphere were only partly successful. We believe this procedure can be successful if the measurements are taken closer to the radar propagation path and at the same time as when the radar measurements are conducted.

If there is a reflector in the target area in a static or known position, relating all interferometric range measurements to this reflector has the potential of providing very accurate measurements. When we process our measurement data using one reflector as a reference, the standard deviation of the range error to the other reflector is less than 1 milli-meter. And even this small error can be explained by inhomogeneities in the atmosphere. The main drawback is the practical problem of finding or establishing a reference reflector in a static or known position.

In general, the movement of unstable rock-slopes are normally very slowly changing processes. It is therefore possible to reduce the magnitude of the errors introduced by changes in the state of the atmosphere by averaging measurements over periods of weeks and months.

Our main conclusion is that we have build a functional ground SAR with improved horizontal cross-range resolution suitable for monitoring slowly moving surfaces. The freely moving radar requires autofocus as a part of the SAR processing. We have therefore developed an accurate autofocus algorithm suitable for a ground SAR with time domain SAR processing. Measurements prove that the radar can measure surface movements with milli-meter accuracy.

# Appendix A

# Phase error as a function of signal to noise ratio

In this appendix the functional relationship between the standard deviation of the phase error estimate $\sigma_{\hat{\theta}}$ and the signal-to-noise-ratio (SNR) is derived.

The model of the received sampled signal is given by

$$\hat{s}(n\Delta t) = s(n\Delta t) + \nu(n\Delta t) \tag{A.0.1}$$

Here $s(n\Delta t)$ is the undisturbed signal

$$s(n\Delta t) = A\cos(2\pi f n\Delta t + \theta) \tag{A.0.2}$$

where $A$ is the magnitude, $\theta$ is the phase we want to estimate and $n\,\epsilon\,[1,\,N]$. $\nu(n\Delta t)$ is additive white unbiased Gaussian distributed noise with variance $\sigma_\nu^2$. It is assumed that $\Delta t < 1/(2f)$ and that $N\Delta t \gg 1/f$. It is also assumed that $\sigma_\nu < A$.

The maximum likelihood estimate of $\theta$ is given by [38]

$$\hat{\theta} = \arctan \frac{\sum_{n=1}^{N} \hat{s}(n\Delta t)\sin(2\pi f n\Delta t)}{\sum_{n=1}^{N} \hat{s}(n\Delta t)\cos(2\pi f n\Delta t)} \tag{A.0.3}$$

With out loss of generality we will assume $\theta = 0$ such that $\mathrm{E}[\hat{\theta}] = 0$ and $\sigma_{\hat{\theta}}^2 = \mathrm{var}(\hat{\theta}) = \mathrm{E}[\hat{\theta}^2]$.

Inserting equation A.0.1 and A.0.2 into the nominator of the arc-tangent expression in equation A.0.3 gives

$$\begin{aligned}\sum_{n=1}^{N}\hat{s}(n\Delta t)\sin(2\pi fn\Delta t) &= \sum_{n=1}^{N}(A\cos(2\pi fn\Delta t)\sin(2\pi fn\Delta t)+ \\ &\quad \nu(n\Delta t)\sin(2\pi fn\Delta t)) \\ &\approx \sum_{n=1}^{N}\nu(n\Delta t)\sin(2\pi fn\Delta t) \end{aligned} \tag{A.0.4}$$

where it has been approximated that the first sum term is close to zero since sine and cosine are orthogonal functions. Inserting equation A.0.1 into the denominator of the arc-tangent expression in equation A.0.3 gives

$$\begin{aligned}\sum_{n=1}^{N}\hat{s}(n\Delta t)\cos(2\pi fn\Delta t) &= \sum_{n=1}^{N}(A\cos^2(2\pi fn\Delta t)+ \\ &\quad \nu(n\Delta t)\cos(2\pi fn\Delta t)) \\ &\approx \sum_{n=1}^{N}A\cos^2(2\pi f\Delta t) \\ &\approx \frac{NA}{2} \end{aligned} \tag{A.0.5}$$

where it has been approximated that the second sum term (the noise) is much smaller than the first (sum of the cosine-squares).

Inserting A.0.4 and A.0.5 into equation A.0.3 and approximating $\arctan x = x$ since $\sigma_\nu < A$ gives

$$\hat{\theta} = \frac{2}{NA}\sum_{n=1}^{N}\nu(n\Delta t)\sin(2\pi fn\Delta t) \tag{A.0.6}$$

The variance of $\hat{\theta}$ can now be calculated

$$\begin{aligned}\sigma_{\hat{\theta}}^2 &= \sum_{n=1}^{N}\mathrm{var}(\frac{2}{NA}\nu(n\Delta t)\sin(2\pi fn\Delta t)) \\ &= \left(\frac{2}{NA}\right)^2\sigma_\nu^2\sum_{n=1}^{N}\sin^2(2\pi fn\Delta t) \\ &= \left(\frac{2}{NA}\right)^2\sigma_\nu^2\frac{N}{2} \\ &= \frac{2}{NA^2}\sigma_\nu^2 \end{aligned} \tag{A.0.7}$$

The average power $P_s$ of the undisturbed signal $s(n\Delta t)$ is related to the magnitude $A$ by

$$A = \sqrt{2P_s} \tag{A.0.8}$$

Inserting equation A.0.8 into A.0.7 and taking the square-root gives the final result

$$\sigma_{\hat{\theta}} = \frac{1}{\sqrt{\frac{P_s}{\sigma_\nu^2}}} = \frac{1}{\sqrt{\text{SNR}}} \tag{A.0.9}$$

In the literature the phase error to SNR relationship is often stated as [90]

$$\sigma_{\hat{\theta}} = \frac{1}{\sqrt{2\ \text{SNR}}} \tag{A.0.10}$$

That result is does not apply in this text since it is derived under the following signal assumption

$$\hat{s}_C(n\Delta t) = A\exp(2\pi f n\Delta t + \theta) + \nu_C(n\Delta t) \tag{A.0.11}$$

Here the $\nu_C$ noise is complex

$$\nu_C(n\Delta t) = v_I(n\Delta t) + jv_Q(n\Delta t) \tag{A.0.12}$$

where $\nu_I$ and $\nu_Q$ are identical independent distributed variables with variance

$$\sigma_{\nu_I}^2 = \sigma_{\nu_Q}^2 = \frac{\sigma_{\nu_C}{}^{\mathbf{2}}}{2} \tag{A.0.13}$$

# Appendix B

# Atmospheric influence on propagation time

## B.1 Theory

In the most general case the two way propagation time from the radar to a point scatterer and back is given by

$$t_d = 2\int_0^{s_{\text{scatter}}} \frac{ds}{c(\vec{r}(s))} \tag{B.1.1}$$

Here $s$ is the distance along the propagation path from the radar to the scatterer, $\vec{r}(s)$ is a position vector that traces out the propagation path as a function of $s$ and $c(\vec{r}(s))$ is the propagation speed in the position $\vec{r}(s)$. In vacuum the propagation speed is a constant $c_0$, and the propagation path becomes a straight line. Then the propagation time simply becomes $t_{d0} = 2s_{\text{scatter}}/c_0$. Because the propagation speed in the atmosphere is slower than in vacuum ($c(\vec{r}(s)) \leq c_0$), the increase in propagation time becomes

$$\Delta t_d = t_d - t_{d0} = 2\int_0^{s_{\text{scatter}}} (\frac{1}{c(\vec{r}(s))} - \frac{1}{c_0})\, ds \tag{B.1.2}$$

The refractivity of the atmosphere is defined as the relative reduction of the propagation speed, scaled by $10^6$

$$N = 10^6(\frac{c_0}{c} - 1) \tag{B.1.3}$$

When this expression is inserted into equation B.1.2, the propagation time increase becomes

$$\Delta t_d = 2\frac{10^{-6}}{c_0}\int_0^{s_{\text{scatter}}} N(\vec{r}(s))\, ds \tag{B.1.4}$$

To fully compensate for the increase in propagation time, $N(\vec{r}(s))$ must there-

fore be known all along the propagation path. Errors in the estimate of the refractivity leads to errors in the calculated range $R$ since

$$R = \frac{c_0}{2} t_{d0} = \frac{c_0}{2} \left( t_d - \Delta t_d \right) \tag{B.1.5}$$

The refractivity is a function of the state of the atmosphere and may be approximated by [22]

$$N = 77.6 \frac{P}{T} + 23.3 \frac{P_w}{T} + 3.75 \cdot 10^5 \frac{P_w}{T^2} \tag{B.1.6}$$

where $P$ is the total pressure in hecto-Pascal, $T$ is the temperature in Kelvin and $P_w$ is the partial pressure of water vapour in hecto-Pascal. The partial water vapour pressure $P_w$ can be calculated from the relative humidity $R_h$ by Clausius-Clapeyron's relation

$$P_w = R_h \, P_{w0} \exp \left[ \frac{L_v}{R_v} ( \frac{1}{T_0} - \frac{1}{T} ) \right] \tag{B.1.7}$$

where $T$ is the temperature in Kelvin, $T_0 = 273.16$ K, $P_{w0} = 6.11$ hPa is the water vapour saturation pressure when $T = T_0$, $L_v = 2.5 \cdot 10^6$ J/kg is the latent heat of water vaporisation and $R_v = 461.52$ J/kg K is the specific gas constant for water vapour. Equation B.1.6 is believed to be accurate to within 0.5 % for frequencies up to 30 GHz and normally encountered ranges of temperatures, pressure and humidity. Physically, the refractivity of the atmosphere is due to displacement of the electron cloud of the gaseous constituents and alignment of electrically and magnetically polar molecules with the propagating electric and magnetic fields.

If there is liquid droplets in the atmosphere (clouds, hail, rain, snow), the additional term $1.45 \cdot 10^3 M$ derived from Clausius-Mossotti's relation must be added on the right side of equation B.1.6 where $M$ is the mass content of cloud and rain water per volume of air in kg/m$^3$ [91]. The added refractivity of droplets are due to displacement of charge inside the particles which generates secondary radiation, also known as forward scattering. Since the size of the liquid droplets are normally much smaller than the wavelength, Rayleigh scattering theory can be used calculate the scattering magnitude.

The additional term becomes inaccurate if the liquid is present as large wet snowflakes with sizes in the same order of magnitude as the wavelength. In this case the Mie solution to Maxwell's theory is needed to calculate the scattering magnitude. If there is frozen snow instead of liquid water in the atmosphere, Clausius-Mossotti's relation gives the term $0.86 \cdot 10^3 M$ due to the lower dielectric constant of ice compared to water.

## B.2 Sensitivity

If a homogeneous media is assumed, the partial derivatives of $R$ with respect to $T$, $P$, and $P_w$ can be calculated. Inserting the values $T = 277$ K, $P = 970$ hPa

and $P_w = 6.43$ hPa, we get

$$\frac{dR}{dP} = -0.28 \text{ mm/hPa km} \quad \text{(B.2.1)}$$

$$\frac{dR}{dT} = 1.1 \text{ mm/K km} \quad \text{(B.2.2)}$$

$$\frac{dR}{dP_w} = -5.0 \text{ mm/hPa km} \quad \text{(B.2.3)}$$

Very dens clouds have a mass content of $M = 2 \cdot 10^{-3}\text{kg/m}^3$. The change in range compared to the situation with no clouds/droplets are $\Delta R = -2.9$ mm/ km.

The magnitude of these sensitivities shows that changes in the state of the atmosphere will introduce large errors if not compensated.

## B.3 Compensation by measuring the state of the atmosphere

A possible compensating strategy is to apply a model of the atmosphere which describe functional relationships between the state variables $P$, $T$, $P_w$ and $M$ and altitude $h$. An accurate model will include reference values such as the pressure and temperature at sea-level ($P_0$ and $T_0$). Based on possibly several measurements of the state variables close to the propagation path $\vec{r}(s)$, the reference variables in the model can be determined. The state of the atmosphere as described by the model is then used to calculate $N(\vec{r}(s))$ using equations B.1.6 and B.1.7. Here follows a brief introduction to how models for $P$, $T$, $P_w$ and $M$ can be constructed. For a more extensive introduction to atmospheric modelling and general meteorology, see [5].

By assuming an ideal gas the so called barometric formula is derived [12]

$$P(h) = P_0 \, e^{-\int_0^h \frac{M_m g}{R_g} \frac{dh}{T(h)}} \quad \text{(B.3.1)}$$

where $M_m$ [kg/mol] is the molar mass for air, $g$ [m/s$^2$] is the gravitational acceleration and $R_g$ [J/(mol K)] is the ideal gas constant for air.

Within intervals of the troposphere the temperature is well modelled with a linear function

$$T(h) = T_0 + Lh \quad \text{(B.3.2)}$$

The temperature gradient $L$ is also called the *lapse rate*. Inserting equation B.3.2 into the integral in equation B.3.1 gives

$$P(h) = P_0 \left( \frac{T_0}{T_0 + Lh} \right)^{\frac{M_m g}{L R_g}} \quad \text{(B.3.3)}$$

$L$ is normally a negative number, the temperature falls with altitude since the

air is mainly warmed from the surface of the planet. The *international standard atmosphere* is defined by the aviation industry to have $L_{ISA} = -0.0065$ K/m which is an average value. The actual value of $L$ at some position and at a given time may differ substantially. If we have unsaturated air and assume adiabatic conditions the *dry adiabatic lapse rate* can be calculated to be $L_{DALR} = -0.0098$ K/m. The adiabatic assumption is fair since air has low thermal conductivity and the bodies involved are very large. If the air is saturated, the temperature is at the dew point temperature, relative humidity is 100 %, then the *saturated adiabatic lapse rate* applies. This lapse rate varies strongly with temperature but the absolute value is always far less than $L_{DALR}$, a typical value is $L_{SALR} = -0.005$ K/km. In absolute values, $L_{SALR}$ is smaller because latent heat is released when water condenses, thus decreasing the rate of temperature drop as altitude increases.

As unsaturated air rises, its temperature drops at the dry adiabatic lapse rate. The dew point also drops (as a result of decreasing air pressure) but much more slowly, typically about $-0.002$ K/km. If unsaturated air rises far enough, eventually its temperature will reach its dew point, and condensation will begin to form. The air subsequently cools at the slower saturated adiabatic lapse rate if the altitude increases further.

Given measurements of $T$, $P$ and $R_h$ at two different altitudes, it is possible to calculate vertical profiles of these variables and determine if condensation occurs within the altitude interval. If yes, the interval is split into two parts where $T$,$P$ and $P_w$ profiles are calculated for both. If the calculations indicate no condensation, single profiles can be calculated.

If $T$, $P$ and $R_h$ is only measured at one altitude we may assume $L = L_{ISA}$ and uniform mole fraction of vapour in the air. Even in this case we may conclude that condensation occurs if the temperature becomes less than the dew point temperature and choose to spilt the interval into two. But the profile estimates will in general be less accurate.

In the case where calculations show that there is condensation between the radar and the target area, an estimate of the water mass content function $M(\vec{r}(s))$ must be formed in addition to $T$, $P$ and $P_w$. This is a difficult task since $M$ may have large local variations along the path $s$. This is often the case in mountain regions where the elevation of air is driven by wind.

### B.3.1 Propagation path

An exact calculation of the increase in propagation time given by equation B.1.4 requires that the propagation path is known. When the propagation media is inhomogeneous, when the refractivity of the atmosphere $N(\vec{r}(s))$ has gradients, then the propagation path will in general not be a straight line. In this subsection we will investigate if the error introduced by assuming a straight path is significant.

We will assume that the wavelength is very small compared to the size of the inhomogeneities in the atmosphere such that the wave propagation is well approximated by geometric (ray) optics. Fermat's principle says that a light ray, in going between two points, must traverse an optical path length which is stationary

with respect to variations of the path. In practice the optical path length is almost always the minimum path length. The optical path length is defined as a functional

$$L = \int_{p_0}^{p_1} \frac{c_0}{c(\vec{r}(s))} ds \tag{B.3.4}$$

The minimum of a functional like this can be found by calculus of variations leading to Euler's equation (in this context also often called the *ray-path equation*)

$$\frac{d}{ds}\left(\frac{c_0}{c(\vec{r}(s))}\frac{d\vec{r}(s)}{ds}\right) - \nabla\frac{c_0}{c(\vec{r}(s))} = 0 \tag{B.3.5}$$

In most cases the propagation speed is only a function of height. Using $x$ and $z$ for the horizontal and vertical axis, respectively, the components of equation B.3.5 becomes

$$\frac{d}{ds}\left(\frac{c_0}{c(z)}\frac{dz(s)}{ds}\right) - \frac{d}{ds}\left(\frac{c_0}{c(z)}\right) = 0 \tag{B.3.6}$$

$$\frac{c_0}{c(z)}\frac{dx(s)}{ds} = \text{constant} \tag{B.3.7}$$

If we use $\theta(s)$ to denote the inclination angle of the ray we have, then $dz(s)/ds = \sin\theta(s)$ and $dx(s)/ds = \cos\theta(s)$. Inserting into equation B.3.7 gives Snell's law in a generalised form

$$\frac{c_0}{c(z)}\cos\theta(s) = \text{constant} \tag{B.3.8}$$

Inserting into B.3.6 and rearranging gives

$$\frac{d\theta(s)}{ds} = -\frac{\cos\theta(s)}{c(z)} \cdot \frac{dc(z)}{dz} \tag{B.3.9}$$

Notice that the first factor on the right side by means of equation B.3.8 is a constant. Equation B.3.9 can therefore be integrated to find $\theta(s)$ given some initial inclination angel $\theta(0)$ and a propagation speed profile $c(z)$. By usage of $dz(s)/ds = \sin\theta(s)$ and $dx(s)/ds = \cos\theta(s)$ the spatial coordinates of the ray $x$ and $z$ can be found. Alternatively the following integral can be solved

$$x(z) - x(z_0) = \int_{z_0}^{z} \frac{dz}{\tan\theta(s)} = \int_{z_0}^{z} \frac{dz}{\sqrt{\left(\frac{c(z_0)}{c(z)\cos\theta(z_0)}\right)^2 - 1}} \tag{B.3.10}$$

The propagation time between the start- and end-points can be calculated by

$$\tau(z) - \tau(z_0) = \int_{z_0}^{z} \frac{dz}{c(z)\sin\theta(s)} = \int_{z_0}^{z} \frac{dz}{c(z)\sqrt{1 - \left(\frac{c(z)}{c(z_0)}\cos\theta(z_0)\right)^2}} \tag{B.3.11}$$

We will use equation B.3.11 to calculate the true propagation time and compare with the propagation time found by assuming a straight propagation path for a situation typical for GinSAR. We have used $x(z_0) = 0$, $x(z) = 2786.17$, $z_0 = 105$, $z = 412$ (all numbers are in meters), $\theta(z_0) = 109.751$ milli-rad. $c(z) = c_0/(N(z) \cdot 10^{-6}+1)$ where the refractivity function $N(z) = N(z_0)\exp(-0.01439 \cdot 10^{-3}(z-z_0))$ is taken from [10], p. 304. The difference in propagation time becomes less than $0.1 \cdot 10^{-15}$ seconds. We therefore conclude that the error introduced by using a straight propagation path is insignificant.

# Appendix C

# Tomographic formulation of SAR imaging

It is possible to interpret SAR processing as a tomographic reconstruction problem. This appendix will give a brief introduction where we try to convey the main ideas. We will emphasis the necessary approximations as they are of special interest to many autofocus algorithms. A thorough description of tomographic SAR imaging can be found in the original paper [72] and in [43].

The imaging geometry is shown in figure C.0.1. The radar is shown as a red dot that moves along the x-axis from $-L$ to $+L$. The target area is assumed to the shaded circle, it is located a distance $R_c$ from the centre point of the synthetic aperture and has radius $R_0$. The reflectivity of the target area is given by $\rho(x,\, w)$, this is the function we seek to reconstruct. The figure shows a short transmitted pulse as a green arc denoted $l$ with arrows indicating the outward propagation.

As the transmitted pulse propagates through the target area, the reflections back to the radar at one instant of time will be the reflectivity function integrated along the arc $l$. The integral will be called the integrated reflectivity

$$\gamma(r(t)) = \int_l \rho(x,\, w)\, dl \tag{C.0.1}$$

In the following it is assumed that the target area radius $R_0$ is small relative to the target area centre range $R_c$. The arc $l$ can then be approximated with a straight line.

It is also assumed that the transmitted signal is a frequency sweep (chirp-pulse)

$$s_{TX}(t) = \exp_{\jmath}\left((\omega+\beta)t + \frac{1}{2}\alpha t^{\mathbf{2}}\right) \tag{C.0.2}$$

where $t\,\epsilon\,[0,\, T_p]$. The received signal will then be

$$s_{RX}(t) = \int_{-R_0}^{R_0} s_{TX}\left(t - \frac{2}{c}\left(R_c + \varepsilon(x) + r(t)\right)\right)\gamma\left(r(t)\right)\, dr \tag{C.0.3}$$

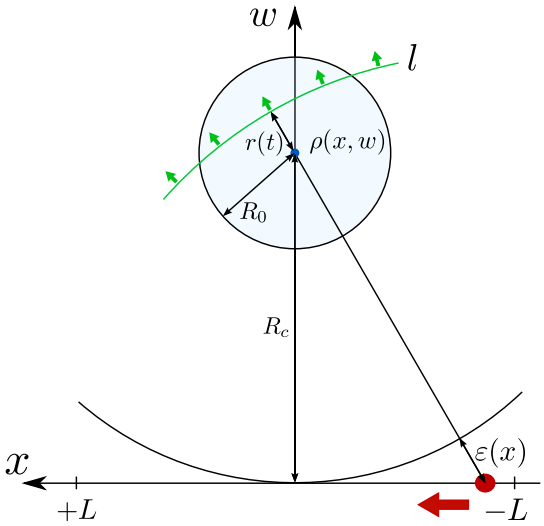


Figure C.0.1: Tomographic SAR imaging geometry.

where $t\,\epsilon\,[\frac{2}{c}(R_c+\varepsilon(x)-R_o,\ \frac{2}{c}(R_c+\varepsilon(x)+R_0)+T_p]$. Upon reception the received signal is de-ramped by multiplying with $s_{TX}(t-\frac{2}{c}(R_c+\varepsilon(x)))^*$. The product is given by

$$\tilde{s}_{DR}(t) = \int_{-R_0}^{R_0} \exp(\jmath E)\,\gamma(r)\,dr \tag{C.0.4}$$

where the $E$ in the exponent is

$$E = -(\omega+\beta)\frac{2}{c}r(t) + \frac{1}{2}\alpha\left(-\frac{4}{c}r(t)t + \frac{4}{c^2}\left(2r(t)\left(R_c+\varepsilon(x)\right)+r(t)^2\right)\right) \tag{C.0.5}$$

If this exponential $E$-expression is approximated by removing the last $r(t)^2$ term, the de-ramp product (equation C.0.4) can be written

$$\tilde{s}_{DR}(t) \approx s_{DR}(t) = \int_{-R_0}^{R_0} \exp\left(-\jmath k_r(t) r\right)\,\gamma(r)\,dr \tag{C.0.6}$$

where

$$k_r(t) = \frac{2}{c}\left((\omega+\beta)+\frac{2}{c}\alpha\left(R_c+\varepsilon(x)\right)-\alpha t\right) \tag{C.0.7}$$

Equation C.0.6 is recognised as the Fourier-transform of $\gamma(r)$ where $k_r(t)$ is the spatial frequency. The expression for $\gamma(r)$ given in equation C.0.1 is equal to the Fourier-transform of $\rho(x,\,w)$ along the $l$-line for zero-frequency. Hence,

$s_{DR}(t)$ traces out a line of the 2-dimensional Fourier-transform of $\rho(x,\, w)$ denoted $P(k_x,\, k_w)$ as $t$ varies. Uniform samples of $s_{DR}(t)$ will give uniform samples of $P(k_x,\, k_w)$ along a line which has the same angle relative to the $k_x$- and $k_w$-axis as the $r$-direction has to the $x$- and $w$-axis. This is shown in figure C.0.2.

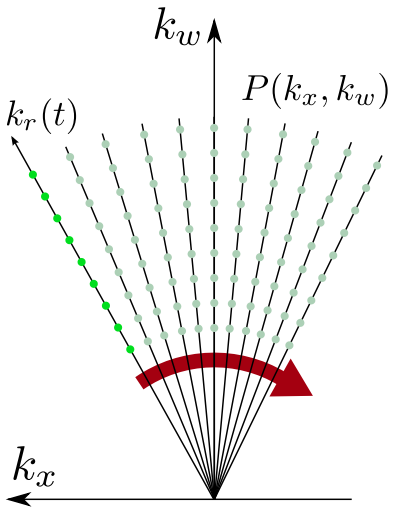


Figure C.0.2: Sample points of $P(k_x,\, k_w)$.

The samples are shown as green dots along the $k_r$-direction. As the radar moves to new positions on the synthetic aperture new lines of samples are traced out shown by grey dots. The red arrow corresponds to the movement on the synthetic aperture in figure C.0.1. The angle of these lines will change since the direction from the radar to the target area centre changes. After all measurements along the synthetic aperture has finished, the stored sample points of $P(k_x,\, k_w)$ are located on a fan. The radial frequency limits are found by inserting the time limits into equation C.0.7, the angular limits are given by the sampling geometry.

To reconstruct $\rho(x,\, w)$ we need to inverse Fourier-transform $P(k_x,\, k_w)$ in both dimensions. The FFT algorithm requires that the samples are located on an uniform rectangular grid. If $R_c \gg R_0$ the grid may be approximated to be rectangular. If this is not the case, the sample-points must be interpolated and re-sampled on a rectangular grid. The interpolation may be split into two sequential one-dimensional interpolations, see figure C.0.3.

The original points are in green. For each receiver position they are first interpolated to the blue points on the left part of the figure which have an uniform separation in the $k_w$-dimension. The blue points are then interpolated to the red

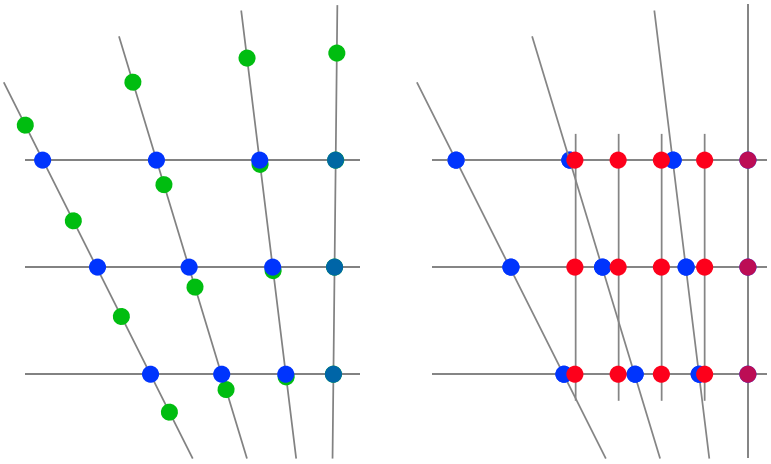

Figure C.0.3: Two sequential one-dimensional interpolations.

points in the $k_x$-dimension as shown on the right part of the figure. The rectangular grid of red points are finally inverse Fourier-transformed. The 2-dimensional inverse FFT is calculated as two 1-dimensional transforms, first in the range dimension and last in the cross-range.

After the last interpolation each red point is no longer associated with one single radar position. If $R_c \gg R_0$ we may still approximate it to be a one-to-one relationship. Since many autofocus algorithms assumes a one-to-one relationship they implicitly assume that $R_c \gg R_0$. The one-to-one approximation makes the last cross-range inverse FFT the first processing step where data from the different receiver positions are mixed.

Notice that if we only do interpolation (no extrapolation) the rectangular area covered by the interpolated points is smaller than the original covered area. This reduction in spectral support reduces the resolution of $\rho(x, w)$ but the relative reduction is small if $R_c \gg R_0$.

In the development of this tomographic reconstruction we have approximated the phase-front of the transmitted pulse to be a straight line and we have ignored the last term in the de-ramp product. These approximations both have the effect that for point scatterers not located in the centre of the target area, the de-ramp product at $(k_x, k_w)$ calculated by equation C.0.4 is only an approximation of the true $P(k_x, k_w)$. The error introduced by the approximations increase with scatterer distance from the centre of the target area.

With respect to the curvature two conditions must both be satisfied for the approximation to be valid. First the range error through the target area due to the curvature must be less than the range resolution. The requirement on the target area size $R_o$ becomes

| | GinSAR | Aircraft SAR | Satellite SAR |
|---|---|---|---|
| $\lambda$ [milli-meter] | 52 | 24 | 31 |
| $\alpha$ [Grad/s$^2$] | 57.2 | 16.8 | 3770 |
| $t_c$[milli-second] | 15.4 | 30.0 | 0.25 |
| $2L$ [meter] | 12 | 5000 | 12000 |
| $R_c$ [kilo-meter] | 2.9 | 15.2 | 594 |
| $R_{0\max1}$ [meter] | 78 | 238 | 1090 |
| $R_{0\max2}$ [meter] | 2037 | 130 | 4643 |
| $R_{0\max3}$ [meter] | $3720 \cdot 10^3$ | 8819 | 9370 |

Table C.0.1: Max target area radius.

$$R_{0\max1} \leq \sqrt{\frac{2\pi c R_c}{\alpha t_c}} \tag{C.0.8}$$

In the derivation of equation C.0.8 we have used $R_0^2/(2R_c)$ as a first order approximation of the range-difference between the straight line and the arc, and $\pi c/(\alpha t_c)$ as an expression for the range resolution. Second, the range error due to the curvature for any point scatterer must not change more than a small fraction of a wavelength as the radar moves along the synthetic aperture. The associated requirement on $R_0$ using a phase error limit of $\pi/4$ has been calculated in [43] - appendix B. When expressing $R_0$ as a function of $L$ we get

$$R_{0\max2} \leq \frac{R_c}{2L}\sqrt{\frac{R_c\lambda}{2}} \tag{C.0.9}$$

With respect to the ignored term in the de-ramp product, the requirement on $R_0$ using $\pi/4$ as a phase error limit has also been calculated in [43] - appendix B

$$R_{0\max3} \leq \frac{R_c c}{2L}\sqrt{\frac{\pi}{2\alpha}} \tag{C.0.10}$$

Table C.0.1 shows the $R_{0\max}$ requirements for GinSAR (rolling on rails), an aircraft carried SAR[1] and a the TerraSAR X satellite SAR.[2]

With respect to the change in range along the aperture due to the curvature ($R_{0\max2}$) and the ignored de-ramp term ($R_{0\max3}$) GinSAR may use tomographic formulated SAR processing without introducing significant errors. But the combination of high range resolution and short range seriously limits the size of the target area ($R_{0\max1}$). It is possible to circumvent the requirement given in equation C.0.8 by repeat the processing for several different target area centre positions and then merge the processed data. But the merge process can be difficult.

[1] The number are taken from [87] as an example of an aircraft carried SAR. There are, however, many aircraft carried SARs with a wide span in the system parameters giving different limits on $R_{0\max}$.

[2] Most of the parameters for the TerraSAR system are programmable. The stated parameters are chosen within the programmable limits. General information on the TerraSAR mission and system design can be found in [104]. More detailed information on the different signal formats can be found in [16].

# Appendix D

# Frequency domain matched filtering

This SAR processing algorithm is also known as the $\Omega - k$ algorithm. It has it roots in seismic processing which bears many similarities to SAR processing. In particular Stolt developed an accurate solution to the wave equation which included a step now called the Stolt-mapping or Stolt-interpolation [93]. Hellsten and Anderson were the first to use the $\Omega - k$ algorithm as described by Stolt for SAR processing [40]. Cafforio, Prati and Rocca recognized the seismic analogy and described SAR processing as migration of electro-magnetic waves [19]. We have chosen to use the name frequency domain matched filtering (FDMF) since this brief introduction uses the matched filter as a starting point. A more thorough description also following the matched filter approach can be found in [65].

The matched filter as described in [97] may be viewed as a correlation between the received signal and the complex conjugate of the same signal. Since the Fourier-transform of the correlation between to signals is equal to the product between the Fourier-transform of each signal, one complex conjugated, the matched filter may be implemented in the frequency domain. The procedure is to Fourier-transform both signals, complex conjugate the first, multiply the signals and finally inverse Fourier-transform the product.

It is straight forward to extend the matched filter to two dimensions as we have in SAR. If there is only one point scatterer at an unknown position in the target area, we would correlate the received signal with a simulated signal from a scatterer located in the centre of the target area. The position of the real scatterer will be at the correlation peak. Since the SAR processing is linear, all scatterers in the target area will be imaged in the same process.

The imaging geometry is shown in figure D.0.1. We will assume the transmitted signal is a frequency sweep (chirp-pulse)[1]

[1]The signal can actually be of any shape but we use a frequency sweep pulse since that is most common.

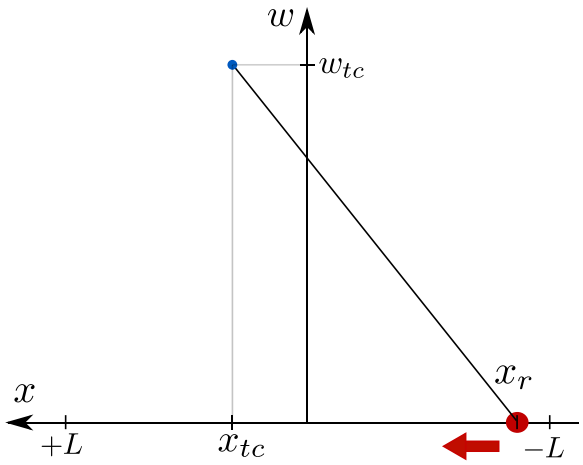


Figure D.0.1: Frequency domain matched filter geometry.

$$s_{TX}(t) = \exp \jmath \left( (\omega + \beta)t + \frac{1}{2}\alpha t^2 \right) \tag{D.0.1}$$

The received signal for some position $x_r$ on the synthetic aperture assuming a single unit point-scatterer at the centre of the target area $(x_{tc},\, w_{tc})$ becomes

$$s_{RX}(x_r,\, t) = s_{TX}\left( t - \frac{2}{c}\sqrt{w_{tc}^2 + (x_{tc} - x_r)^2} \right) \tag{D.0.2}$$

Here $x_r$ is the position of the radar along the $x$-axis. For simplicity we will assume that the target area consists of $n$ discrete scatterers with coordinates $(x_{tn},\, w_{tn})$. The actual received signal will be then the sum of all these scatterers

$$\hat{s}_{RX}(x_r,\, t) = \sum_n \rho(x_{tn},\, w_{tn}) s_{TX}\left( t - \frac{2}{c}\sqrt{w_{tn}^2 + (x_{tn} - x_r)^2} \right) \tag{D.0.3}$$

The Fourier-transform of equation D.0.2 in the time dimension is

$$S_{RX}(x_r,\, \omega) = S_{TX}(\omega) \exp -\jmath 2 \frac{\omega}{c}\sqrt{w_{tc}^2 + (x_{tc} - x_r)^2} \tag{D.0.4}$$

The expression for $S_{TX}(\omega)$ can be expressed analytically by the Fresnel integrals, see [39] section 2.1.2.2.2. In practice a numerical calculation using FFT is often used.

The Fourier-transform of equation D.0.4 in the $x_r$-dimension can be calculated using the principle of stationary phase (PSOP) [14]

$$S_{RX}(k_{xr},\,\omega) = S_{TX}(\omega)\frac{\exp -\jmath\frac{\pi}{4}}{\sqrt{4\left(\frac{\omega}{c}\right)^2 - k_{xr}^2}}\exp\left(-\jmath\sqrt{4\left(\frac{\omega}{c}\right)^2 - k_{xr}^2}w_{tc} - \jmath k_{xr}x_{tc}\right) \tag{D.0.5}$$

for $|k_{xr}| < 2\omega/c$ and zero otherwise. The Fourier-transform of the correlation product can now be calculated

$$C_p(k_{xr},\,\omega) = \hat{S}_{RX}(k_{xr},\,\omega)^* S_{RX}(k_{xr},\,\omega) \tag{D.0.6}$$

where $\hat{S}_{RX}(k_{xr},\,\omega)^*$ is the complex conjugate Fourier-transform of $\hat{s}_{RX}(x_r,\,t)$.

Since $C_p(k_{xr},\,\omega)$ in equation D.0.6 is a function of $k_{xr}$ and $\omega$, it cannot directly be inverse Fourier-transformed in both dimensions to find the positions of the scatterers.

To this end we will define a reflectivity function with only one single point scatterer

$$\rho(x,\,w) = \delta(x - x_t,\,w - w_t) \tag{D.0.7}$$

The Fourier-transform of $\rho(x,\,w)$ in both dimensions is

$$P(k_x,\,k_w) = \exp\left(-\jmath k_x x_t - \jmath k_w w_t\right) \tag{D.0.8}$$

When comparing the exponential in equation D.0.5 with equation D.0.8 they have the same form if we introduce the following mapping

$$k_x(\omega,\,k_{xr}) = k_{xr} \tag{D.0.9}$$

$$k_w(\omega,\,k_{xr}) = \sqrt{4\left(\frac{\omega}{c}\right)^2 - k_{xr}^2} \tag{D.0.10}$$

This is the Stolt-mapping coming from the change of variables. Since both $\omega$ and $k_{xr}$ is uniformly sampled, the sample spacing of $k_w$ will not be uniform. It is therefore required to interpolate $C_p(k_{xr},\,\omega)$ such that the resulting $C_p(k_x,\,k_w)$ is uniformly sampled in both $k_w$ and $k_x$. As described in [92] the Jacobian of the mapping from $\omega$ to $k_w$is given by

$$J(\omega) = \frac{4\frac{\omega}{c^2}}{\sqrt{4\left(\frac{\omega}{c}\right)^2 - k_{xr}^2}} \tag{D.0.11}$$

After interpolation $C_p(k_x,\,k_w)$ is inverse Fourier-transformed in both dimensions. The final result is the matched filter correlation product $c_p(x,\,w)$.

The FDMF algorithm can be summarised in the following steps

1. The recorded data $\hat{s}_{RX}(x_r,\,t)$ is Fourier-transformed in both dimensions into $\hat{S}(k_x,\,\omega)$.

2. The Fourier-transform of a point scatterer in the centre of the target area $S(k_x, \omega)$ is calculated as given by equation D.0.5.

3. The Fourier-transform of the correlation product $C_p(k_x, \omega)$ is calculated as given by equation D.0.6.

4. The correlation product $C_p(k_x, \omega)$ is interpolated in the $\omega$-dimension into $C_p(k_x, k_w)$.

5. The matched filter correlation product $c_p(x, w)$ is found by inverse Fourier-transforming $C_p(k_x, k_w)$ in both dimensions.

The FDMF algorithm is an exact implementation of the matched filter. The only step that in practice will involve an approximation is the interpolation. The FDMF algorithm can be order of magnitude computationally more efficient than the matched filter implemented in the time domain due to the FFT algorithm. Often the most time consuming step is the interpolation.

# Appendix E

# GinSAR simulator

As a valuable tool in the development of GinSAR we have made a simulator that generates raw radar data in exactly the same format as the real radar. No modifications in the post-processing software are therefore needed to process the simulator data. This appendix briefly describes the simulator.

The target scene is defined by a selectable number of point scatterers. To simulate the effect of a distributed scatterer, many closely located point scatterers must be defined. It is only possible to model the impact of a homogeneous atmosphere on the propagation speed. The simulator assumes omni-directional antennas and scatterers. It is possible to define both a phase error function and a deviation in the length of the synthetic aperture. Only white Gaussian additive measurement noise can be modelled, non-linear effects in the electronics are not included except for analogue-to-digital converter quantisation.

When using the simulator many constants must be defined such as transmitter amplifier power. As far as possible we have used data specified by the producers of the components. But for some parameters such as the gain of the antennas when radar absorbing material is attached to the rim, a qualified guess is our best option. Therefore, the amplification in the whole transmitter and receiver chain becomes uncertain. To settle the uncertainty in practice, the constants are adjusted to fit the magnitude response of a given scatterer calculated from a real measurement. The simulator program is summarised by the following steps:

1. Define the position and magnitude of all scatterers in the scene.
2. Define the positions of the frequency sweeps on the synthetic aperture (the length of the synthetic aperture, the number of frequency sweeps and optionally the phase error function).
3. Define the transmitted frequency sweep pulse (start and stop frequency, duration).
4. For all positions on the synthetic aperture
   (a) For all scatterers in the scene

i. Add a delayed and scaled version of the transmitted frequency sweep pulse to the received signal for this position on the synthetic aperture. The delay is calculated as a function of the distance from the radar to the scatterer, the scale is calculated from the scatterer magnitude and the distance.

(b) Scale the signal by the gain of the radar (transmitter power, antenna gain, receiver gain).

(c) Add white measurement noise.

(d) Sample the received signal to the analogue-to-digital converter's precision (convert to 16 bits precision which effectively adds quantisation noise).

# Bibliography


[1] Ageing of Dams and Appurtenant Works - Review and Recommendations. *The International Commission on Large Dams (ICOLD)*, Bulletin 93, 1994.

[2] Worldwide Overview of Large Landslides of the 20th and 21st Centuries. United States Geological Survey, 2010. URL `http://landslides.usgs.gov/learning/majorls.php`.

[3] Special Issue on SEASAT-1 Sensors. *IEEE Journal on Oceanic Engineering*, OE-5(2), April, 1980.

[4] A. Aguasca, A. Broquetas, J. J. Mallorqui, and X. Fabregas. A solid state L to X-band flexible ground-based SAR system for continuous monitoring applications. In *Geoscience and Remote Sensing Symposium, 2004. IGARSS 04. Proceedings. 2004 IEEE International*, volume 2, pages 757–760, 2004.

[5] C. D. Ahrens. *Meteorology today: an introduction to weather, climate, and the environment*. Brooks/Cole Pub Co, 2007.

[6] G. Antonello, N. Casagli, P. Farina, J. Fortuny, D. Leva, G. Nico, A. J. Sieber, and D. Tarchi. A ground-based interferometer for the safety monitoring of landslides and structural deformations. In *Geoscience and Remote Sensing Symposium, 2003. IGARSS 03. Proceedings. 2003 IEEE International*, volume 1, pages 218–220, 2003.

[7] G. Antonello, D. Tarchi, N. Casagli, P. Farina, L. Guerri, and D. Leva. SAR interferometry from satellite and ground-based system for monitoring deformations on the Stromboli volcano. In *Geoscience and Remote Sensing Symposium, 2004. IGARSS 04. Proceedings. 2004 IEEE International*, volume 1. IEEE, 2004. ISBN 0780387422.

[8] E. P. W. Attema. The active microwave instrument on-board the ERS-1 satellite. *Proceedings of the IEEE*, 79(6):791–799, 1991.

[9] V. Barnett and T. Lewis. *Outliers in statistical data.* John Wiley & Sons, Inc, 1994.

[10] D. K. Barton. *Modern Radar System Analysis.* Artech House Publishers, 1988.

[11] J. C. Bennett and K. Morrison. Development of a ground-based, polarimetric synthetic aperture radar. In *Aerospace Applications Conference, 1996. Proceedings., 1996 IEEE*, volume 4, pages 139–146. IEEE, 2002. ISBN 0780331966. doi: 10.1109/AERO.1996.499408 .

[12] M. N. Berberan-Santos, L. Pogliani, and E. N. Bodunov. On the barometric formula. *American Journal of Physics*, 65(5):404–412, 1997.

[13] F. Berizzi and G. Corsini. Focusing of Two Dimensional ISAR Images by Contrast Maximization. In *Microwave Conference, 1992. 22nd European*, volume 2, pages 951–956. IEEE, 1992.

[14] N. Bleistein and R. A. Handelsman. *Asymptotic expansions of integrals*. Harcourt College Pub, 1975. ISBN 0030835968.

[15] LH Blikra. The Aaknes rockslide; monitoring, threshold values and early-warning. *Proc. 10'th Int. Symposium on Landslides and Engineered Slopes, Xi'an, China*, 2008.

[16] H. Breit, T. Fritz, U. Balss, M. Lachaise, A. Niedermeier, and M. Vonavka. TerraSAR-X SAR processing and products. *Geoscience and Remote Sensing, IEEE Transactions on*, 48(2):727–740, 2010. ISSN 0196-2892. doi: 10.1109/TGRS.2009.2031062.

[17] Andreas R. Brenner and Ludwig Roessing. Radar Imaging of Urban Areas by Means of Very High-Resolution SAR and Interferometric SAR. *IEEE Transactions on Geoscience and Remote Sensing*, 46(10):2971, 2008. doi: 10.1109/TGRS.2008.920911.

[18] R. Burgmann, P. A. Rosen, and E. J. Fielding. Synthetic aperture radar interferometry to measure Earth's surface topography and its deformation. *Annual Review of Earth and Planetary Sciences*, 28:169–209, 2000.

[19] C. Cafforio, C. Prati, and F. Rocca. SAR data focusing using seismic migration techniques. *Aerospace and Electronic Systems, IEEE Transactions on*, 27(2):194–207, 1991. ISSN 0018-9251.

[20] T. M. Calloway and G. W. Donohoe. Subaperture autofocus for synthetic aperture radar. *Aerospace and Electronic Systems, IEEE Transactions on*, 30(2):617–621, 1994. ISSN 0018-9251.

[21] N. Casagli, P. Farina, D. Leva, G. Nico, and D. Tarchi. Monitoring the Tessina landslide by a ground-based SAR interferometer and assessment of the system accuracy. In *Geoscience and Remote Sensing Symposium, 2002. IGARSS 02. 2002 IEEE International*, volume 5, pages 2915–2917. IEEE, 2002. ISBN 078037536X.

[22] J. L. Davis, T. A. Herring, I. I. Shapiro, A. E. E. Rogers, and G. Elgered. Geodesy by radio interferometry: Effects of atmospheric modelling errors on estimates of baseline length. *Radio Science*, 20(6):1593–1607, 1985.

[23] Karlus A. Camara de Macedo, Rolf Scheiber, and Alberto Moreira. An Autofocus Approach for Residual Motion Errors With Application to Airborne Repeat-Pass SAR Interferometry. *IEEE Transactions on Geoscience and Remote Sensing*, 46(10):3151, 2008. doi: 10.1109/TGRS.2008.924004.

[24] Y. L. Desnos, C. Buck, J. Guijarro, G. Levrini, J. L. Suchail, R. Torres, H. Laur, J. Closa, and B. Rosich. The ENVISAT advanced synthetic aperture radar system. In *Geoscience and Remote Sensing Symposium, 2000. Proceedings. IGARSS 2000. IEEE 2000 International*, volume 3, pages 1171–1173, 2000.

[25] M. Edrich. Design overview and flight test results of the miniaturised SAR sensor MISAR. In *Radar Conference, 2004. EURAD. First European*, pages 205–208. IEEE, 2004. ISBN 1580539939.

[26] P. H. Eichel and CV Jakowatz, Jr. Phase-gradient algorithm as an optimal estimator of the phase derivative. *Optics letters*, 14(20):1101–1103, 1989. ISSN 0146-9592.

[27] P. H. Eichel, D. C. Ghiglia, and CV Jakowatz, Jr. Speckle processing method for synthetic-aperture-radar phase correction. *Optics Letters*, 14 (1):1–3, 1989. ISSN 0146-9592.

[28] H. Essen, M. Hagelen, W. Johannes, R. Sommer, A. Wahlen, M. Schlechtweg, and A. Tessmann. High resolution millimetre wave measurement radars for ground based SAR and ISAR imaging. *Radar Conference, 2008. RADAR '08. IEEE*, pages 1–5, 2008. doi: 10.1109/RADAR.2008.4721023.

[29] J. R. Fienup and J. J. Miller. Aberration correction by maximizing generalized sharpness metrics. *JOSA A*, 20(4):609–620, 2003. ISSN 1520-8532.

[30] M R Foster and N J Guinzy. The coefficient of coherence: its estimation and use in geophysical data processing. *Geophysics*, 32(4):602–616, 1967.

[31] D Garbor. *Theory of communication*, volume 93, Part III, pp. 429-441. J. IEE (London), 1946.

[32] Jason H. Gart. *Electronics and Aerospace Industry in Cold War Arizona, 1945-1968: Motorola, Hughes Aircraft, Goodyear Aircraft.* PhD thesis, Arizona State University, 2006.

[33] Dennis C. Ghiglia and Mark D. Pritt. *Two-Dimensional Phase Unwrapping: Theory, Algorithms, and Software*. Wiley, 1998. doi: ISBN: 978-0-471-24935-1.

[34] P. T. Gough. A fast spectral estimation algorithm based on the FFT. *Signal Processing, IEEE Transactions on*, 42(6):1317–1322, 1994. ISSN 1053-587X.

[35] T. Hamasaki, L. Ferro-Famil, E. Pottier, and M. Sato. Applications of polarimetric interferometric ground-based SAR (GB-SAR) system to environment monitoring and disaster prevention. In *Radar Conference, 2005. EURAD 2005. European*, pages 29–32. IEEE, 2006. ISBN 2960055136.

[36] R. F. Hanssen. *Radar Interferometry - Data Interpretation and Error Analysis*. Remote Sensing and Digital Image Processing. Kluwer Academic Publishers, P O Box 322, 3300 AH Dordrecht, The Netherlands, 2001.

[37] L. J. Harcke, R. M. Ueberschaer, J. W. Sinko, and J. M. Strus. GPS/IMU Error Analysis for Airborne SAR Remote Sensing. In *Proceedings of the 20th International Technical Meeting of the Satellite Division of The Institute of Navigation (ION GNSS 2007)*, pages 1631–1635, 2001.

[38] Simon Haykin. *Communication Systems, pp 599-603*. John Wiley & Sons, 605 Third Avenue, New York, NY 10158, USA, Second edition, 1983.

[39] A. Hein. *Processing of SAR data: fundamentals, signal processing, interferometry*. Springer Verlag, 2004. ISBN 3540050434.

[40] H. Hellsten and L. E. Andersson. An inverse method for the processing of synthetic aperture radar data. *Inverse Problems*, 3:111, 1987.

[41] J. A. Högbom. Aperture synthesis with a non-regular distribution of interferometer baselines. *Astronomy and Astrophysics Supplement Series*, 15:417, 1974. ISSN 0365-0138.

[42] P. J. Huber and E. Ronchetti. *Robust statistics*. John Wiley & Sons Inc, 2009. doi: 10.1002/9780470434697.

[43] C. V. Jakowatz. *Spotlight-mode synthetic aperture radar: a signal processing approach*. Kluwer Academic Pub, 1996. ISBN 0792396774.

[44] C. V. Jakowatz, Jr and D. E. Wahl. Eigenvector method for maximum-likelihood estimation of phase errors in synthetic-aperture-radar imagery. *Journal of the Optical Society of America A*, 10(12):2539–2546, 1993. ISSN 1084-7529.

[45] Y. Jungang, H. Xiaotao, J. Tian, X. Guoyi, and Z. Zhimin. An Interpolated Phase Adjustment by Contrast Enhancement Algorithm for SAR. *Geoscience and Remote Sensing Letters, IEEE*, (99):211–215, 2011. ISSN 1545-598X. doi: 10.1109/LGRS.2010.2058090.

[46] D. Kahaner, C. B. Moler, S. Nash, and G. E. Forsythe. *Numerical methods and software*. Prentice-Hall Englewood Cliffs, NJ, 1989.

[47] James F. Kaiser and Ronald W. Schafer. On the Use of the Io-Sinh Window for Spectrum Analysis. *IEEE Transactions on Acoustics, Speech and Signal Processing*, ASSP-28(No 1):pp 105–107, 1980.

[48] J. Kolman. PACE: An autofocus algorithm for SAR. In *Radar Conference, 2005 IEEE International*, pages 310–314, 2005.

[49] F. N. Kong and T. L. By. Performance of a GPR system which uses step frequency signals. *Journal of applied geophysics*, 33(1-3):15–26, 1995. ISSN 0926-9851.

[50] H. Lee, J. H. Lee, S. J. Cho, N. H. Sung, and J. H. Kim. An Experiment of GB-SAR Interperometric Measurement of Target Displacement and Atmospheric Correction. In *Geoscience and Remote Sensing Symposium, 2008. IGARSS 2008. IEEE International*, volume 4, pages –240. IEEE, 2009.

[51] D. Leva, G. Nico, D. Tarchi, J. Fortuny-Guasch, and A.J. Sieber. Temporal analysis of a landslide by means of a ground-based SAR interferometer. *IEEE Transactions on Geoscience and Remote Sensing*, 41(4):745, 2003. doi: 10.1109/TGRS.2003.808902.

[52] J. Li and P. Stoica. Efficient mixed-spectrum estimation with applications to target feature extraction. *Signal Processing, IEEE Transactions on*, 44 (2):281–295, 1996. ISSN 1053-587X.

[53] X. Li, H. Sun, H. Gu, W. Su, and G. Liu. A new kind of ISAR autofocusing technique based on entropy criteria. In *Signal Processing Proceedings, 2000. WCCC-ICSP 2000. 5th International Conference on*, volume 3, pages 1806–1809. IEEE, 2000. ISBN 0780357477.

[54] K. H. Liu and D. C. Munson. Fourier-domain Multichannel Autofocus for synthetic aperture radar. In *Signals, Systems and Computers, 2008 42nd Asilomar Conference on*, pages 848–852, 2009.

[55] Z. S. Liu and J. Li. Synthetic-aperture-radar motion compensation and feature extraction by means of a relaxation-based algorithm. *JOSA A*, 15 (3):599–610, 1998. ISSN 1520-8532.

[56] P. Lombardo. A multichannel spaceborne radar for the COSMO-SkyMed satellite constellation. In *Aerospace Conference, 2004. Proceedings. 2004 IEEE*, volume 1, 2004.

[57] C. Lopez-Martinez, L. Pipia, X. Fabregas, A. Aguasca, S. Duque, J. J. Mallorqui, and J. Marturia. Polarimetric differential SAR interferometry: First results with ground-based measurements. *Geoscience and Remote Sensing Letters, IEEE*, 6(1):167–171, 2009. ISSN 1545-598X. doi: 10.1109/LGRS.2008.2009007.

[58] K. Lukin, A. Mogyla, V. Palamarchuk, P. Vyplavin, E. Kozhan, and S. Lukin. Monitoring of St. Sophia Cathedral interior using Ka-band Ground Based Noise Waveform SAR. In *Radar Conference, 2009. EuRAD 2009. European*, pages 215–217. IEEE, 2009.

[59] K. A. Lukin, A. A. Mogyla, V. P. Palamarchuk, P. L. Vyplavin, O. V. Zemlyaniy, Y. A. Shiyan, and M. Zaets. Ka-band bistatic ground-based noise waveform SAR for short-range applications. *Radar, Sonar and Navigation, IET*, 2(4):233–243, 2008. ISSN 1751-8784. doi: 10.1049/iet-rsn:20080017.

[60] Konstantin A. Lukin, Anatoliy A. Mogila, and Pavel L. Vyplavin. Ground-Based Noise Waveform Sar and Differential Interferometry for Remote Monitoring of Large Objects. *ISMW'07 Symposium Proceedings. Kharkov, Ukraine*, 2007.

[61] G. Luzi, M. Pieraccini, D. Mecatti, L. Noferini, G. Guidi, F. Moia, and C. Atzeni. Ground-based radar interferometry for landslides monitoring: atmospheric and instrumental decorrelation sources on experimental data. *IEEE Transactions on Geoscience and Remote Sensing*, 42(11):2454, 2004. doi: 10.1109/TGRS.2004.836792.

[62] G. Luzi, L. Noferini, D. Mecatti, G. Macaluso, M. Pieraccini, C. Atzeni, A. Schaffhauser, R. Fromm, and T. Nagler. Using a Ground-Based SAR Interferometer and a Terrestrial Laser Scanner to Monitor a Snow-Covered Slope: Results From an Experimental Data Collection in Tyrol (Austria). *Geoscience and Remote Sensing, IEEE Transactions on*, 47(2):382–393, 2009. ISSN 0196-2892. doi: 10.1109/TGRS.2008.2009994.

[63] C. E. Mancill and J. M. Swiger. A map drift autofocus technique for correcting higher-order SAR phase errors. In *27th Annual Tri-Service Radar Symposium Record*, pages 391–400, 1981.

[64] D. Massonnet and K. L. Feigl. Radar interferometry and its application to changes in the earth's surface. *Rev. Geophys.*, 36(4):441–500, 1998.

[65] S. Mehrdad. *Synthetic aperture radar signal processing with MATLAB algorithms*. New York: John Wiley & Sons, Inc, 1999.

[66] A. Meta and P. Hoogeboom. Development of signal processing algorithms for high resolution airborne millimeter wave FMCW SAR. In *Radar Conference, 2005 IEEE International*, pages 326–331. IEEE, 2004. ISBN 078038881X.

[67] Robert L. Morrison, Minh N. Do, and David C. Munson. SAR Image Autofocus By Sharpness Optimization: A Theoretical Study. *IEEE Transactions on Image Processing*, 16(9):2309, 2007. doi: 10.1109/TIP.2007.903252.

[68] Robert L Morrison, Minh N Do, and David C Munson. MCA: a multichannel approach to SAR autofocus. *IEEE Trans Image Process*, 18(4):840–53, 2009. doi: 10.1109/TIP.2009.2012883.

[69] R. L. Morrison Jr and M. N. Do. A multichannel approach to metric-based SAR autofocus. In *2006 International Conference on Image Processing*, volume 2, pages –1070, 2005. doi: 10.1109/ICIP.2006.312856.

[70] R. L. Morrison Jr and D. C. Munson Jr. An experimental study of a new entropy-based SAR autofocus technique. In *Image Processing. 2002. Proceedings. 2002 International Conference on*, volume 2, pages –441. IEEE, 2002. ISBN 0780376226.

[71] R. A. Muller and A. Buffington. Real-time correction of atmospherically degraded telescope images through image sharpening. *JOSA*, 64(9):1200–1210, 1974.

[72] D. C. Munson Jr, J. D. O'Brien, and W. K. Jenkins. A tomographic formulation of spotlight-mode synthetic aperture radar. *Proceedings of the IEEE*, 71(8):917–925, 1983. ISSN 0018-9219.

[73] Y. Nemoto, H. Nishino, M. Ono, H. Mizutamari, K. Nishikawa, and K. Tanaka. Japanese earth resources satellite-1 synthetic aperture radar. *Proceedings of the IEEE*, 79(6):800–809, 1991.

[74] G. Nico, D. Leva, G. Antonello, and D. Tarchi. Ground-based SAR interferometry for terrain mapping: theory and sensitivity analysis. *IEEE Transactions on Geoscience and Remote Sensing*, 42(6):1344, 2004. doi: 10.1109/TGRS.2004.826556.

[75] G. Nico, D. Leva, J. Fortuny-Guasch, G. Antonello, and D. Tarchi. Generation of digital terrain models with a ground-based SAR system. *IEEE Transactions on Geoscience and Remote Sensing*, 43(1):45, 2005. doi: 10.1109/TGRS.2004.838354.

[76] L. Noferini, M. Pieraccini, D. Mecatti, G. Luzi, C. Atzeni, A. Tamburini, and M. Broccolato. Permanent scatterers analysis for atmospheric correction in ground-based SAR interferometry. *IEEE Transactions on Geoscience and Remote Sensing*, 43(7):1459, 2005. doi: 10.1109/TGRS.2005.848707.

[77] Linhsia Noferini, Massimiliano Pieraccini, Daniele Mecatti, Giovanni Macaluso, Guido Luzi, and Carlo Atzeni. DEM by Ground-Based SAR Interferometry. *IEEE Geoscience and Remote Sensing Letters*, 4(4):659–663, 2007.

[78] Linhsia Noferini, Takuya Takayama, Massimiliano Pieraccini, Daniele Mecatti, Giovanni Macaluso, Guido Luzi, and Carlo Atzeni. Analysis of Ground-Based SAR Data With Diverse Temporal Baselines. *IEEE Transactions on Geoscience and Remote Sensing*, 46(6):1614, 2008. doi: 10.1109/TGRS.2008.916216.

[79] J. F. Nouvel, S. Angelliaume, and O. Ruault du Plessis. The ONERA Compact Ka-SAR. In *Radar Conference, 2008. EuRAD 2008. European*, pages 475–478. IEEE, 2009.

[80] M. Pieraccini, G. Luzi, and C. Atzeni. Terrain mapping by ground-based interferometric radar. *IEEE Transactions on Geoscience and Remote Sensing*, 39(10):2176–2181, 2001.

[81] L. Pipia, A. Aguasca, X. Fabregas, J. J. Mallorqui, C. Lopez-Martinez, and J. Marturia. Mining induced subsidence monitoring in urban areas with a ground-based SAR. In *Urban Remote Sensing Joint Event, 2007*, pages 1–5, 2007.

[82] L. Pipia, X. Fabregas, A. Aguasca, S. Duque, J. J. Mallorqui, and C. Lopez-Martinez. Polarimetric Deformation Maps Retrieval of Urban Areas using Ground-Based SAR Acquisitions. In *Geoscience and Remote Sensing Symposium, 2008. IGARSS 2008. IEEE International*, volume 4, pages 320–327. IEEE, 2009.

[83] Luca Pipia, Xavier Fabregas, Albert Aguasca, and Carlos Lopez-Martinez. Atmospheric Artifact Compensation in Ground-Based DInSAR Applications. *IEEE Geoscience and Remote Sensing Letters*, 5(1):88, 2008. doi: 10.1109/LGRS.2007.908364.

[84] P. Prats and J. J. Mallorqui. Estimation of azimuth phase undulations with multisquint processing in airborne interferometric SAR images. *Geoscience and Remote Sensing, IEEE Transactions on*, 41(6):1530–1533, 2003. ISSN 0196-2892. doi: 10.1109/TGRS.2003.814140.

[85] R. K. Raney, A. P. Luscombe, E. J. Langham, and S. Ahmed. Radarsat [sar imaging]. *Proceedings of the IEEE*, 79(6):839–849, 1991.

[86] D. Reale, F. Serafino, and V. Pascazio. An Accurate Strategy for 3-D Ground-Based SAR Imaging. *Geoscience and Remote Sensing Letters, IEEE*, 6(4):681–685, 2009. ISSN 1545-598X. doi: 10.1109/LGRS.2009.2023537.

[87] P. A. Rosen, S. Hensley, K. Wheeler, G. Sadowy, T. Miller, S. Shaffer, R. Muellerschoen, C. Jones, H. Zebker, and S. Madsen. UAVSAR: a new NASA airborne SAR system for science and technology research. In *Radar, 2006 IEEE Conference on*, page 8. IEEE, 2006. ISBN 0780394968. doi: 10.1109/RADAR.2006.1631770 .

[88] H. Rudolf, D. Leva, D. Tarchi, and A. J. Sieber. A mobile and versatile SAR system. In *Geoscience and Remote Sensing Symposium, 1999. IGARSS 99 Proceedings. IEEE 1999 International*, volume 1, pages 592–594, 1999.

[89] Paul Segall and James L. Davis. GPS Applications for Geodynamics and Earthquake Studies. *Annual Review of Earth Planet and Science*, 25:301 – 36, 1997.

[90] P. L. Sharma. Accurate frequency estimation using phase information. In *Circuits and Systems, 1990., Proceedings of the 33rd Midwest Symposium on*, pages 309–310. IEEE, 2002. ISBN 0780300815.

[91] F. S. Solheim, J. Vivekanandan, R. H. Ware, and C. Rocken. Propagation delays induced in GPS signals by dry air, water vapor, hydrometeors, and

other particulates. *Journal of Geophysical Research*, 104(D8):9663–9670, 1999.

[92] M. Soumekh. Band-limited interpolation from unevenly spaced sampled data. *Acoustics, Speech and Signal Processing, IEEE Transactions on*, 36 (1):110–122, 1988. ISSN 0096-3518.

[93] R. H. Stolt. Migration by Fourier transform. *Geophysics*, 43:23, 1978.

[94] Dario Tarchi. Monitoring landslide displacements by using ground-based synthetic aperture radar interferometry: Application to the Ruinon landslide in the Italian Alps. *Journal of Geophysical Research*, 108(B8):2387, 2003. doi: 10.1029/2002JB002204.

[95] D. G. Thompson, J. S. Bates, and D. V. Arnold. Extending the phase gradient autofocus algorithm for low-altitude stripmap mode SAR. In *Radar Conference, 1999. The Record of the 1999 IEEE*, pages 36–40, 1999.

[96] S. I. Tsunoda, F. Pace, J. Stence, M. Woodring, W. H. Hensley, A. W. Doerry, and B. C. Walker. Lynx: A high-resolution synthetic aperture radar. In *Aerospace Conference Proceedings, 2000 IEEE*, volume 5, pages 51–58. IEEE, 2000. ISBN 0780358465.

[97] George L Turin. An Introduction to Matched Filters. *IRE Transactions on Information Theory*, pages 311–329, 1960.

[98] F. T. Ulaby and M. C. Dobson. *Handbook of radar scattering statistics for terrain*. Artech House (Norwood, MA), 1989.

[99] W. L. Van Rossum, M. P. G. Otten, and R. J. P. Van Bree. Extended PGA for range migration algorithms. *Aerospace and Electronic Systems, IEEE Transactions on*, 42(2):478–488, 2006. ISSN 0018-9251.

[100] H. Van Trees. *Optimum array processing*. Wiley, 2002.

[101] D. E. Wahl, P. H. Eichel, D. C. Ghiglia, and C. V. Jakowatz Jr. Phase gradient autofocus-a robust tool for high resolution SAR phase correction. *Aerospace and Electronic Systems, IEEE Transactions on*, 30(3):827–835, 1994. ISSN 0018-9251.

[102] M. Weiss, O. Peters, and J. Ender. A three dimensional SAR system on an UAV. In *Geoscience and Remote Sensing Symposium, 2007. IGARSS 2007. IEEE International*, pages 5315–5318. IEEE, 2008.

[103] C. Werner, T. Strozzi, A. Wiesmann, and U. Wegmuller. A ground-based real-aperture radar instrument for differential interferometry. In *Radar Conference, 2009 IEEE*, pages 1–4. IEEE, 2009.

[104] R. Werninghaus and S. Buckreuss. The TerraSAR-X mission and system design. *Geoscience and Remote Sensing, IEEE Transactions on*, 48(2):606–614, 2010. ISSN 0196-2892. doi: 10.1109/TGRS.2009.2031062.

[105] R. Werninghauss and S. Buckreuss. The TerraSAR-X mission and system design. *Geoscience and Remote Sensing, IEEE Transactions on*, 48(2):606–614, 2010. ISSN 0196-2892. doi: 10.1109/TGRS.2009.2031062.

[106] L. Xi, L. Guosui, and J. Ni. Autofocusing of ISAR images based on entropy minimization. *Aerospace and Electronic Systems, IEEE Transactions on*, 35 (4):1240–1252, 1999. ISSN 0018-9251.

[107] W. Ye, T. S. Yeo, and Z. Bao. An optimal method for phase error estimation in SAR imagery. In *Geoscience and Remote Sensing Symposium Proceedings, 1998. IGARSS 98. 1998 IEEE International*, volume 2, pages 1165–1167. IEEE, 1998. ISBN 0780344030.

[108] E. C. Zaugg, D. L. Hudson, and D. G. Long. The BYU SAR: A small, student-built SAR for UAV operation. In *Geoscience and Remote Sensing Symposium, 2006. IGARSS 2006. IEEE International Conference on*, pages 411–414. IEEE, 2006. ISBN 0780395107.

[109] Y. Zheng and Z. Bao. Autofocusing of SAR images based on RELAX. In *Radar Conference, 2000. The Record of the IEEE 2000 International*, pages 533–538. IEEE, 2000. ISBN 0780357760.

[110] Zheng-Shu Zhou. Development of a ground-based polarimetric broadband SAR system for noninvasive ground-truth validation in vegetation monitoring. *IEEE Transactions on Geoscience and Remote Sensing*, 42(9):1803, 2004. doi: 10.1109/TGRS.2004.832248.

[111] H.-M Zogg. Terrestrisches Laserscanning - Ein allgemeiner Uberblick uber Messmethoden und Einsatzmoglichkeiten in der Geomatik. *Geomatik-News*, 2007.